SECURITY CLASSIFICATION OF THIS PAGE

REPORT DOCUMENTATION PAGE

Form Approved
OMB No. 0704-0188

1a. REPORT SECURITY CLASSIFICATION UNCLASSIFIED	1b. RESTRICTIVE MARKINGS NONE
2a. SECURITY CLASSIFICATION AUTHORITY **AD-A217 454**	3. DISTRIBUTION/AVAILABILITY OF REPORT APPROVED FOR PUBLIC RELEASE; DISTRIBUTION UNLIMITED.
	5. MONITORING ORGANIZATION REPORT NUMBER(S) AFIT/CI/CIA-88- 6
6a. NAME OF PERFORMING ORGANIZATION AFIT STUDENT AT UNIVERSITY OF ILLINOIS 6b. OFFICE SYMBOL (If applicable)	7a. NAME OF MONITORING ORGANIZATION AFIT/CIA
6c. ADDRESS (City, State, and ZIP Code)	7b. ADDRESS (City, State, and ZIP Code) Wright-Patterson AFB OH 45433-6583
8a. NAME OF FUNDING/SPONSORING ORGANIZATION 8b. OFFICE SYMBOL (If applicable)	9. PROCUREMENT INSTRUMENT IDENTIFICATION NUMBER
8c. ADDRESS (City, State, and ZIP Code)	10. SOURCE OF FUNDING NUMBERS PROGRAM ELEMENT NO. / PROJECT NO. / TASK NO. / WORK UNIT ACCESSION NO.

11. TITLE (Include Security Classification) (UNCLASSIFIED)

NUMERICAL SIMULATION OF LEADING-EDGE VORTEX ROLLUP AND BURSTING

12. PERSONAL AUTHOR(S)

STEVEN ALLAN BRANDT

13a. TYPE OF REPORT	13b. TIME COVERED	14. DATE OF REPORT (Year, Month, Day)	15. PAGE COUNT
THESIS/~~DISSERTATION~~	FROM _____ TO _____	1988	117

16. SUPPLEMENTARY NOTATION

APPROVED FOR PUBLIC RELEASE IAW AFR 190-1
ERNEST A. HAYGOOD, 1st Lt, USAF
Executive Officer, Civilian Institution Programs

17. COSATI CODES			18. SUBJECT TERMS (Continue on reverse if necessary and identify by block number)
FIELD	GROUP	SUB-GROUP	

19. ABSTRACT (Continue on reverse if necessary and identify by block number)

90 01 31 009

20. DISTRIBUTION/AVAILABILITY OF ABSTRACT	21. ABSTRACT SECURITY CLASSIFICATION
☒ UNCLASSIFIED/UNLIMITED ☐ SAME AS RPT. ☐ DTIC USERS	UNCLASSIFIED

22a. NAME OF RESPONSIBLE INDIVIDUAL	22b. TELEPHONE (Include Area Code)	22c. OFFICE SYMBOL
ERNEST A. HAYGOOD, 1st Lt, USAF	(513) 255-2259	AFIT/CI

DD Form 1473, JUN 86 *Previous editions are obsolete.* SECURITY CLASSIFICATION OF THIS PAGE

AFIT/CI "OVERPRINT"

NUMERICAL SIMULATION OF LEADING-EDGE VORTEX ROLLUP AND BURSTING

BY
STEVEN ALLAN BRANDT, Major, USAF

University of Illinois at Urbana-Champaign, 1988
110 pages

ABSTRACT

Vortex aerodynamics has played an important role in the development of high performance aircraft in recent years. Although computer codes which solve the three dimensional Euler equations have been used extensively to study leading-edge vortices, they don't include physical viscosity effects associated with vortex flows. The Euler solvers do, however, contain numerical viscosity. As a result, viscosity effects in the Euler solutions such as vortex core size, vortex burst location, leading edge separation, and vortex rollup often do not agree quantitatively with results of physical experiments. The present work defines models for these physical viscosity effects which can be coupled with an Euler solver to improve modeling of vortex physics.

A vortex core model is derived from the steady, incompressible Navier-Stokes equations written in cylindrical coordinates. The core model is coupled with an Euler solver and tested on a variety of delta wings over a range of angles of attack. The resulting surface pressure distributions and vortex burst locations are shown to be much closer to wind tunnel data and results from Navier-Stokes solutions than results from Euler codes alone.

A second model is defined for viscosity effects in the viscous shear layer near the rounded leading edge of a highly swept wing based on an analogy to the boundary layer on a flat plate. The model is incorporated into an Euler code through the surface boundary condition and source terms in the boundary cells. The modified code is tested on several highly swept wings with rounded leading edges. Results are also shown to be in closer agreement with wind tunnel data for the same wing geometry than results from an unmodified Euler code.

NUMERICAL SIMULATION OF LEADING-EDGE VORTEX ROLLUP AND BURSTING

BY

STEVEN ALLAN BRANDT

B.S., Iowa State University of Science and Technology, 1975
M.S., Iowa State University of Science and Technology, 1976

THESIS

Submitted in partial fulfillment of the requirements
for the degree of Doctor of Philosophy in
Aeronautical and Astronautical Engineering
in the Graduate College of the
University of Illinois at Urbana-Champaign, 1988

Urbana, Illinois

UNIVERSITY OF ILLINOIS AT URBANA-CHAMPAIGN

THE GRADUATE COLLEGE

JULY 1988

WE HEREBY RECOMMEND THAT THE THESIS BY

STEVEN ALLAN BRANDT

ENTITLED NUMERICAL SIMULATION OF LEADING EDGE VORTEX ROLLUP AND BURSTING

BE ACCEPTED IN PARTIAL FULFILLMENT OF THE REQUIREMENTS FOR

THE DEGREE OF DOCTOR OF PHILOSOPHY

Ki Dong Lee
Director of Thesis Research

M. A. Jakobsen
Head of Department

Committee on Final Examination†

Ki Dong Lee
Chairperson

† Required for doctor's degree but not for master's.

0-517

ABSTRACT

Vortex aerodynamics has played an important role in the development of high performance aircraft in recent years. Although computer codes which solve the three dimensional Euler equations have been used extensively to study vortex flows, they don't include physical viscosity effects associated with vortex flows. The Euler solvers do, however, contain numerical viscosity. As a result, viscosity effects in the Euler solutions such as vortex core size, vortex burst location, leading edge separation, and vortex rollup often do not agree quantitatively with results of physical experiments. The present work defines models for these physical viscosity effects which can be coupled with an Euler solver to improve modeling of vortex physics.

A vortex core model is derived from the steady, incompressible Navier-Stokes equations written in cylindrical coordinates. The core model is coupled with an Euler solver and tested on a variety of delta wings over a range of angles of attack. The resulting surface pressure distributions and vortex burst locations are shown to be much closer to wind tunnel data and results from Navier-Stokes solutions than results from Euler codes alone.

A second model is defined for viscosity effects in the viscous shear layer near the rounded leading edge of a highly swept wing based on an analogy to the boundary layer on a flat plate. The model is incorporated into an Euler code through the surface boundary condition and source terms in the boundary cells. The modified code is tested on several highly swept wings with rounded leading edges. Results are also shown to be in closer agreement with wind tunnel data for the same wing geometry than results from an unmodified Euler code.

DEDICATION

This work is dedicated to my mother, who taught me to set lofty goals, to my father, who taught me the value of hard work, to my wife, Joni, who endured more than I that the job could be completed, and to my children, Rob, Katie, John, and Maria, who got by for the past three years on less than their fair share of their father.

ACKNOWLEDGMENT

The author gratefully acknowledges the guidance and instruction of Professor Ki Lee, without whom this work could not have been accomplished. The encouragement and insight of Dr. August Verhoff and Dr. Ray Cosner of the McDonnell-Douglas Corporation are also greatly appreciated. This work was supported in part by a grant from the McDonnell-Douglas Corporation and by the Air Force Institute of Technology. Special thanks are also due to Jim Loellbach and Tedd Pierce for sharing their knowledge of computer operating systems, grid generation technology, and computer graphics.

TABLE OF CONTENTS

LIST OF FIGURES

NOMENCLATURE

Symbol	
a, a_E	area of vortex core in model and in Euler solution
C_f	skin friction coefficient
C_ϕ	wall proximity parameter
D	numerical viscosity operator
E	energy
$\hat{f}, \hat{g}, \hat{h}$	fluxes of flow quantities in X, Y and Z directions
H	enthalpy
h	cell volume
i, j, k	chordwise, vertical and spanwise grid indices
K_a, K_g, K_i	vortex core model area, growth, and image coefficients
K_s, K_t	shear layer model shear stress and thickness parameters
K_1, K_2, K_3	integral equation coefficients
K_4, K_5	constants
L	length of vortex from apex to burst point
l	distance from delta wing apex
l_z, l_z	normal distances from wing surface and symmetry plane
N	correction operator
P, Q	difference operators
p	pressure
Re	Reynolds number
S	source terms
t	time
U, V, W	velocities in the X, Y, and Z coordinate directions
U_∞	free stream velocity

u,v,w	velocities in the x, r and θ coordinate directions
$\hat{w}$	flow quantities in Euler equations
X,Y,Z	chordwise, vertical and spanwise Cartesian coordinates
x,r,θ	axial, radial, and circumferential cylindrical coordinates
α	wing angle of attack
Γ	vortex strength
γ	ratio of specific heats
δ, δ_s	core radius and shear layer thickness
ϵ	ratio of core diameter to vortex length
ϕ_Y, ϕ_Z	vortex axis inclination angles
μ	air viscosity
ρ	air density

Subscripts

a	based on area difference
i	due to image vorticies
E	in the Euler solution
f	skin friction
g	core growth
s	shear layer
t	thickness
Y	angles and distances measured parallel to the Y axis
Z	angles and distances measured parallel to the Z axis
0	central axis of the vortex
δ	vortex core edge
∞	free stream

Superscripts

n	time level or iteration count
(0),(1),(2)	stages in Runge-Kutta scheme

CHAPTER 1

INTRODUCTION

1.1 MOTIVATION OF THE PRESENT WORK

Vortex aerodynamics has played an increasingly important role in the design of high performance aircraft in recent years. In the late 1940's, wind tunnel studies of wings with triangular or delta planforms revealed that such wings produced more lift at high angles of attack than was predicted by conventional finite wing theory. The first of these studies, which was reported by Wilson and Lovell [1], found that the magnitude of this extra lift was increased when the test wing was given a sharp leading edge. Flow visualization in wind tunnels and water channels revealed that as a delta wing approaches an angle of attack where flow separation would cause an unswept wing to stall, the flow over each highly swept leading edge instead rolls up into a tornado-like flow structure called a leading edge vortex. The use of a sharp leading edge causes the flow to separate and form a vortex at a lower angle of attack. Since the separated flow

rolls up instead of being disorganized into turbulence, the loss of lift normally associated with a stall is delayed until higher angles of attack. Like a tornado, leading edge vortices have very low pressures in their center or core region. Because of this, they lower the pressure on a portion of the upper surface of the wing and hence increase the amount of lift produced. The extra vortex lift gives delta-winged aircraft like the F-102 and F-106 extremely good maneuverability at low speeds.

The benefits of leading edge vortices have prompted designers to include vortex lift-generating surfaces in such modern high performance aircraft as the F-16, F-18, SR-71, Concorde SST, and even the Space Shuttle. Figure 1 shows planform views of these aircraft with the leading-edge vortex-generating surfaces identified by crosshatching. Such aircraft are able to fly at angles of attack greater than 30 degrees in some cases without experiencing a stall. Aircraft with better high speed performance can be designed by relying on vortex lift for their low speed, high angle of attack operations. However, care must be taken when designing such aircraft to avoid problems which can result from the presence of vortices in the flow field.

As more experimental data on leading edge vortices were accumulated, researchers such as Hummel [2] and Anders [3] found that when a delta wing operates at very high angles of attack, axial pressure gradients develop in the cores of its leading edge vortices. As angle of attack is increased, these pressure gradients eventually cause local stagnation or reversal of the flow in the core. When this happens, it causes the core to grow rapidly and break down into random turbulence in much the same way that stall occurs on unswept wings. This phenomenon is called vortex bursting. Several researchers including Wentz [4], Payne and Nelson [5], Hall [6], and Lawford and Beauchamp [7] have made extensive wind tunnel and water channel tests of a variety of delta wings. They have created a large body of bursting location data as a function of sweep angle and angle of attack.

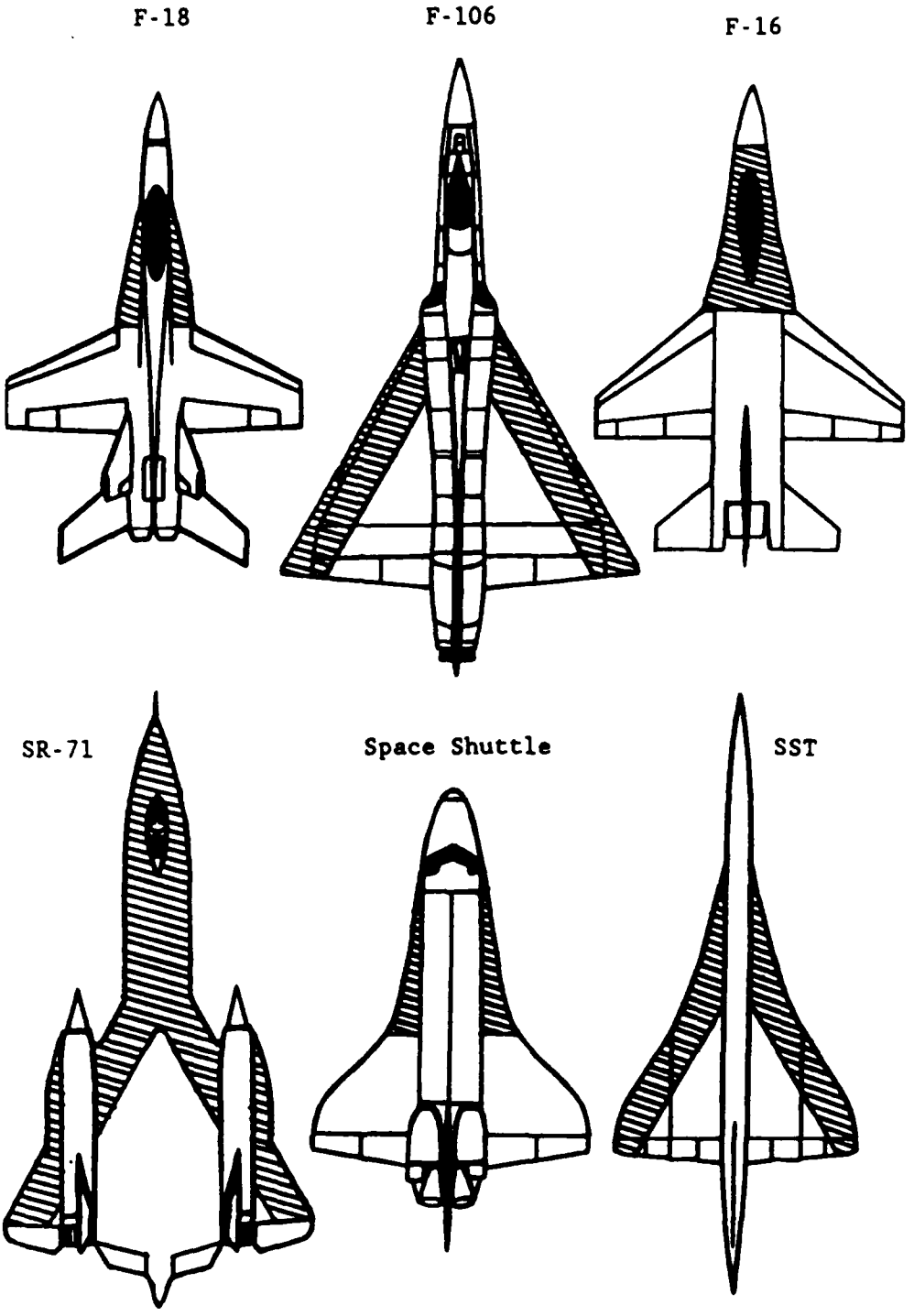

Figure 1. Planform views of some high performance aircraft. Surfaces which generate leading edge vortices are crosshatched.

When bursting occurs, lift is greatly reduced. If the vortex on one wing of an aircraft bursts before that on the other wing, the aircraft experiences severe control problems. Because bursting progresses from the wing trailing edge toward the apex, it can also cause an uncontrollable pitchup on some delta wings. In addition, the turbulence present in a burst vortex can cause structural fatigue problems in aircraft components which are not designed for that frequency of cyclic loading. Skow, Titriga, and Moore [8], among others, have described aircraft configurations which even experience control difficulties due to the motion and interaction of the vortices they produce before any bursting occurs.

Present technologies for understanding vortices and utilizing them in aircraft design have some serious limitations. Wind tunnels and water channels are currently used for the majority of vortex-related design development work, but such testing is expensive and requires long lead times, making it poorly suited to preliminary, iterative design work. Wind tunnels also provide only limited access to local flow details.

Computational fluid dynamics (CFD) technologies have shown considerable ability to model vortex effects. Changes to the flow conditions and vehicle configurations being modeled are accomplished in CFD codes with less effort than is required for changes in wind tunnel models and test conditions. This makes CFD very attractive for preliminary design and configuration definition work.

Several mathematical models and numerical methods have been developed to simulate leading edge vortices. As available computing power has increased, solution technology has progressed from the leading edge suction analogy of Polhamus [9] to panel methods, [10,11] then to Euler equation formulations. [12,13,14,15] With each new method, the requirement for computer speed and memory has increased. In recent years, attempts have been made to solve the Navier-Stokes equations for flowfields around delta

wings. [16,17,18] This technology, however, is not yet mature. Numerical problems associated with grid density and truncation error where high gradients are present have yet to be resolved. In addition, current Navier-Stokes codes employ turbulence models which are inadequate for vortex flows. Computing time and memory requirements of Navier-Stokes codes also make them too expensive for routine uses.

On the other hand, computer codes which solve the Euler equations offer a low-cost alternative to the Navier-Stokes solvers for problems where viscosity effects are either negligible or can be represented by simple mathematical models. Many researchers, including Rizzi [19] and Newsome [20], have made extensive use of Euler solvers to simulate leading edge vortex flows. Their results are often in good qualitative agreement with experimental and Navier-Stokes results, but they frequently fail to accurately predict such viscosity effects as vortex core size and bursting location. Analytic models for physical viscosity effects can be coupled with the Euler codes. The formulation of such a method would contribute to a better understanding of the processes which occur in a leading edge vortex. The combination of Euler code and model would be a useful tool for vortex research and aircraft design. This is the motivation for the present research.

1.2 DESCRIPTION OF THE PROBLEM

Computer codes which solve the Euler equations do not attempt to include physical viscosity effects. Ideally, an Euler solution should be totally inviscid. In practice, however, numerical effects which are similar to physical viscosity are present in Euler solutions. This numerical viscosity will be described in greater detail in Chapter 2.

Because of numerical viscosity, Euler solutions contain such viscous

phenomena as flow separation, leading edge vortices, and vortex breakdown. These effects are not, however, controlled by the viscous physics of the flow being modeled. For flow problems where viscosity effects are relatively unimportant, the difference between numerical and physical viscosity has a relatively small effect on the flow solutions. For these cases, Euler solvers often give acceptable results.

In flow problems involving leading edge vortices, however, viscosity effects can have a profound influence on the very structure of the flow solution. In particular, the leading edge separation which leads to vortex rollup and the onset of vortex bursting are both strongly affected by viscosity. In general, numerical viscosity effects are in the same direction as physical viscosity, so there is often qualitative agreement between Euler solutions and physical experiments. The magnitudes of physical and numerical viscosity frequently differ, however. While physical viscosity is solely a function of flow quantities, numerical viscosity is also influenced by the computational algorithm used and the size, shape and orientation of the grid. As a result, quantitative agreement between computations and physics is often difficult to achieve.

A need therefore exists for a method to replace or correct the effects of numerical viscosity in Euler solutions so that they better represent the viscous physics. In the present effort, viscosity effects are measured by flow quantities in the Euler solution such as pressure, velocity, vortex strength and core diameter. Corrections to the flow quantities are then calculated from algebraic models for the viscous processes near the wing surface and in the vortex core. These corrections are incorporated into the Euler code as source terms in the flow equations. For this method to succeed, the algebraic models must properly represent the relevant viscous physics.

1.3 EXISTING VORTEX MODELS

A great deal of theoretical modeling of vortex decay and vortex bursting has been done by a variety of researchers in the past 50 years. Research on this topic has typically been divided into two areas of interest. The oldest studies of vortex decay dealt with aircraft trailing vortices. When vortex bursting on delta wings was discovered in the late 40's, a great deal of attention was given to trying to understand this phenomenon. In the late 60's and early 70's, when jumbo jets were introduced into commercial airline service, their trailing vortices created serious hazards to other aircraft. Attention once more turned to the modeling of trailing vortex decay. Models for vortex bursting were studied in search of a means to alleviate the hazard of trailing vortices by causing them to burst. Then, in the late 70's and 80's the design of high performance aircraft such as the F-16, F-18, and Space Shuttle focused interest once more on leading edge vortex bursting.

All of the models and theories developed in this area have implications for the present research. Each model has certain advantages and disadvantages for describing vortex bursting. A survey of all the models reveals at the same time a great variety in their formulation and yet a general similarity in their fundamental assumptions, especially the shapes of their assumed velocity distributions.

One of the earliest and simplest 3-dimensional vortex models was the potential vortex. Circumferential velocity in this vortex varies with the inverse of the distance from the center. This causes circulation around all closed paths containing the vortex center to be the same. The potential vortex model has no viscous core, so circumferential velocity becomes infinite at the center. Far from the center, however, the velocity field matches well with those of vortices in nature. Most subsequent vortex models have been designed to match the potential vortex velocity

field outside their core regions. Axial velocities for the potential vortex are defined as being uniform.

A simple modification of the potential vortex avoids the singularity at the center. Known as the Rankine vortex, this model has a central core which rotates as a solid body. At the core edge, the circumferential velocity profile abruptly changes to that of the potential vortex. Circumferential velocities match at the core edge, but slopes do not. The great advantage of the Rankine vortex for modeling is the simplicity of this circumferential profile. For this reason, it has been a popular velocity profile for the development of bursting theories and simulations. Like the potential vortex, axial velocities for the Rankine vortex are uniform.

A more physically reasonable vortex model was derived by Lamb [23] as a similarity solution for the viscous decay of an infinite line vortex which is initially concentrated into a potential vortex. The circumferential velocities in this model are expressed as a function of time. For this reason, the Lamb vortex was used by Iversen [24] to model trailing vortex decay. In Iversen's model, a variable turbulent eddy viscosity is used instead of Lamb's constant viscosity. This allows Iversen to match water channel trailing vortex decay data more accurately. Both models do not consider axial variations in vortex properties. This prevents them from modeling vortex bursting in their present form.

The analytic modeling of vortex bursting really started with Hall's [25] work published in 1961. He assumed that once viscosity effects had determined the circumferential velocity profile of the vortex, the bursting process could by modeled inviscidly. Hall also assumed a conical, incompressible vortex with steady, laminar flow. The initial velocity profiles assumed by Hall allowed variation in the axial velocities, but both his axial and circumferential profiles had singularities at the vortex center. This forced him to define a diffusive sub-core to avoid the

singularity and then patch the two solutions. As a result, Hall's model was relatively complex.

Other researchers such as Brown, [26] Mager, [27] Krause [28] and Powell and Murman [29] have derived similar sets of differential equations to describe bursting. Each used slightly different assumptions and methods, but all used some arbitrarily defined initial velocity distribution. The various velocity profiles employed are described and compared in Appendix A. Each researcher solved the set of equations numerically and/or analytically. Mager obtained a closed form solution for his ordinary differential equations for the case of an isolated vortex in a uniform flow. Because the flow field around a delta wing is far from uniform, Mager's closed form solution is not used in the present work. Both Krause [30] and Grabowski and Berger [31] used the algebraic velocity profiles defined by Mager to make numerical simulations of vortex bursting. The results of these simulations agree well with bursting experiments performed in vortex tubes by Harvey [32], Sarpkaya [33], and Faler and Leibovich [34].

A great deal of theoretical and experimental work has been done aimed at explaining vortex bursting in terms of stability. The first of these was Jones [34], who analyzed the response of an arbitrary cylindrical flow to infinitesimal axial disturbances. Jones then applied his results to Hall's solution. Subsequent analyses by Benjamin [35], Lessen [36], Leibovich [37] and others have described vortex breakdown as a transition or jump between two flow states, one of which has reverse axial flow, such that both flow states satisfy the governing differential equations. They defined stability bounds which suggest that some vortices with "super-critical" initial axial and circumferential velocity distributions are prone to bursting while vortices with "subcritical" initial profiles are not. The numerical simulations by Grabowski and Berger tended to disagree with these stability bounds, however. Mager discovered similar conjugate

flow states in his closed form solutions. He found that the change from one flow state to another could either be a smooth transition or an abrupt jump, depending on the nature of the initial velocity profile.

All of these methods have used arbitrary initial velocity profiles as part of their analyses. These velocity profiles have generally been axisymmetric. The flow external to the vortex core has been modeled as either a uniform velocity field with a line vortex added to it, or as a conical flow. For these reasons, strict applicability of any of the solutions or criteria to a general leading edge vortex problem is limited. Some of the basic methods used to obtain these solutions are, however, used in the present work.

1.4 OUTLINE OF THE PRESENT WORK

A model for viscosity effects in vortex cores is derived from the steady, incompressible Navier-Stokes equations written in cylindrical coordinates. The model is formulated to allow it to be incorporated into a computer code which solves the Euler equations in three dimensions. The resulting Euler code/core model combination is tested on a variety of problems. The first tests are made on a simple rectangular box domain. These tests determine the ability of the core model to correct for the effects of numerical viscosity in the Euler solution. Further tests are made on the rectangular grid to determine the model's ability to produce vortex bursting when a rapidly growing physical core is modeled and to prevent bursting if a physical core with zero growth is assumed. The Euler code with core model is then tested on a variety of delta wings over a range of angles of attack. The resulting surface pressure distributions and vortex burst location predictions are compared with wind tunnel data and results from Navier-Stokes simulations and Euler codes alone.

A model for total pressure losses due to viscosity in the shear layer near the rounded leading edge of a highly swept wing is defined based on an analogy to the boundary layer on a flat plate. The model is incorporated into an Euler code through the surface boundary condition and momentum source terms in the boundary cells. The modified code is tested over a range of angles of attack for several highly swept wings with rounded leading edges. These flow solutions are compared with wind tunnel data and results from an unmodified Euler code.

CHAPTER 2

COMPUTATIONAL METHODS

2.1 EULER EQUATIONS

The Navier-Stokes equations are generally used to describe the unsteady motion of a compressible viscous fluid. For many flow problems, however, viscosity effects are confined to relatively small portions of the flowfield. For instance, for low speed flow around an infinite wing, viscosity effects may be confined to a thin boundary layer close to the wing surface. If this region is modeled appropriately, the rest of the flowfield may be solved with a simplified version of the Navier-Stokes equations in which the viscosity terms are omitted. These simplified equations are known as the Euler equations. The use of the Euler equations bypasses the computational difficulties of dealing with the very small length scales associated with viscosity effects.

A number of computer codes are available to solve the Euler equations for flowfields around three-dimensional aerodynamic shapes. Two of these

codes, FLO57 [13] and ARC3D [15], are modified and used in the present research. The computational methods employed in each of these codes will be described because the present research is directed at overcoming some of the limitations inherent in those methods.

The time dependent, compressible Euler equations can be written in matrix form:

$$\frac{\partial \hat{w}}{\partial t} + \frac{\partial \hat{f}}{\partial X} + \frac{\partial \hat{g}}{\partial Y} + \frac{\partial \hat{h}}{\partial Z} = 0 \tag{1}$$

where:

$$\hat{w} = \begin{bmatrix} \rho \\ \rho U \\ \rho V \\ \rho W \\ \rho E \end{bmatrix} \quad \hat{f} = \begin{bmatrix} \rho U \\ \rho U^2 + p \\ \rho UV \\ \rho UW \\ \rho UH \end{bmatrix} \quad \hat{g} = \begin{bmatrix} \rho V \\ \rho VU \\ \rho V^2 + p \\ \rho VW \\ \rho VH \end{bmatrix} \quad \hat{h} = \begin{bmatrix} \rho W \\ \rho WU \\ \rho WV \\ \rho W^2 + p \\ \rho WH \end{bmatrix} \tag{2}$$

and U, V, and W are component velocities in the three orthogonal coordinate directions, X, Y, and Z of a Cartesian coordinate system. Also, ρ is the local air density, p is the local air pressure, and E and H are given by:

$$E = \left(\frac{1}{\gamma - 1}\right)\left(\frac{p}{\rho}\right) + \frac{U^2 + V^2 + W^2}{2} \qquad H = E + \frac{p}{\rho} \tag{3}$$

2.2 FLO57 - EXPLICIT FINITE VOLUME FORMULATION

In FLO57 [13], the time dependent Euler equations are solved to obtain steady-state solutions as time asymptotes. The discretization scheme used by FLO57 is known as the finite volume method. In this method, the flow field is divided into small cells or control volumes. The Euler equations are satisfied in the average sense for each control volume. This is essentially solving the integral form of (1) which is

$$\int\int\int\left(\frac{\partial \hat{w}}{\partial t}+\frac{\partial \hat{f}}{\partial X}+\frac{\partial \hat{g}}{\partial Y}+\frac{\partial \hat{h}}{\partial Z}\right)dX\,dY\,dZ=0. \tag{4}$$

and which, for small cells, can be rewritten:

$$\frac{\partial}{\partial t}(\bar{w}h)+Q\hat{w}=0 \tag{5}$$

where h is the cell volume and Q is the operator for the steady-state residual calculation applied to the flow quantities. In other words, the rate of change of the flow quantities in each cell is equated to the net fluxes of those quantities across the cell walls. For the finite volume method, all of the flow quantities are defined at the center of the cells, rather than at the grid nodes at the cell corners. When evaluating fluxes, however, flow quantities on each face of the cell must be known. These quantities are approximated by making their values at the cell face equal to the average of quantities at the centers of the cells which share that face. Derivatives of flow quantities are approximated as differences between the quantities in adjacent cells.

In order to stabilize the solution, numerical viscosity is added to the formulation. In FLO57, the numerical viscosity is scaled by the

magnitudes of blended second and fourth derivatives of the flow quantities. With this damping added, the final form of (5) which is actually solved becomes:

$$\frac{\partial}{\partial t}(\hat{w}h) + Q\hat{w} - D\hat{w} = 0 \qquad (6)$$

where $D\hat{w}$ represents the sum of the numerical viscosity added for stability plus a viscosity-like numerical effect which results from the discretization of the flowfield and approximation of derivatives with finite differences. For simplicity in future discussions, the term "numerical viscosity" will be used in this work to refer to this sum of both effects.

The flow field is initialized with a uniform velocity distribution, the initial condition, and then a fourth order Runge-Kutta time-stepping scheme is used to advance to a steady state solution. The Runge-Kutta scheme uses a multi-level explicit integration scheme for computational efficiency. If equation (5) is rewritten

$$\frac{\partial \hat{w}}{\partial t} + P\hat{w} = 0$$

where

$$P\hat{w} = \frac{1}{h}(Q\hat{w} - D\hat{w}),$$

then, at time level n, the four stage scheme can be written

$$\hat{w}^{(0)} = \hat{w}^{n}$$

$$\hat{w}^{(1)} = \hat{w}^{(0)} - \frac{\Delta t}{2} P\hat{w}^{(0)}$$

$$\hat{w}^{(2)} = \hat{w}^{(0)} - \frac{\Delta t}{2} P\hat{w}^{(1)}$$

$$\hat{w}^{(3)} = \hat{w}^{(0)} - \Delta t P\hat{w}^{(2)}$$

$$\hat{w}^{n+1} = \hat{w}^{(0)} - \frac{\Delta t}{6}\left(P\hat{w}^{(0)} + 2P\hat{w}^{(1)} + 2P\hat{w}^{(2)} + P\hat{w}^{(3)}\right)$$

A single iteration involves sweeping through the entire flowfield and updating each flow quantity. The Runge-Kutta scheme does not require any matrix inversion for integration, but it allows larger time steps than other explicit Euler codes. Like other explicit schemes, the method also vectorizes easily on supercomputers.

2.3 ARC3D - IMPLICIT FINITE DIFFERENCE FORMULATION

Although it solves the same Euler equations as FLO57, the details of the formulation of ARC3D are different. The major features which distinguish ARC3D from FLO57 are a finite difference formulation instead of finite volume and an implicit time-stepping scheme. ARC3D also has the capability of solving the thin-layer approximation to the Navier-Stokes equations by including appropriate viscous terms.

The finite difference formulation of ARC3D differs from finite volume in that flow quantities are defined at the grid node points instead of at the cell centers. Like FLO57, ARC3D uses a centered differencing scheme to obtain spacial derivatives. Since flow quantities are not weighted by cell

areas as in FLO57, the flow equations are transformed from Cartesian coordinates into general curvilinear coordinates. The transformation metrics are generated numerically using finite differences.

The implicit time-stepping scheme of ARC3D is based on a method developed by Beam and Warming [22]. In this method, the equation to be solved is

$$\frac{\partial \hat{w}}{\partial t} + P\hat{w}^{n+1} = 0$$

which may be written

$$\hat{w}^{n+1} - \hat{w}^{n} + \Delta t P\hat{w}^{n+1} = 0.$$

If a correction is defined such that

$$\delta\hat{w} = \hat{w}^{n+1} - \hat{w}^{n},$$

then the equation to be solved can then be written

$$\delta\hat{w} + \Delta t\overline{P}\delta\hat{w} = (I + \Delta t\overline{P})\delta\hat{w} = -\Delta t P\hat{w}^{n}$$

where $\overline{P}$ is a linearized operator of P. This equation can be written as implicit and explicit portions to yield

$$N\delta\hat{w} = -\Delta t P\hat{w} \qquad (6)$$

where N is a correction operator defined in three dimensions such that

$$N = I + \Delta t \bar{P}.$$

The left half of equation (6) is implicit while the right-hand side is the explicit evaluation of the residual at time step n. The operator N is approximately factored into three one-dimensional operators, each of which can be inverted using a block tridiagonal matrix solver. This requires much less computational effort than inverting N, but computational effort per iteration is still much greater than in explicit schemes like FLO57. This extra work per iteration is generally offset by much larger time steps permitted by the implicit scheme. For problems considered in the present work, however, ARC3D typically took more computer time than FLO57 to reach the same level of convergence in the flow solution.

As in FLO57, numerical viscosity is added based on second and fourth derivatives of flow quantities. The second order dissipation is added implicitly to the left side of equation (6) to improve the practical stability bound. The fourth order term is added explicitly to the formulation.

The thin-layer approximations to the Navier-Stokes equations involve neglecting viscosity terms based on derivatives in the streamwise direction. As a result, they are not really valid for the case of a vortex core. Likewise, separated flow invalidates the thin-layer assumptions. For these reasons, the Navier-Stokes capabilities of ARC3D are not used to any great extent in the present effort.

2.4 BOUNDARY CONDITIONS

Appropriate boundary conditions must be specified to make a formulation complete. Three different types of boundary conditions are

implemented in the present work, farfield, solid wall and symmetry. At far field boundaries, just setting the flow quantities to free stream values is not normally acceptable. If such an approach is taken, the fixed quantities at the boundaries cause wave reflections at the boundary which propagate back into the flowfield. This can lead to errors and instability in the solution.

Instead of fixed free stream conditions at farfield boundaries, a characteristic boundary condition is used which is based on the theory of Kreiss [21]. If the flow is subsonic, this theory indicates that for boundaries which have incoming flow through them, all but one of the five needed flow quantities must be specified by the external flow. The one remaining quantity, usually pressure, is extrapolated from the interior so that sound waves can be allowed to escape. For farfield boundaries with outflow, on the other hand, only one quantity is specified by the exterior flow and the rest are extrapolated from the interior.

At solid surfaces, flow tangency is enforced for inviscid flow problems. This is done by setting the normal component of the flow velocity at the surface to zero. The pressure at the surface must also be known because it provides a momentum source to the boundary cells or nodes. The simplest approximation to the surface pressure is to equate it to the pressure at the boundary cell center or the adjacent node. A higher order estimate of surface pressure can be achieved by using the momentum equation normal to the surface to extrapolate pressure from the cell center or node down to the solid wall.

For planes of symmetry, a mirror image condition for all the flow quantities is enforced. As with inviscid solid surfaces, pressure at the plane of symmetry may be extrapolated from the interior using the momentum equation normal to the symmetry plane. This pressure may also be simply equated to the pressure at the adjacent boundary cell center or grid node.

2.5 GRIDS

Three types of grid topology are used in the present research. The first of these is a simple Cartesian grid in a rectangular box domain. A perspective view of one such grid is shown in Figure 2. The topology of such a grid is labeled H-H because boundaries at opposite ends of the box are parallel to each other like the two vertical legs of the letter H.

In discussing grid topology, it is helpful to refer to the i, j, k indices of a grid point instead of its physical coordinates, X, Y and Z. For Cartesian grids with unit spacing between nodes, there is no distinction between the two methods. However, as a grid is distorted to conform to more complex geometries, the X, Y, and Z coordinates of a given node may change, but the computational coordinates given by its i, j and k indices do not. The convention used in this work is that X and i directions run generally in the streamwise direction, Y and j run vertically, and Z and k run laterally in a direction that makes the XYZ coordinate system right handed. In FLO57, cells are indexed in the same way as grid nodes, except that ghost cells are added along the boundaries of the computational domain. As a result, the dimensions of the arrays storing flow quantities are larger by one in each direction than those for the grid.

Figure 3 shows a typical boundary cell on the lower surface of the rectangular box. Only i and j indices are shown for simplicity. Note that the j index of the cell is 2 because the ghost cell j index is 1. The grid nodes at the surface have a j index of 1 however. Similar relationships at the upstream and downstream boundaries cause a cell with a given i index to be between grid nodes with indices of i-1 and i. The H-H grid used in this work has an inviscid solid surface boundary condition on the j=1 face of the domain and a symmetry boundary condition on the k=1 face. Farfield boundary conditions are used on the other four faces.

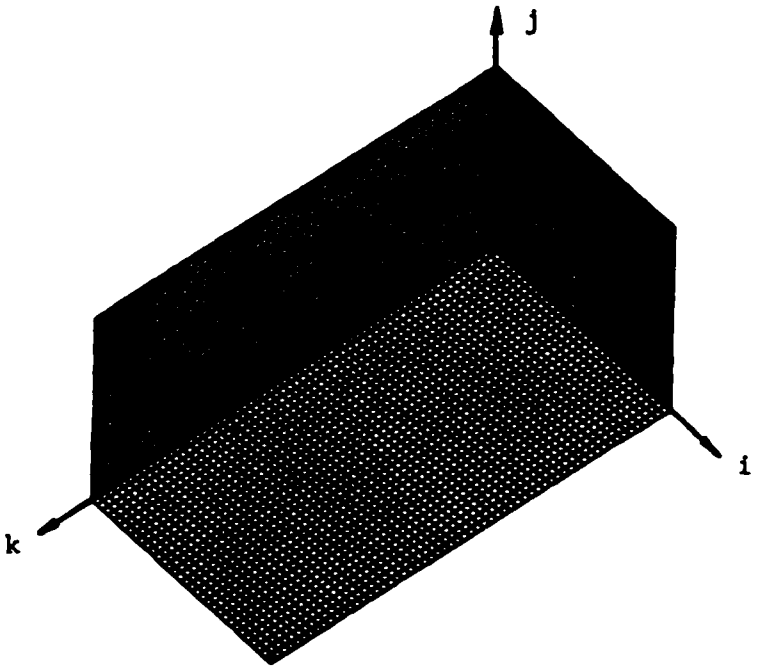

Figure 2. Perspective view of rectangular box grid.

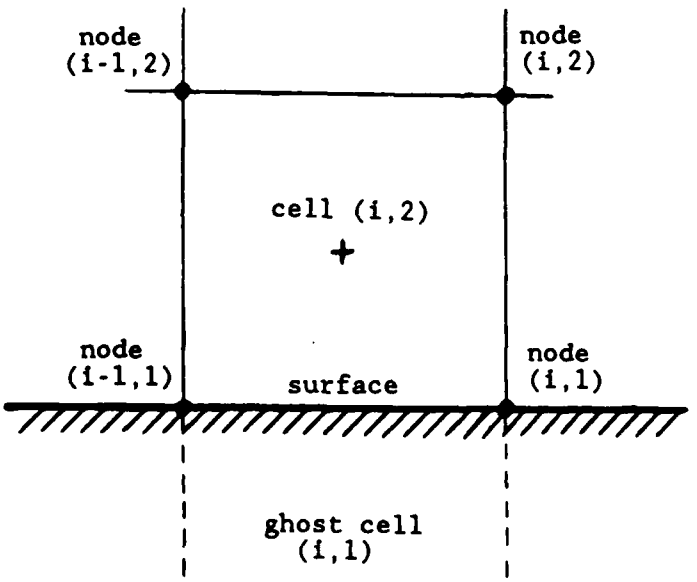

Figure 3. Boundary cell and grid indices.

A second grid is used for studies of leading edge vortices on delta wings. In this grid, the i=1 and i=imax faces remain at the upstream and downstream ends of the flowfield, parallel to each other as in the H-H grid. However, the lower surface of the grid is wrapped around the upper and lower surfaces of the delta wing, causing the two lateral side faces of the grid at k=1 and k=kmax to end up both being on the plane of symmetry, one on the top side of the wing and one on the bottom. In the region of the grid ahead of the apex of the delta wing, the j=1 surface of the grid is condensed into a single line. A perspective view of this grid and a planform view of a delta wing with the pattern of the grid on its surface are shown in Figure 4.

When the grid on the other side of the plane of symmetry is included, the j = constant grid lines on i = constant planes are circles or ellipses. For this reason, the topology of this grid is labeled H-O. The H implies that i = constant planes are still parallel as in the Cartesian grid while the O suggests the circular shape of the j = constant grid lines.

Boundary conditions for this grid differ from those of the H-H topology. In the H-O system, both k=1 and k=kmax faces require symmetry conditions. The j=1 surface has two types of boundary conditions. For i indices running from the apex of the delta wing to its trailing edge, a solid surface boundary condition is used. Upstream and downstream of the wing, a periodic boundary condition is used which recognizes the fact that a cell touching the j=1 surface of the top half of the grid is physically adjacent to another boundary cell with a higher k index on the lower half of the grid. Figure 5 shows a view of an i = constant plane of the grid downstream of the wing to make this relationship between the boundary cells more clear. The periodic condition can be handled easily by setting flow quantities in the upper cell of the periodic boundary equal to the flow quantities in the corresponding lower cell and vice versa for FLO57, and by

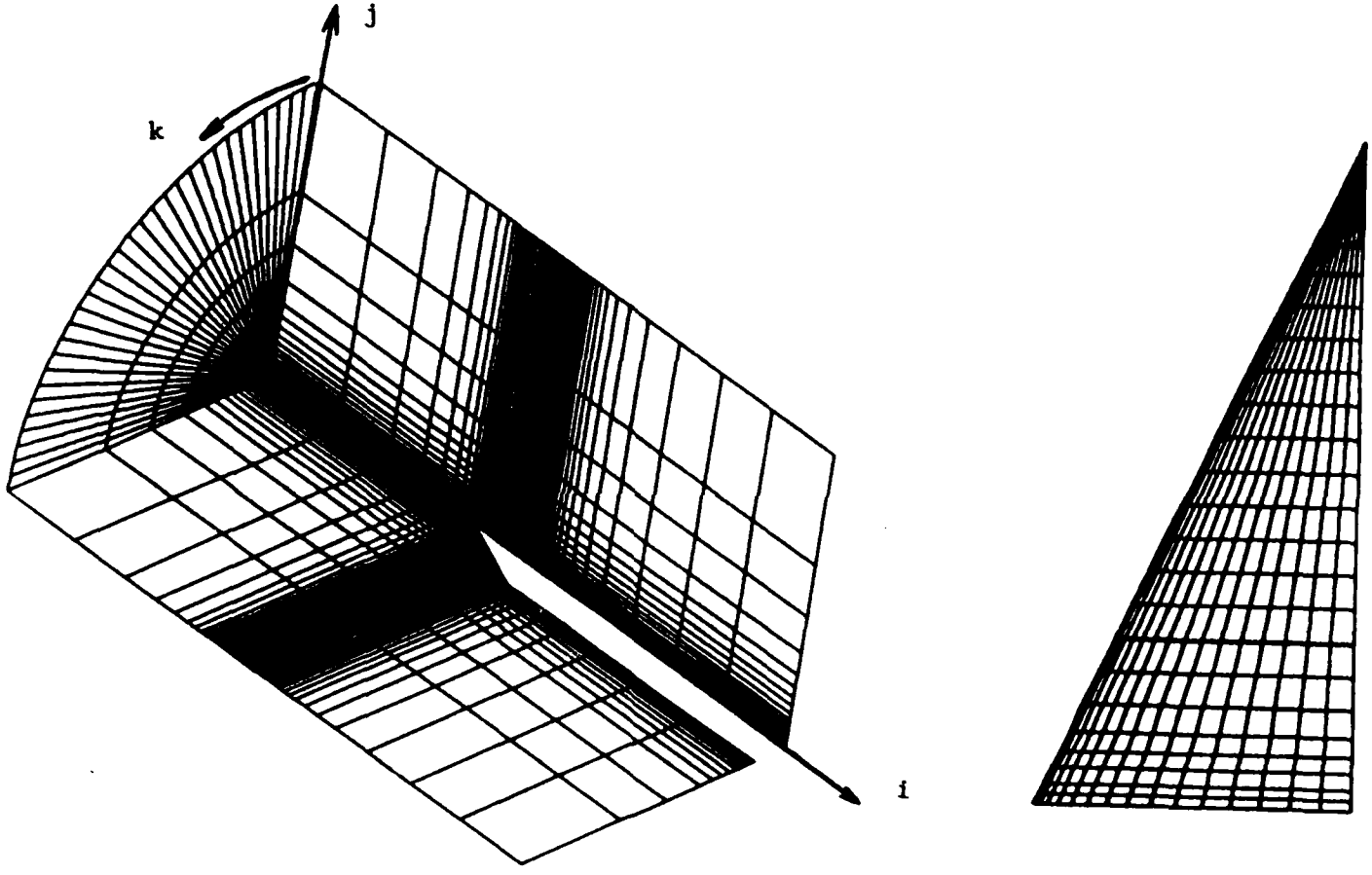

Figure 4. Perspective view of H-O grid and planform view of delta wing.

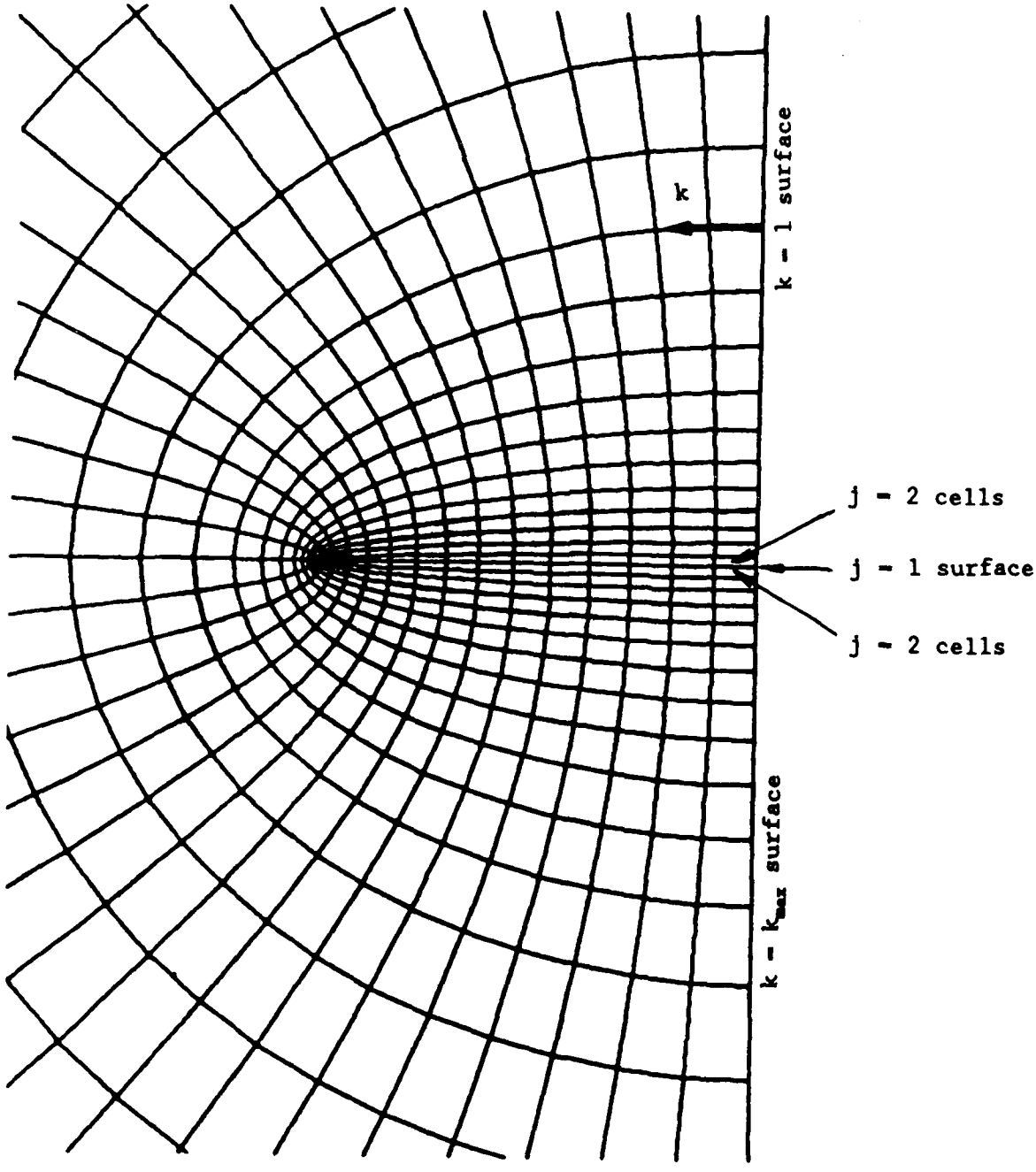

Figure 5. View from downstream of i = 45 plane of H-O grid.

making an appropriate arrangement between the upper and lower grid nodes for ARC3D. Farfield boundary conditions are used for the rest of the boundaries.

The third grid topology used is labeled C-H. As the name implies, the streamwise direction of the grid is folded into a C shape while the spanwise direction remains similar to the rectangular box. Figure 6 shows a view of the k=1 plane along with a wing planform view and grid pattern for a C-H grid used in the present work. The C shape of the k=1 plane is apparent. It is also apparent from Figure 6 that, as in the H-O mesh, two different boundary conditions are needed for the j=1 surface.

The i index in this topology starts at the lower half of the downstream end of the grid, increases moving forward and wrapping around the wing leading edge, and ends at the upper half of the downstream end. For those cells which lie on the wing surface, a solid surface boundary condition is used. A periodic boundary condition is used for the remaining cells on this boundary. This includes all cells on this surface for k greater than the k value of the wingtip, and for k less than k of the wingtip, all cells downstream of the wing trailing edge. Another boundary condition in the C-H topology which differs from those in either H-H or H-O meshes is the i=1 boundary. Since the i=1 surface is downstream of the wing in a C-H mesh, it is given an outflow farfield boundary condition.

2.6 SPECIAL CONCERNS FOR VORTEX FLOWS

When a vortex is present in an Euler solution, numerical viscosity and grid density work together to determine vortex core size. Rizzi(19) made Euler simulations of leading edge vortex flows on delta wings using a range

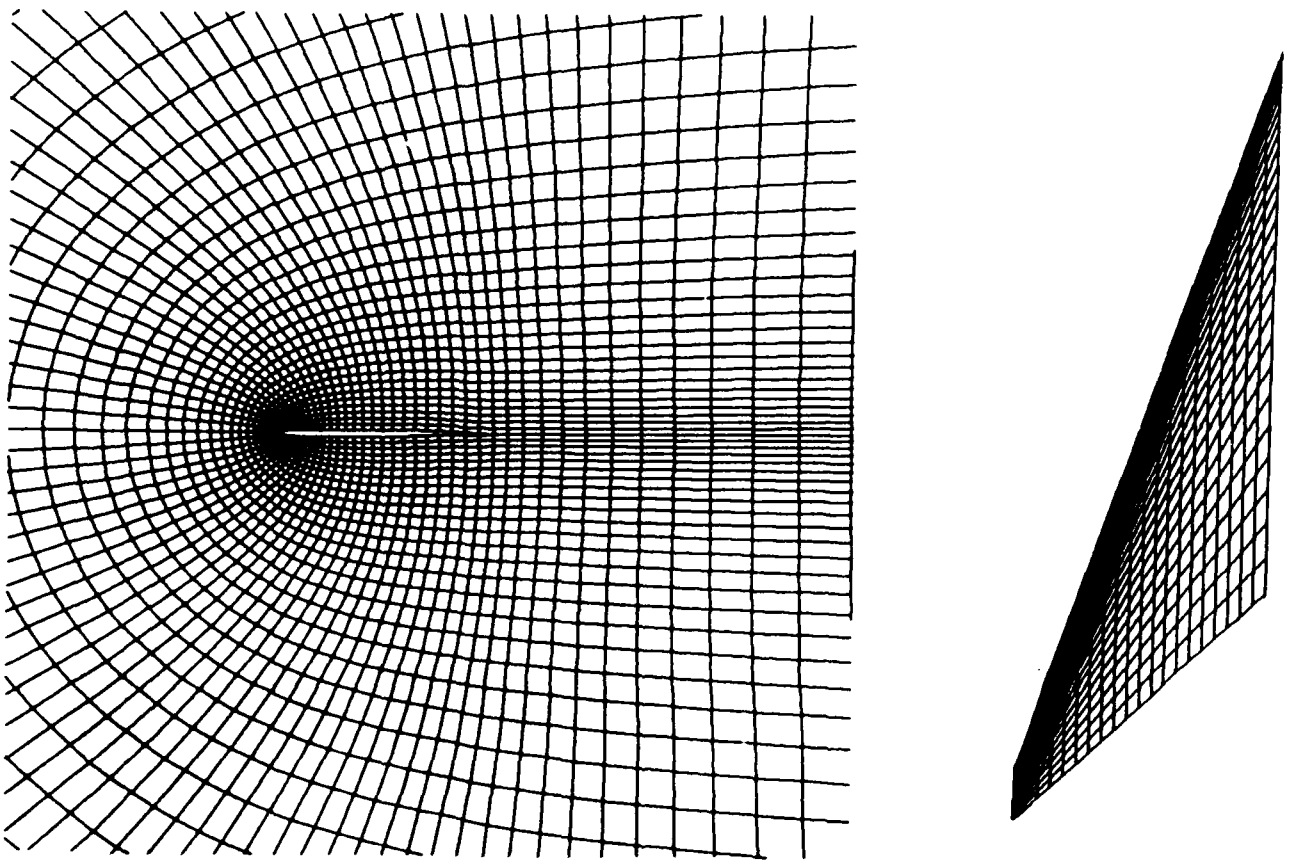

Figure 6. Wing planform view and view from wingtip of k = 1 plane of C-H grid.

of grid sizes from coarse to very fine. He found that for a medium density grid, surface pressure distributions on the wing surface matched well with wind tunnel experiments. For grids which were coarser than this, however, he found that the expansion peaks in the surface pressure curves were more spread out and the absolute value of their minimum pressure coefficients were reduced. This result suggests that the vortex core in the coarse grid Euler solution was larger than the core in the medium grid solution and the wind tunnel tests. When Rizzi ran simulations on the very fine grid, the absolute value of the minimum pressure coefficient on the wing was much greater than for the wind tunnel tests, and the region of the wing effected by the vortex was smaller. This result implied that the very fine grid allowed a vortex which was smaller than in the physical experiment.

This dependence on grid density for sizing of the vortex core is a very undesirable feature of vortex flowfield analyses using Euler solvers as well as Navier-Stokes codes. Not only does core size effect the pressure distribution on the wing surface, but if the cell size changes along the length of the vortex, the resulting change in core size can produce an axial pressure gradient. This, in turn, can contribute to the development of an axial jet or velocity defect, depending on the direction of the gradient. Because these effects are numerical rather than based on the physics of the problem, the usefulness of Euler solvers for vortex research is jeopardized.

In addition, the use of different surface boundary conditions is significant for problems involving the formation of leading edge vortices on wings with rounded leading edges. Figure 7 shows an example of this for a wing with a leading edge sweep angle of 71.2 degrees and a NACA 0012 airfoil. The figure shows a crossflow plane cut of the wing with crossflow velocity vectors drawn for two flow solutions from FLO57 at eighteen degrees angle of attack. The solution on the top was obtained by

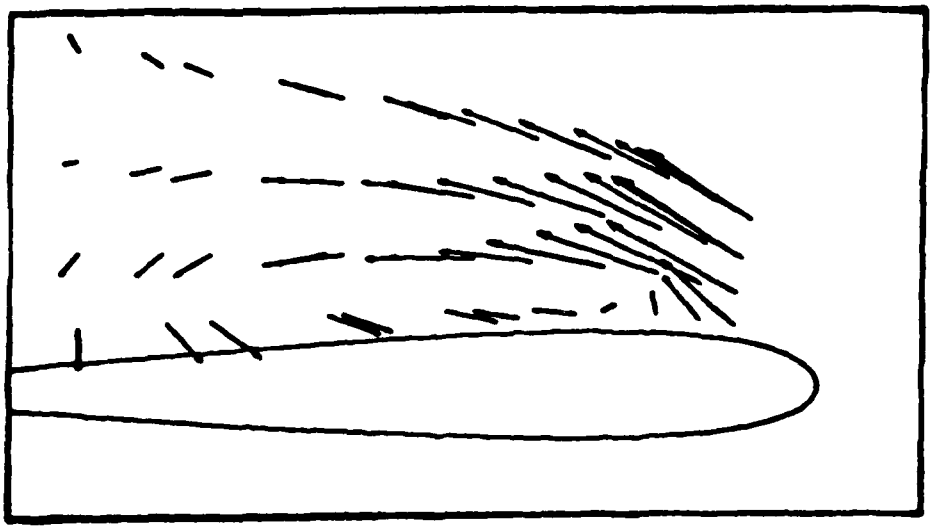

Crossflow Velocity Vectors
Angle of Attack is 18 Degrees
$P_{surface} = P_{cell}$ Boundary Condition

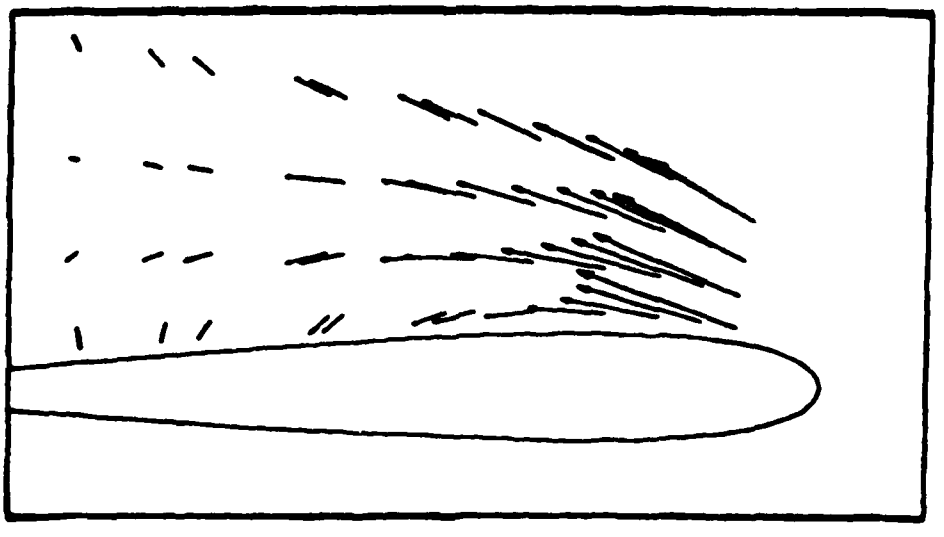

Crossflow Velocity Vectors
Angle of Attack is 18 Degrees
Normal Momemtum Equation Boundary Condition

Figure 7. Effect of surface boundary condition on vortex rollup

extrapolating surface pressures from the boundary cell centers to the wing surface using the momentum equation normal to the surface, while the one on the bottom came from setting the surface pressure equal to the boundary cell pressure. As can be seen, the normal momentum equation boundary condition prevented the vortex from developing. These numerical difficulties with the formulation of Euler solvers and the choice of grids limit the degree to which they can be used in vortical flow research.

CHAPTER 3

MODEL DEVELOPMENT

3.1 VORTEX CORE MODEL

A model for the vortex core is derived from the steady, incompressible Navier-Stokes equations written for the cylindrical coordinate system centered on a vortex core. The modeling process is similar to that developed by Mager [27] and Krause, [28] but the present model includes approximations for non-axisymmetric wall effects. The vortex is assumed to be slender and close to a wing surface and a plane of symmetry. The velocity components u, v, and w are defined along the x, r, and θ coordinates which correspond to axial, radial, and circumferential directions. With these assumptions, the Navier-Stokes equations can be written:

$$\frac{\partial u}{\partial x}+\frac{\partial v}{\partial r}+\frac{v}{r}+\frac{1}{r}\frac{\partial w}{\partial \theta} = 0 \tag{7a}$$

$$u\frac{\partial u}{\partial x}+v\frac{\partial u}{\partial r}+\frac{w}{r}\frac{\partial u}{\partial \theta} = -\frac{1}{\rho}\frac{\partial p}{\partial x}+\frac{\mu}{\rho}\left(\frac{\partial^2 u}{\partial x^2}+\frac{\partial^2 u}{\partial r^2}+\frac{1}{r}\frac{\partial u}{\partial r}+\frac{1}{r^2}\frac{\partial^2 u}{\partial \theta^2}\right) \tag{7b}$$

$$u\frac{\partial v}{\partial x}+v\frac{\partial v}{\partial r}+\frac{w}{r}\frac{\partial v}{\partial \theta}-\frac{w^2}{r} = -\frac{1}{\rho}\frac{\partial p}{\partial r}$$

$$+\frac{\mu}{\rho}\left(\frac{\partial^2 v}{\partial x^2}+\frac{\partial^2 v}{\partial r^2}+\frac{1}{r}\frac{\partial v}{\partial r}-\frac{v}{r^2}+\frac{1}{r^2}\frac{\partial^2 v}{\partial \theta^2}-\frac{2}{r^2}\frac{\partial w}{\partial \theta}\right) \tag{7c}$$

$$u\frac{\partial w}{\partial x}+v\frac{\partial w}{\partial r}+\frac{w}{r}\frac{\partial w}{\partial \theta}+\frac{vw}{r} = -\frac{1}{\rho r}\frac{\partial p}{\partial \theta}$$

$$+\frac{\mu}{\rho}\left(\frac{\partial^2 w}{\partial x^2}+\frac{\partial^2 w}{\partial r^2}+\frac{1}{r}\frac{\partial w}{\partial r}-\frac{w}{r^2}+\frac{1}{r^2}\frac{\partial^2 w}{\partial \theta^2}+\frac{2}{r^2}\frac{\partial v}{\partial \theta}\right) \tag{7d}$$

where p is the pressure, ρ is the density, and μ is the air viscosity. In a manner similar to boundary layer analysis, a small parameter, ϵ is defined by the equation

$$\epsilon = \frac{\delta_{ref}}{L}$$

where L is the reference axial length scale of the vortex and δ_{ref} is the vortex core radius at x = L. It is further assumed that the ratios of radial distances and velocities to their axial counterparts are also of the same order as ϵ. To non-dimensionalize equations (7), x is normalized by L, but r is normalized by ϵ L. In this way the very small radial

coordinate is scaled to be of the same order of magnitude as the axial coordinate. In a similar manner, u and w are normalized by the free stream velocity, U_∞, but v is normalized by ϵU_∞. Pressure is normalized by free stream dynamic pressure, ρU_∞^2. In addition, the vortex Reynolds number is defined as

$$Re = \frac{\rho U_\infty L}{\mu}$$

When the non-dimensional variables are substituted into equations (7) and common multiples of L, U_∞ and ϵ are divided out the equations can be written

$$\frac{\partial u}{\partial x} + \frac{\partial v}{\partial r} + \frac{v}{r} + \frac{1}{\epsilon r}\frac{\partial w}{\partial \theta} = 0 \tag{8a}$$

$$u\frac{\partial u}{\partial x} + v\frac{\partial u}{\partial r} + \frac{w}{\epsilon r}\frac{\partial u}{\partial \theta} = -\frac{\partial p}{\partial x} + \frac{1}{Re\epsilon^2}\left(\epsilon^2\frac{\partial^2 u}{\partial x^2} + \frac{\partial^2 u}{\partial r^2} + \frac{1}{r}\frac{\partial u}{\partial r} + \frac{1}{r^2}\frac{\partial^2 u}{\partial \theta^2}\right) \tag{8b}$$

$$\epsilon^2\left(u\frac{\partial v}{\partial x} + v\frac{\partial v}{\partial r}\right) + \frac{\epsilon w}{r}\frac{\partial v}{\partial \theta} - \frac{w^2}{r} = -\frac{\partial p}{\partial r} + \frac{1}{Re}\left(\epsilon^2\frac{\partial^2 v}{\partial x^2} + \frac{\partial^2 v}{\partial r^2} + \frac{1}{r}\frac{\partial v}{\partial r} - \frac{v}{r^2} + \frac{1}{r^2}\frac{\partial^2 v}{\partial \theta^2} - \frac{2}{\epsilon r^2}\frac{\partial w}{\partial \theta}\right) \tag{8c}$$

$$u\frac{\partial w}{\partial x} + v\frac{\partial w}{\partial r} + \frac{w}{\epsilon r}\frac{\partial w}{\partial \theta} + \frac{vw}{r} = -\frac{1}{\epsilon r}\frac{\partial p}{\partial \theta} + \frac{1}{Re\epsilon^2}\left(\epsilon^2\frac{\partial^2 w}{\partial x^2} + \frac{\partial^2 w}{\partial r^2} + \frac{1}{r}\frac{\partial w}{\partial r} - \frac{w}{r^2} + \frac{1}{r^2}\frac{\partial^2 w}{\partial \theta^2} + 2\frac{\epsilon}{r^2}\frac{\partial v}{\partial \theta}\right) \tag{8d}$$

Next, the parameter ϵ is assumed to scale with the inverse of the square root of the Reynolds number. For very large Reynolds numbers, it is therefore assumed that terms of order ϵ^2, $1/Re$, ϵ, and $1/(Re\,\epsilon)$ are negligible. After eliminating these terms, the equations of motion become:

$$\frac{\partial u}{\partial x}+\frac{\partial v}{\partial r}+\frac{v}{r}+\frac{1}{\epsilon r}\frac{\partial w}{\partial \theta} = 0 \tag{9a}$$

$$u\frac{\partial u}{\partial x}+v\frac{\partial u}{\partial r}+\frac{w}{r}\frac{\partial u}{\partial \theta} = -\frac{\partial p}{\partial x}+\frac{1}{Re\epsilon^2}\left\{\frac{1}{r}\frac{\partial}{\partial r}\left(r\frac{\partial u}{\partial r}\right)+\frac{1}{r^2}\frac{\partial^2 u}{\partial \theta^2}\right\} \tag{9b}$$

$$\frac{w^2}{r} = \frac{\partial p}{\partial r} \tag{9c}$$

$$u\frac{\partial w}{\partial x}+v\frac{\partial w}{\partial r}+\frac{w}{\epsilon r}\frac{\partial w}{\partial \theta}+\frac{vw}{r} = -\frac{1}{\epsilon r}\frac{\partial p}{\partial \theta} + \frac{1}{Re\epsilon^2}\left\{\frac{\partial}{\partial r}\left(\frac{1}{r}\frac{\partial}{\partial r}(rw)\right)+\frac{1}{r^2}\frac{\partial^2 w}{\partial \theta^2}\right\} \tag{9d}$$

The above equations are integrated algebraically by defining radial distributions or profiles of the axial and circumferential velocities within the core. A number of profiles which have been used for this purpose are described in Appendix A. Since all of these profiles are axisymmetric, derivatives in the circumferential direction for these profiles are zero, and the equations to be integrated reduce to

$$\frac{\partial u}{\partial x}+\frac{\partial v}{\partial r}+\frac{v}{r} = 0$$

$$u\frac{\partial u}{\partial x}+v\frac{\partial u}{\partial r} = -\frac{\partial p}{\partial x}+\frac{1}{Re\epsilon^2}\left\{\frac{1}{r}\frac{\partial}{\partial r}\left(r\frac{\partial u}{\partial r}\right)\right\}$$

$$\frac{w^2}{r} = \frac{\partial p}{\partial r}$$

$$u\frac{\partial w}{\partial x}+v\frac{\partial w}{\partial r}+\frac{vw}{r} = \frac{1}{Re\epsilon^2}\left\{\frac{\partial}{\partial r}\left(\frac{1}{r}\frac{\partial}{\partial r}(rw)\right)\right\}$$

In many of the velocity profiles, such as the Rankine vortex, the radial velocity, v, is also assumed to be zero. This further simplifies the formulation. For the purposes of the present work, v is generally not assumed to be zero, and the vortices are only assumed to be nearly axisymmetric, so that derivatives in the circumferential direction are small but not necessarily zero.

To include non-axisymmetric wall effects, the concept of image vortices is used. The non-axisymmetric velocity profiles for a vortex near a wall are approximated by adding to the axisymmetric profiles the velocities induced by the image vortices. In order to facilitate evaluation of the image vortex velocities, a wing-centered Cartesian coordinate system is defined with X, Y, and Z as chordwise, vertical, and spanwise coordinates respectively. This Cartesian coordinate system is the same as that used by the Euler solver. Figure 8 illustrates the relationship between the vortex-centered $xr\theta$ system and the Cartesian system. In the XYZ system, two non-dimensional distances and two angles are defined as follows:

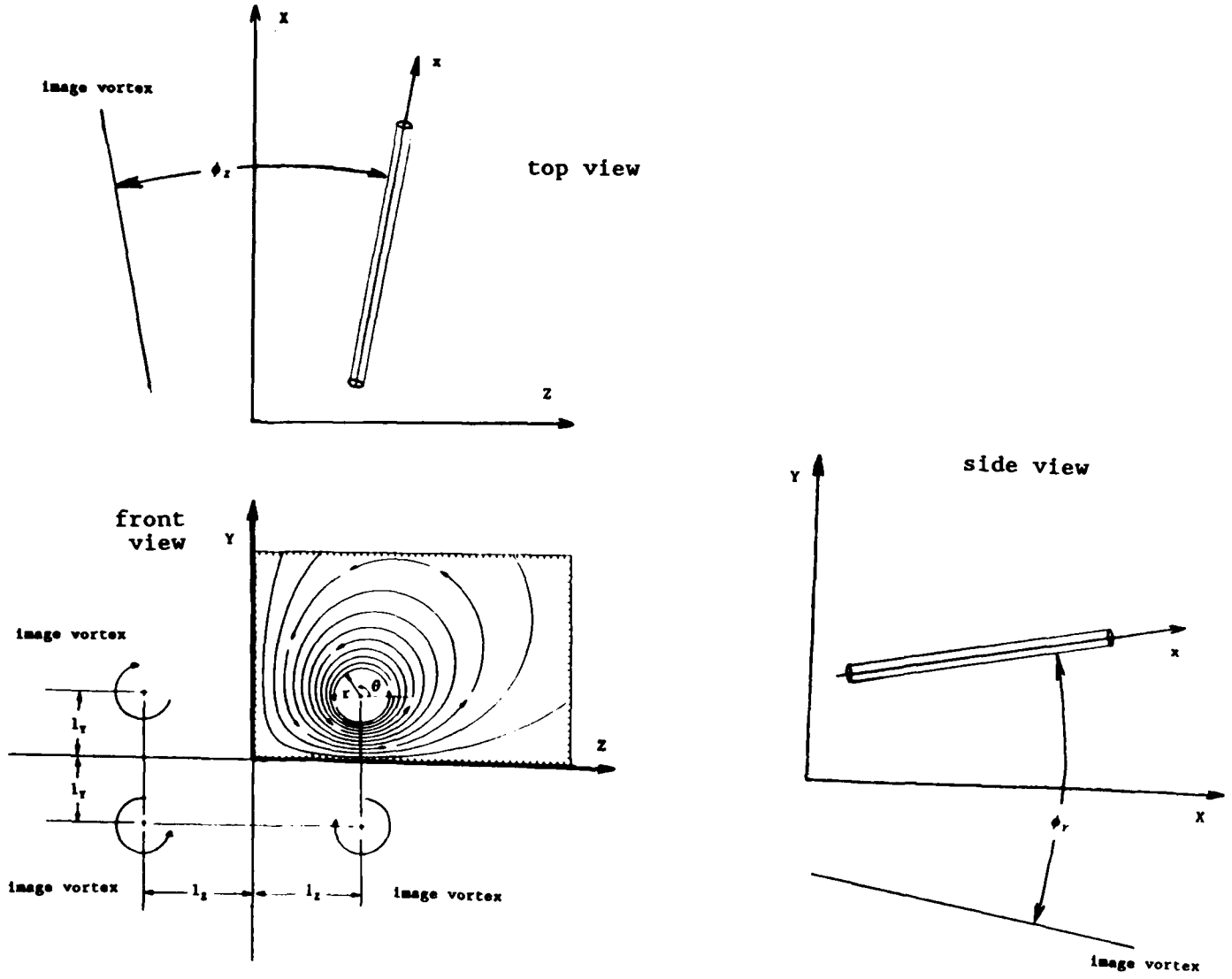

Figure 8. Coordinate system relationships.

$$l_Y = \frac{Y_{core} - Y_{wing}}{\delta_{ref}} \qquad l_Z = \frac{Z_{core} - Z_{symm}}{\delta_{ref}}$$

$$\phi_Y = 2\tan^{-1}\left(\frac{dl_Y}{dX}\right) \qquad \phi_Z = 2\tan^{-1}\left(\frac{dl_Z}{dX}\right).$$

Figure 8 also illustrates these distances and angles. For infinite image vortices, the induced v and w velocities in the vortex coordinate system are given by

$$v_i = -\frac{\Gamma}{2\pi}\left\{\cos\phi_Y\left(\frac{2l_Y\cos\theta}{r^2+4l_Yr\sin\theta+4l_Y^2}-\frac{\cos\theta}{2l_Y}\right)+\cos\phi_Z\left(\frac{2l_Z\sin\theta}{r^2-4l_Zr\cos\theta+4l_Z^2}-\frac{\sin\theta}{2l_Z}\right)\right\}$$

$$+\frac{\Gamma}{2\pi}\cos\phi_Y\cos\phi_Z\left(\frac{2l_Y\cos\theta+2l_Z\sin\theta}{r^2+4l_Yr\sin\theta-4l_Zr\cos\theta+4l_Y^2+4l_Z^2}-\frac{l_Y\cos\theta+l_Z\sin\theta}{l_Y^2+l_Z^2}\right) \qquad (10a)$$

$$w_i = -\frac{\Gamma}{2\pi}\left\{\cos\phi_Y\left(\frac{r+2l_Y\sin\theta}{r^2+4l_Yr\sin\theta+4l_Y^2}-\frac{\sin\theta}{2l_Y}\right)+\cos\phi_Z\left(\frac{r-2l_Z\cos\theta}{r^2-4l_Zr\cos\theta+4l_Z^2}+\frac{\cos\theta}{2l_Z}\right)\right\}$$

$$+\frac{\Gamma}{2\pi}\cos\phi_Y\cos\phi_Z\left(\frac{r+2l_Y\sin\theta-2l_Z\cos\theta}{r^2+4l_Yr\sin\theta-4l_Zr\cos\theta+4l_Y^2+4l_Z^2}-\frac{l_Y\sin\theta-l_Z\cos\theta}{l_Y^2+l_Z^2}\right) \qquad (10b)$$

See Appendix B for a derivation of equations (10).

For the problems considered in the present work, ϕ_Y is small and l_Z is large compared with l_Y. Image vortex induced u velocities are therefore ignored. The image vortex induced w velocity is added to the chosen axisymmetric w profile to obtain the total w velocity distribution.

With the circumferential velocity profile specified, equation (9c) is

integrated from the vortex center, r = 0, to the edge of the core, r = δ. After removing negligible terms, the relationship between the pressure at the core edge and pressure at the vortex center is given by

$$p(x,0) = p(x,\delta) - K_a \frac{\Gamma^2}{a} + K_i \Gamma^2 C_\phi . \qquad (11)$$

where the vortex core area, a and the circulation, Γ are defined as

$$a = \pi\delta^2 \qquad \text{and} \qquad \Gamma = 2\pi\delta w_\theta$$

respectively, and C_ϕ is the wall effect parameter given by

$$C_\phi = \frac{\cos\phi_Y}{l_Y^2} + \frac{\cos\phi_Z}{l_Z^2} - \frac{\cos\phi_Y \cos\phi_Z}{l_Y^2 + l_Z^2} . \qquad (12)$$

The coefficients K_a and K_i depend on the choice of the circumferential velocity profile. In addition, for cases where the image vortices are not infinite, the value of K_i is reduced to approximate this fact. An example of the evaluation of K_a and K_i for the case of a Rankine vortex plus the image vortex velocities is given in Appendix D.

The v velocity profile is next obtained by integrating equation (9a) in the radial direction. To simplify this process, the equation is first integrated using the axisymmetric u and w profiles to obtain v for the axisymmetric case. The non-axisymmetric v defined by equation (10a) is then added to the axisymmetric v. An example of this process is also given in Appendix D. With the profiles for the three components of velocity known, equation (9d) is integrated over the area of the vortex core to obtain:

$$\frac{1}{a}\frac{da}{dx} = \frac{K_1}{\Gamma}\frac{d\Gamma}{dx} - \frac{K_2}{u_\delta}\frac{du_\delta}{dx} + \frac{K_3}{Re\epsilon^2 a u_\delta} \qquad (13)$$

where the values of K_1, K_2, and K_3 depend on the velocity profiles chosen. For the Rankine vortex circumferential velocity profile, K_2 and K_3 are zero and K_1 is one. In this case, equation (13) gives

$$a \propto \Gamma$$

which implies that core area increases linearly with vortex strength. In the velocity profiles defined by Mager, K_1 and K_2 are not constants but depend on the form parameter of the axial velocity profile. This form parameter varies upstream of bursting from 1 for a uniform axial flow to 0 when stagnation occurs at the vortex center. See Appendix D for an example of the effect this has on equation (13). In order to simplify the model, average values of K_1 and K_2 are used.

For such complex velocity profiles as Mager's, it is more difficult to integrate equation (13). Two extreme cases are considered, each of which permits (13) to be integrated easily. First, it is assumed that vortex strength is increasing rapidly and the viscous term of (13) can be neglected. For this case the equation can be integrated to give

$$a = K_4 \frac{\Gamma^{K_1}}{u_\delta^{K_2}}.$$

where K_4 is a constant of integration. On the other hand, consider a case where vortex strength and velocity at the core edge are constant. For these assumptions, equation (13) would be solved by

$$a = \frac{K_3}{Re\epsilon^2}\frac{(x-x_o)}{u_\delta}$$

where x_o is a constant of integration. By choosing a suitable coefficient K_5 to replace K_3 the above expression for core area could be written

$$a = K_5\frac{\Gamma(x-x_o)}{u_\delta}$$

Based on these two results, the following approximate model for core growth is defined:

$$a = K_g\frac{\Gamma^{K_1}(x-x_o)}{u_\delta^{K_2}} \tag{14}$$

where K_g is a core growth parameter which depends on the velocity profiles and the product $Re\,\epsilon^2$.

Next, the circumferential velocity profile is assumed to be close to that of a Rankine vortex, so the radial distribution of pressure in the vortex core can be approximated by

$$p(x,r) = p(x,0) + \left(\frac{r}{\delta}\right)^2 (p(x,\delta) - p(x,0)). \tag{15}$$

Using equations (11) and (15), equation (9b) is integrated over the area of the core to give

$$u_0\frac{du_0}{dx}+\frac{dp_0}{dx} = -K_a\left(\frac{\Gamma}{a}\frac{d\Gamma}{dx}-\frac{\Gamma^2}{a^2}\frac{da}{dx}\right)$$

$$+K_t\left(\Gamma\frac{d\Gamma}{dx}C_\phi-\frac{\Gamma^2}{2a}\frac{da}{dx}C_\phi+\frac{\Gamma^2}{2}\frac{dC_\phi}{dx}\right) \qquad (16)$$

where the subscript 0 designates core center values. It is worthwhile to point out that the contribution of the viscous term disappears in the integration if the axial velocity profile is defined as in Mager's profile with zero slopes at the center and the edge of the core.

If the velocity profiles of the viscous core and those in Euler solutions are similar, then the major discrepancy of the Euler formulation is primarily due to the non-physical estimation of core size and core growth rate. Therefore, the non-physical vortex core in Euler solutions can be replaced with a core that is derived from viscous physics, as given in equation (16). This is in effect equivalent to an addition of the difference between the model and the Euler solution as a source term into the Euler formulation. The difference can be given as

$$\left(u_0\frac{du_0}{dx}+\frac{dp_0}{dx}\right)-\left(u_0\frac{du_0}{dx}+\frac{dp_0}{dx}\right)_E$$

$$= -K_a\left\{\frac{\Gamma}{a}\frac{d\Gamma}{dx}\left(1-\frac{a}{a_E}\right)-\frac{\Gamma^2}{a^2}\left(\frac{da}{dx}-\frac{a^2}{a_E^2}\frac{da_E}{dx}\right)\right\}$$

$$-K_t\frac{\Gamma^2}{2a}C_\phi\left(\frac{da}{dx}-\frac{a}{a_E}\frac{da_E}{dx}\right) \qquad (17)$$

where the subscript E denotes flow quantities measured in the Euler solution.

Equation (17) provides momentum source terms for use in the Euler solver. Because the vortex x axis is not alligned with the wing X axis, components of the source term for each cell must be applied to the X, Y, and Z momentum equations in the Euler solver.

3.2 SHEAR LAYER MODEL

The viscous shear layer next to a highly swept wing at a large angle of attack is too complex to model with simple physics. The flowfield involves many difficult features including the mechanism for leading edge separation and creation of leading edge vortices, reattachment of the flow around the primary vortex, appearance of a secondary vortex separation, etc. As a simple approximation of these complexities, an analogy is made to the boundary layer on a flat plate. Boundary layer separation can be explained as being caused by loss of total pressure in the boundary layer due to viscosity. This same concept is extended to explain leading edge separation on a highly swept rounded leading edge. Total pressure loss in a boundary layer is approximated as being of such a magnitude that static pressure at the boundary layer edge is equal to the pressure at the flat plate surface. For the rounded leading edge, an effective shear layer thickness is defined such that total pressure losses satisfy this same equality of static pressures at the shear layer edge and at the surface. The magnitude of this effective thickness will be different than for a flat plate boundary layer. It is assumed, however, that the growth profile of the effective shear layer thickness can be approximated by a simple modification to the well known equation for turbulent boundary layer growth on a flat plate given by Schlichting [38]. The modified equation is written

$$\delta_s = \frac{K_t l}{(Re_{local})^{0.2}} \tag{18}$$

where Re_{local} is the local Reynolds number based on the distance l measured from the apex of the delta wing and δ_s is the effective shear layer thickness. The coefficient K_t is an effective thickness parameter which equals 0.37 for a flat plate, but which is much greater for the round leading edge. This shear layer thickness effect is incorporated into the Euler solver by modifying the normal momentum equation boundary condition. Instead of extrapolating pressure from the cell center all the way to the wing surface, the modified boundary condition uses the relation

$$p_{wall} = p_{cell} - \frac{dp}{dn}(\Delta n - \delta_s) \tag{19}$$

where p_{cell} is the pressure at the center of the boundary cell, dp/dn is the pressure gradient in the direction normal to the surface, and Δn is the normal distance between the surface and the cell center.

In addition to corrections for the surface pressure, the analogy with the flat plate boundary layer is used to calculate momentum source terms for the boundary cells. These source terms are similar to those calculated by the vortex core model. They represent the net momentum loss experienced by the boundary cells due to the shear layer. If the entire shear layer is contained within the boundary cells, the skin friction coefficient, C_f, is a measure of this momentum transfer from the fluid in the boundary cell to the wing surface. Using the analogy with a flat plate boundary layer once again, the equation for C_f in the shear layer is approximated as

$$C_f = \frac{K_s}{(Re_{local})^{0.2}}. \tag{20}$$

K_s in equation (20) is a wall shear stress parameter which equals 0.074 for a flat plate boundary layer. The shear stress source terms are added into the momentum equations in a direction parallel to the local velocity in each boundary cell.

3.3 MODEL IMPLEMENTATION

The vortex core model is incorporated into the Euler solver as a separate subroutine which is accessed periodically. The control parameters K_g, K_a, and K_i are input into the program by the user and used unchanged throughout the solution process. The exponents K_1 and K_2 in equation (14) are both assumed to be approximately equal to 1. The total circulation or vortex strength and the Euler vortex core size are determined from the Euler solution at axial locations along the vortex corresponding to convenient locations in the Euler grid. The vortex strength is obtained by evaluating the vorticity flux through the surfaces of each cell and summing them. The area of the vortex core is measured from the cross sectional areas of the cells which contain vorticity of strength above a given threshold level. The center of the vortex at each axial station is identified as the cell with a local minimum static pressure and a local maximum vorticity flux. Locating the vortex center establishes the values of C_ϕ in equation (12). The axial momentum source terms at each axial position along the vortex are then obtained from equation (17).

When the momentum source terms are added in, the equation solved by the Euler code is of the form

$$\frac{\partial}{\partial t}(h\hat{w}) + Q\hat{w} - D\hat{w} - S = 0$$

where the S term represents the momentum sources from the core model. To avoid destabilizing the solution, source terms are not just applied to the cell at the vortex center. Terms for neighboring cells are scaled in accordance with their distance from the center following a profile similar to the axial velocity profiles used by Mager. In order to reduce computational costs, these corrections are updated only once every 30 to 50 iterations.

The new boundary condition is incorporated into the Euler solver by modifying the surface boundary condition subroutine. The desired values of effective thickness parameter and shear stress parameter are input to the program. These values are used to calculate the effective viscous layer thickness for each boundary cell using equation (18). The pressure at the surface is then defined using equation (19). Momentum source terms for the boundary cells are scaled by the local values of skin friction coefficient given by equation (20).

CHAPTER 4

CORE MODEL EVALUATION

4.1 RECTANGULAR GRID EXPERIMENT

A simple computational experiment was performed which simulated a vortex near an infinite flat plate and a plane of symmetry. The experiment had three purposes. The first of these was to identify some of the characteristics of Euler codes which cause problems in vortex simulations. The second was to evaluate some of the assumptions and approximations used in developing the vortex core model. The third purpose was to provide a simple computational problem for the first tests of the vortex core model.

A computational grid was defined in the shape of a rectangular box. The flowfield within the box was initialized with a uniform flow parallel to the top, bottom, and sides of the box. To this was added a vortex whose axis ran parallel to the uniform flow. This vortex flowfield was also used as an inflow boundary condition on the upstream end of the box. A solid surface boundary condition was imposed on the bottom surface of the box and

one of the sides of the box was made a plane of symmetry. The other three box faces were given farfield boundary conditions.

The motivation of this study was to isolate the difficult computational issues arising from the complicated geometries and flowfields associated with delta wings. Such factors as leading edge separation, vortex rollup, and the pressure fields associated with wing airfoil shapes were completely excluded from the test. Other factors such as vortex strength, location, and core size could be controlled individually. The two different Euler solvers discussed in Chapter 2 were used in the tests. Both gave essentially the same results.

The first test involved initializing the flow field with a potential vortex. In order to avoid a singularity at the vortex center, the vortex was centered on a grid node so that induced velocities at the cell centers were finite for FLO57 and vice versa for ARC3D. This caused the entire flow field to be initially irrotational. This velocity distribution could also be regarded as that from a Rankine vortex with a core diameter equal to the width of a single grid cell. The velocity fields induced by three image vorticies were also added to the initialization so that normal velocities at the flat plate and the plane of symmetry were zero. When the Euler code was run, the action of the numerical viscosity in the flow solver caused the vortex core to enlarge to cover a region eight to ten cells in diameter. This growth in core size occurred within the first 2 cells downstream of the upstream boundary. Total swirl or vortex strength was conserved, so maximum circumferential velocity in the vortex decreased dramatically in this relatively short downstream distance. The reduction in maximum circumferential velocity was accompanied by an increase in pressure along the central axis of the vortex. Since the upstream boundary condition was inflow, the velocity profile there did not change with iterations. With a potential vortex at the upstream boundary and a more diffuse core just a few cells downstream, a strong pressure gradient was

created which was opposite to the direction of the axial flow in the vortex core. This adverse pressure gradient caused a deficit in the axial flow velocities in the core region and, in fact, the flow slowed to near stagnation in the cells just downstream of the upstream boundary.

To avoid the near-bursting condition caused by the potential vortex initial condition, a more "natural" circumferential velocity profile was used. This velocity distribution was obtained from the original potential vortex solution at a location 5 to 8 cells downstream of the point where the core grows to its equilibrium size. The shape of this profile was determined by the numerical viscosity, but it was very similar to Mager's analytic velocity profile (see Appendix A). Figure 9 compares radial distributions of circumferential velocity and circulation for Mager's profile and for a Rankine vortex with a typical profile from the Euler solution. Note that the Euler results are extremely close to the Mager profile.

The solutions obtained with this Mager-like upstream boundary condition are quite well behaved. Such flow quantities as core diameter, total circulation, and axial velocity are essentially constant down the length of the vortex. The only quantity which varies significantly in the axial direction is the distance of the vortex from the flat plate and the symmetry plane. The image vortex-induced velocity resulting from the proximity of the vortex to a solid wall causes the distance of the vortex from the plane of symmetry to increase with increasing downstream distance. The wall effect also causes the vortex to move slightly closer to the flat plate as it moves downstream. The magnitudes of the self-induced velocities in the Euler solution agree very well with what is predicted using the concept of image vortices. A very slight increase in minimum core pressure was noted as the vortex moved closer to the flat plate.

Figures 10, 11, 12, and 13 show crossflow plane streamlines, velocity vectors, vorticity contours, and pressure contours for a typical flowfield

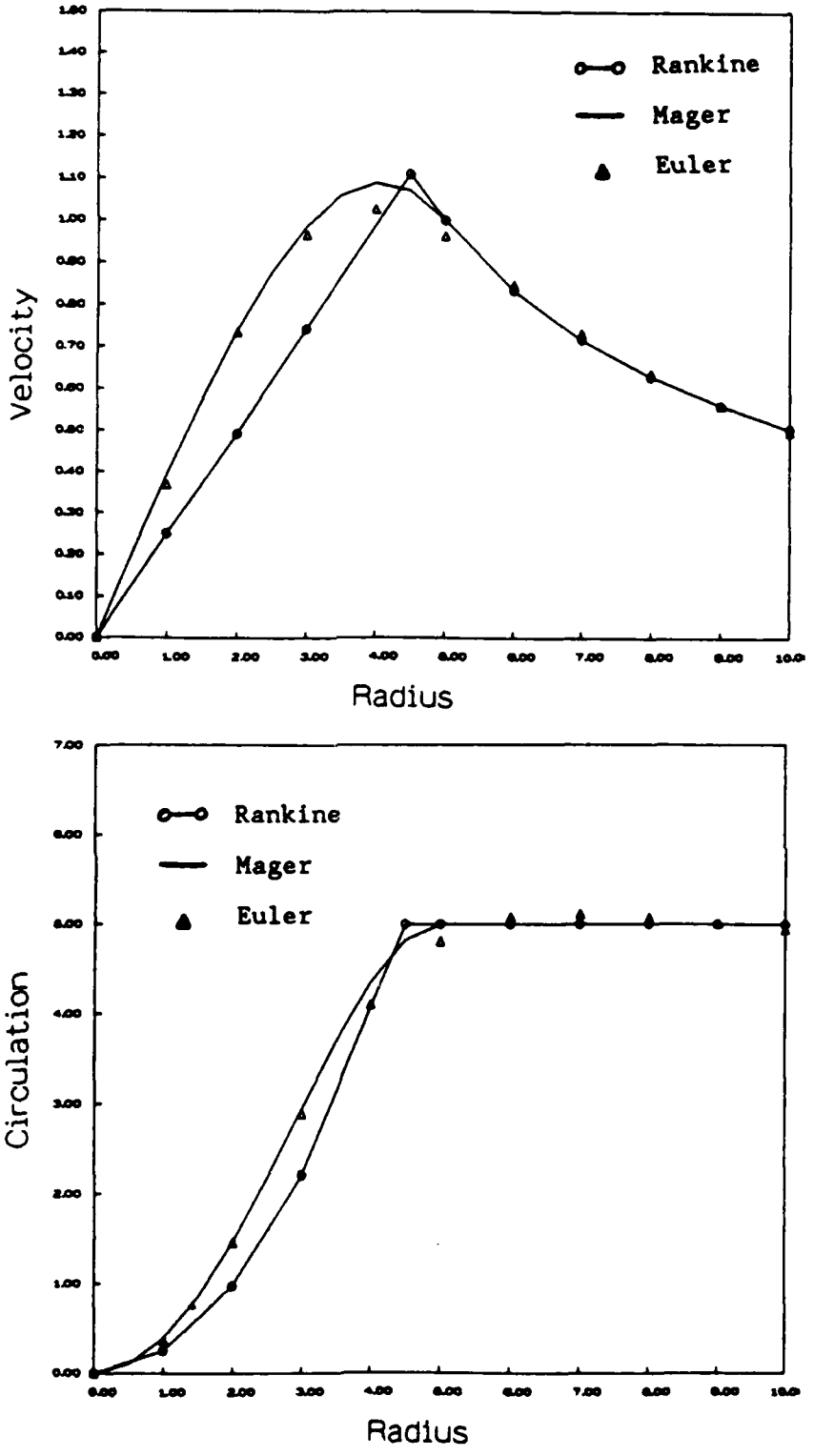

Figure 9. Radial variation of circumferential velocity and circulation.

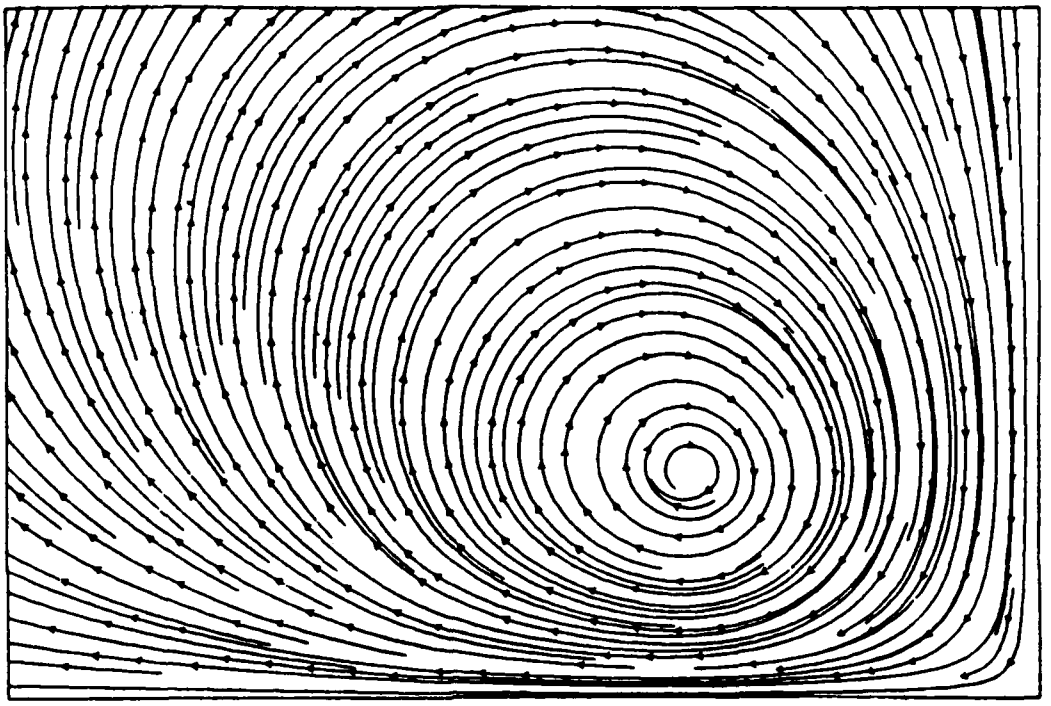

Figure 10. Rectangular grid study crossflow streamlines. Flat plate surface is at the bottom and plane of symmetry is at right.

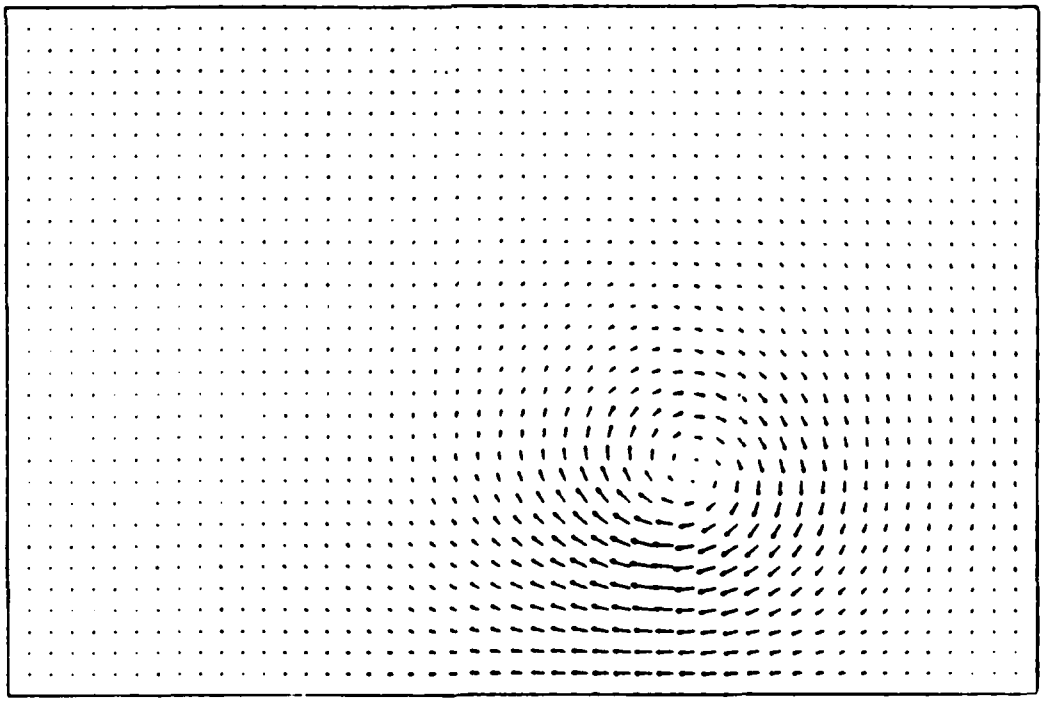

Figure 11. Rectangular grid study crossflow velocity vectors. Flat plate surface is at the bottom and plane of symmetry is at right.

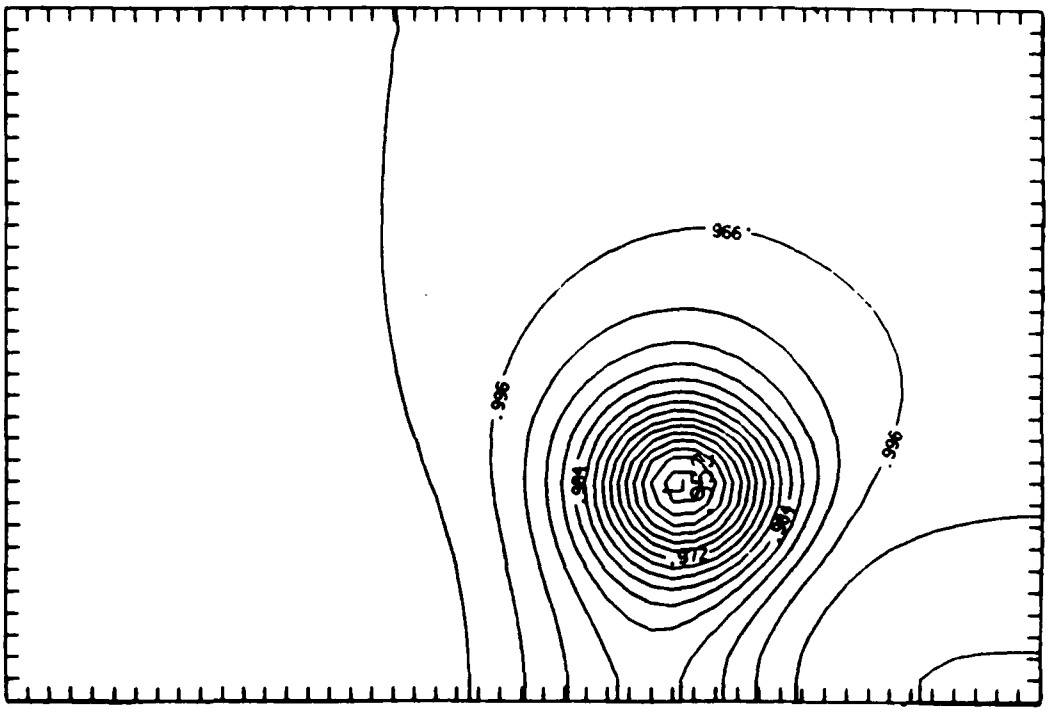

Figure 12. Rectangular grid study crossflow plane pressure contours. Flat plate surface is at the bottom and plane of symmetry is at right.

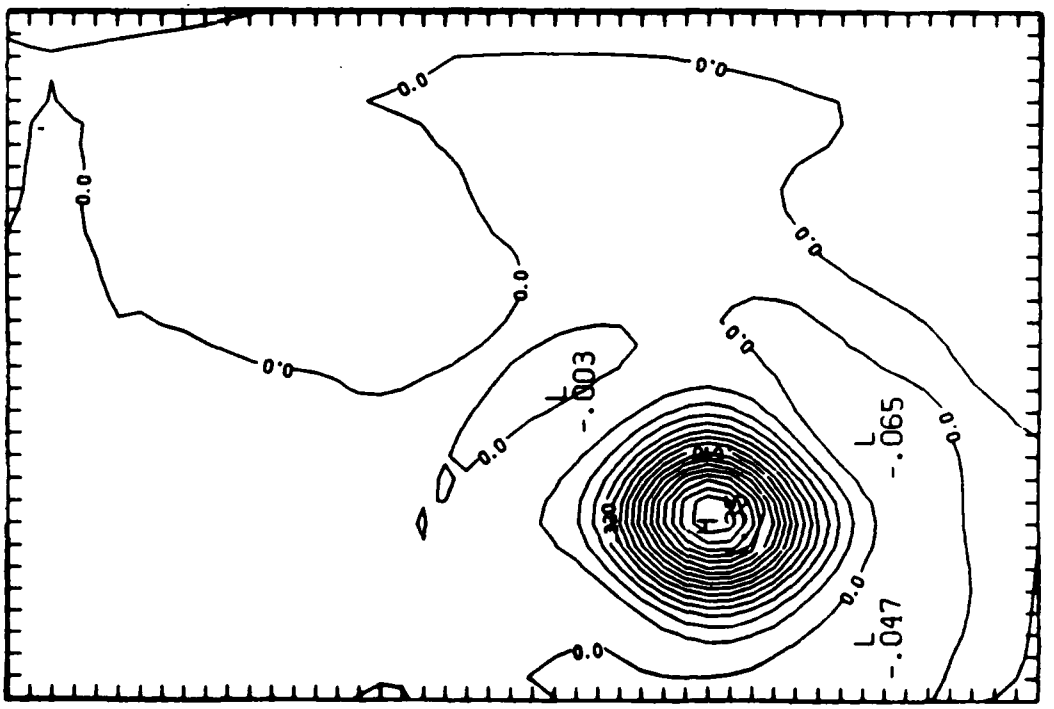

Figure 13. Rectangular grid study crossflow plane vorticity contours. Flat plate surface is at the bottom and plane of symmetry is at right.

at a point halfway down the length of the vortex. Tick marks on the frame of the two latter plots correspond to individual cells on the uniform rectangular grid. Note that the region of reduced static pressure spans approximately ten cells. The region of significant vorticity is also about ten cells in diameter. Outside this rotational core, however, the rest of the flowfield is very nearly irrotational. This result suggests that the use of irrotational image vortices in the vortex core model is acceptable. As a further evaluation of the use of irrotational image vortices in the core model, Figure 14 shows a crossflow streamline plot for a Mager profile with image vortex velocities added to it. The value of the stream function used for this plot is adjusted so that the streamline labeled 0 is the core edge. Note the very good agreement between this plot and Figure 10.

The relationship in the core model for the variation of core pressure with distance from walls can be evaluated by comparing it to pressure variations in the Euler solutions. Figure 15 plots vortex core pressure for two Euler solutions as a function of the wall proximity parameter C_ϕ. The solid line on the plot represents the pressure variation predicted using the vortex core model equation (11). Equation (11) appears to be a very good approximation for the effect of walls on core pressure.

Several tests were made to evaluate grid effects in the flow solutions. The first test was a study of the effect of the overall size of the grid on the flow solution. It was observed early in the research that if the grid was so small that the image vortex velocity caused the vortex to move into the cells adjacent to the lateral far field boundary, the boundary conditions used could not keep the vortex core intact. For a grid with 18 cells in the X direction, a Y-Z plane which was 32 cells high and 48 cells wide seemed to give good results, with the vortex never getting closer to the far field than Y = 11 and Z = 23. When this grid was reduced in size to 24 by 36, a 0.3% increase could be seen in the minimum pressures

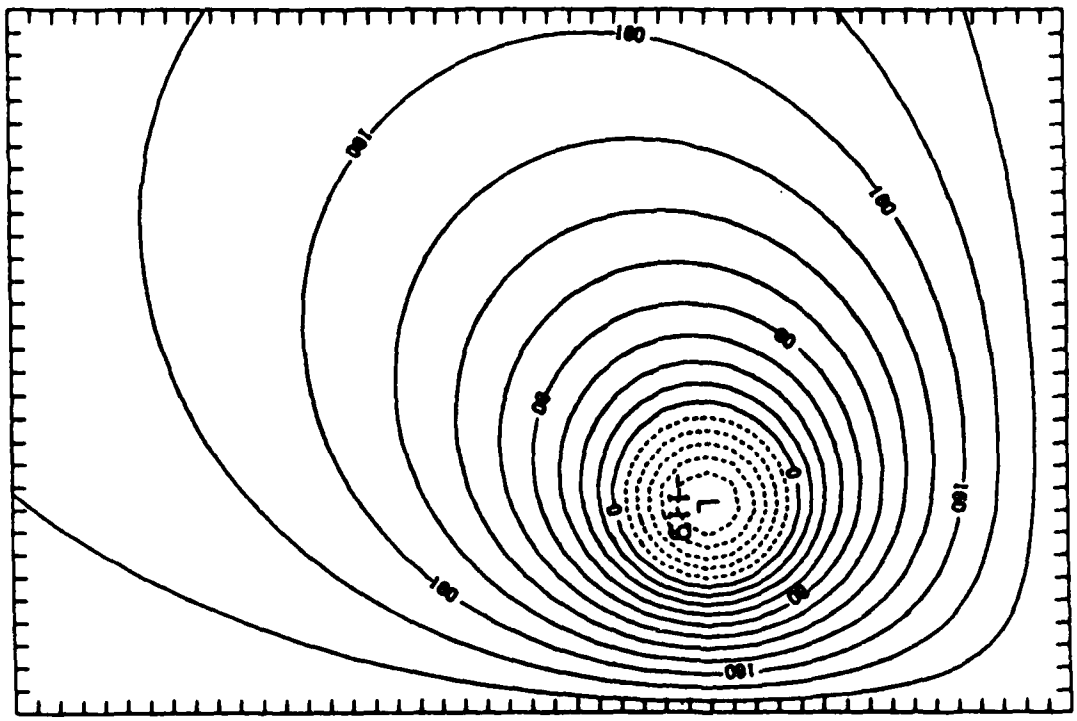

Figure 14. Crossflow streamlines for Mager profile plus image vortices.

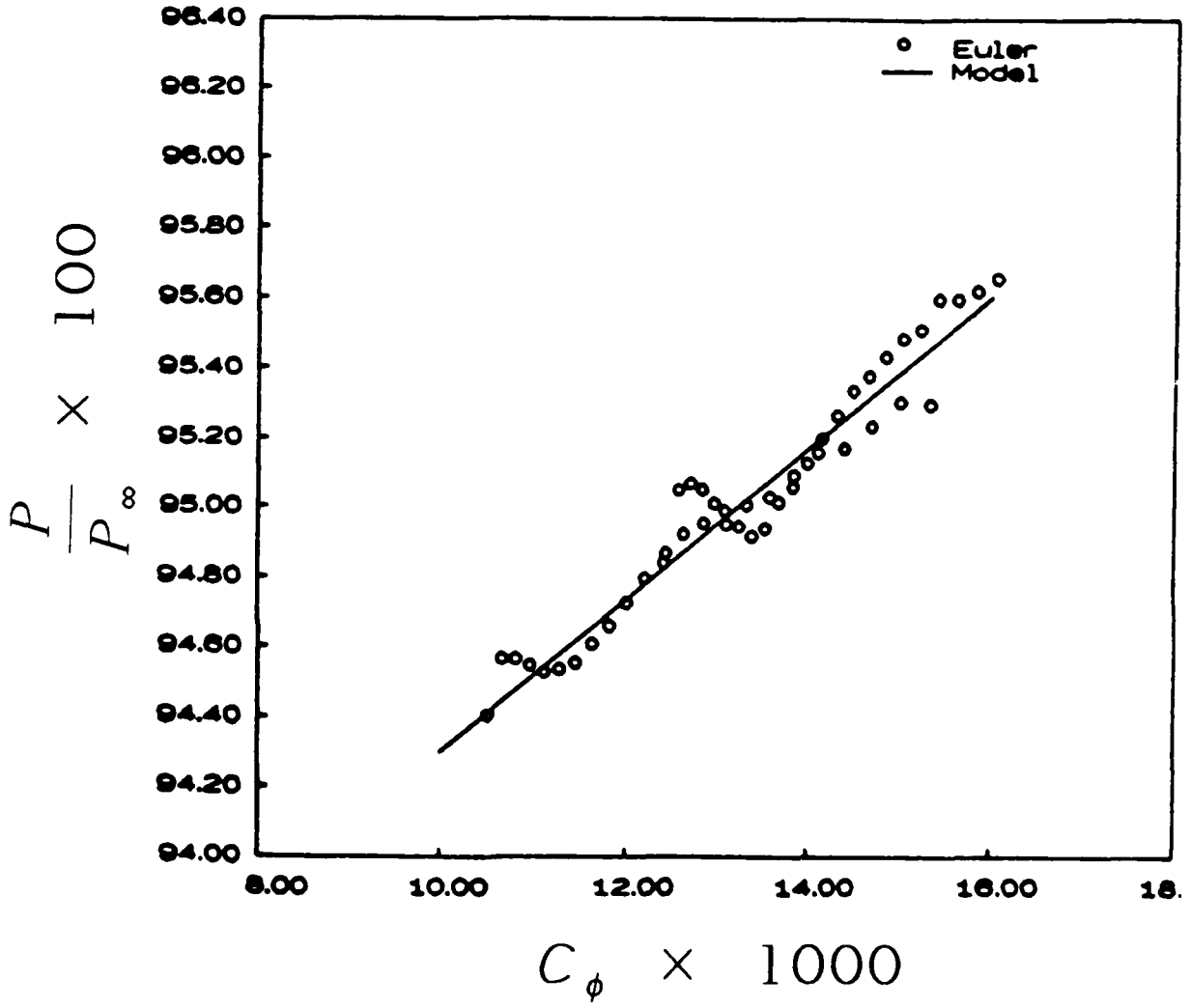

Figure 15. Variation of minimum core pressure with wall proximity factor, C_{ϕ}.

along the vortex core and the image vortex-induced velocity of the vortex core was 10% less. However, when the grid size was increased to 40 x 60, the difference in minimum core pressures was less than 0.1% and the lateral motion of the core showed no difference from that on the 32 x 48 grid. A study was also made of the effect of stretching the outer cells to place the far field boundaries even further away. For the 18 x 32 x 48 grid, stretching of the outer 6 cells in both the Y and Z directions had little effect on the solutions.

In order to evaluate the effects of cell aspect ratio on the quality of the flow solution, several test runs were made with the cells elongated or shortened by changing the grid spacing in the X or streamwise direction. In general, the effect of stretching or shortening the cells was negligible over a grid spacing from .5 to 2. in the X direction with the Y and Z grid spacing constant at 1.

The effect of grid skewing on the quality of the solution was also investigated. Since the image vortex velocities caused the vortex to move at an angle from the axial direction, the grid was skewed at this angle to keep the vortex in the cell with the same k index in each successive i plane. The cells in the region between the vortex and the plane of symmetry were stretched as necessary to keep the plane of symmetry parallel to the free stream flow direction. Figure 16 shows three views of one of these skewed grids, the grid labeled Grid A. The solutions obtained on this grid for the same number of iterations differed less than 0.04% from those obtained on the uniformly spaced grid, an almost indistinguishable difference. However, the calculation converged faster on the skewed grid, so the slight error which appears to exist between the two may be mostly a measure of convergence. This result suggests that a reasonable amount of grid skewness is tolerable in flow calculations around more complex geometries.

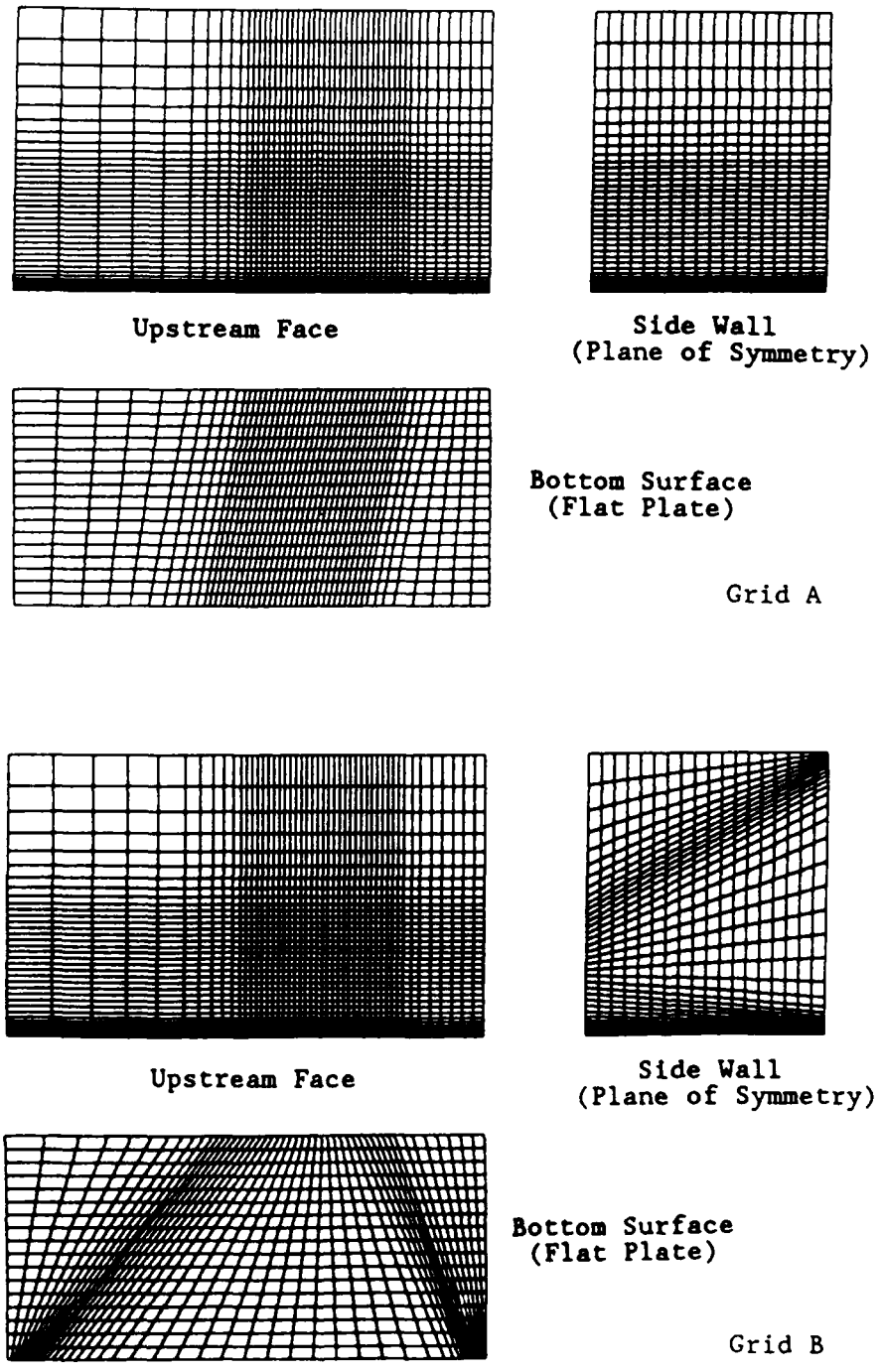

Figure 16. Skewed and stretched grids.

Grid A in Figure 16 has a much finer grid spacing in the region where the vortex core was placed, but it is stretched in the outer regions so the far field is kept at the same distance as it was on the uniform grid. As expected, a finer grid allowed a smaller vortex core since the core spread over the same number of cells as in the uniform grid case. In order to demonstrate the error this cell size effect could cause in a flow solution, a grid was generated which had a grid spacing of one half unit in the area of the vortex at the upstream end, but a spacing of 2 units at the downstream end of the domain. Three views of the grid are also shown in Figure 16 and labeled Grid B. The grid spacing in the streamwise or X direction was one unit throughout the domain, so the cells expanded from .5 x .5 to 2 x 2 in a distance of 18 units. This rate of grid expansion is much less than that of many grids commonly used for computations of flows around wings (see Rizzi [19] for example). However, when a vortex with a core of the minimum size resolvable by the Euler code on a given region of the grid was caused to flow into a part of the grid where the cell size was increasing, the vortex core also enlarged. Since the flow solver preserved the total swirl of the vortex, this non-physical growth of the core caused reduced circumferential velocities and increased pressures in proportion to the enlargement of the cells. Figure 17 compares side views of the two grids with velocity vector arrows drawn for their respective flow solutions. In the flowfield for Grid B, it is apparent that the adverse pressure gradient within the vortex core has created a reversal in the axial flow within the core similar to that which characterizes vortex bursting. The test case run with identical flow conditions and boundary conditions on Grid A shows only a slight reduction in axial flow velocities. Figure 18 plots the axial variation of pressure for the two solutions of Figure 17.

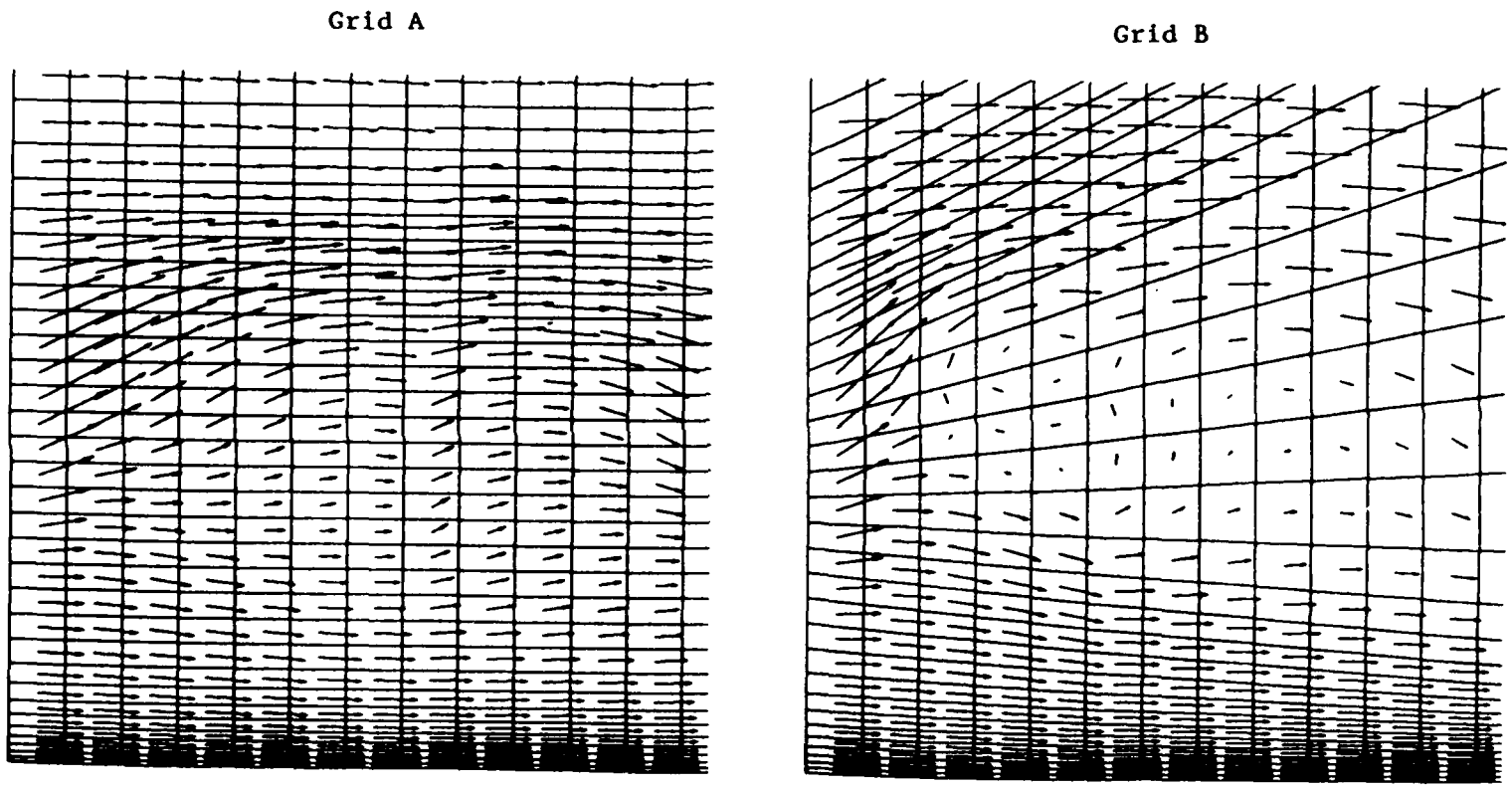

Figure 17. Side views of velocity vectors in the vertical plane containing the vortex axis for two flow solutions with identical initial and boundary conditions but different grids.

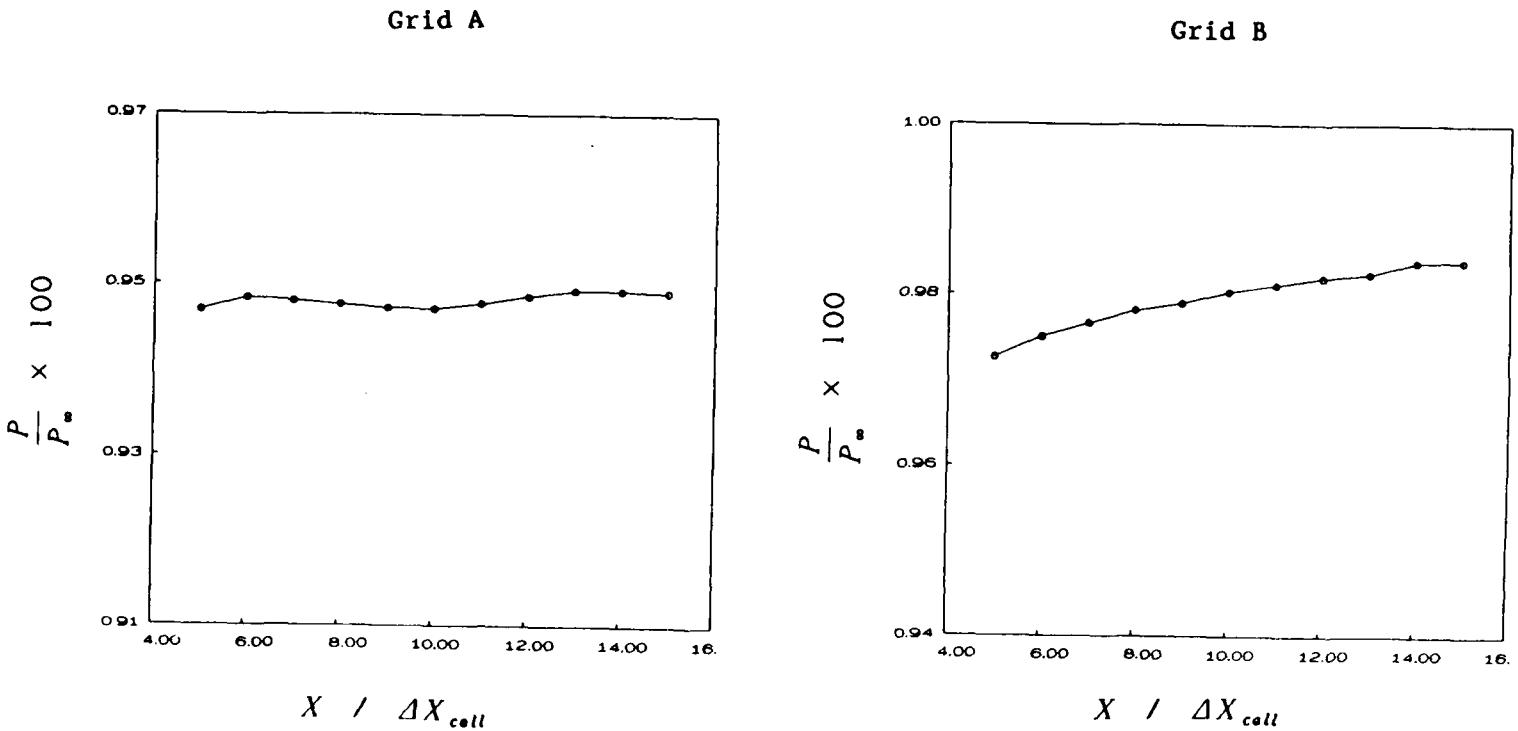

Figure 18. Axial variation of minimum core pressure for the two flow solutions of Figure 17.

Two general conclusions can be drawn from the results of these tests. First, the adverse effects of grid density and numerical viscosity on flow solutions containing vortices were shown to be potentially very serious, to the point of causing bursting. Second, many of the assumptions used in deriving the vortex core model were shown to be reasonable and compatible with the Euler formulation.

4.2 BURSTING CONTROL DEMONSTRATION

The vortex core model should be able to correct for or reduce the effects of grids and numerical viscosity in two ways. If axial velocity defects or bursting are caused by an expanding grid, the vortex core model should be able to correct for that effect when the physical vortex core is modeled with no rate of growth. On the other hand, if the grid is uniform and little or no axial velocity defect is present in the flow solution, then by modeling a physical core with a rapid rate of growth, the vortex core model should be able to produce bursting.

Both these capabilities were successfully demonstrated. Figure 19 shows side views of velocity vectors in the vertical plane containing the vortex for two different flow solutions on Grid A. The solution on the left was obtained using an Euler solver alone. The one on the right came from an Euler solver with the vortex core model. For this test, the physical core was modeled as growing very rapidly by giving the vortex growth parameter a large value. The vortex bursting produced by the model is apparent.

Figure 20 shows a demonstration of the model's ability to eliminate grid-induced vortex bursting on Grid B. The flow solution with grid-induced bursting on the left is for an Euler solver alone, while the

solution on the right is for the Euler solver with core model. For this test, the physical core size was arbitrarily set to the same constant value down the length of the vortex. Since no axial pressure gradient should develop if core area is constant, the model generated source terms which eliminated the grid-induced bursting.

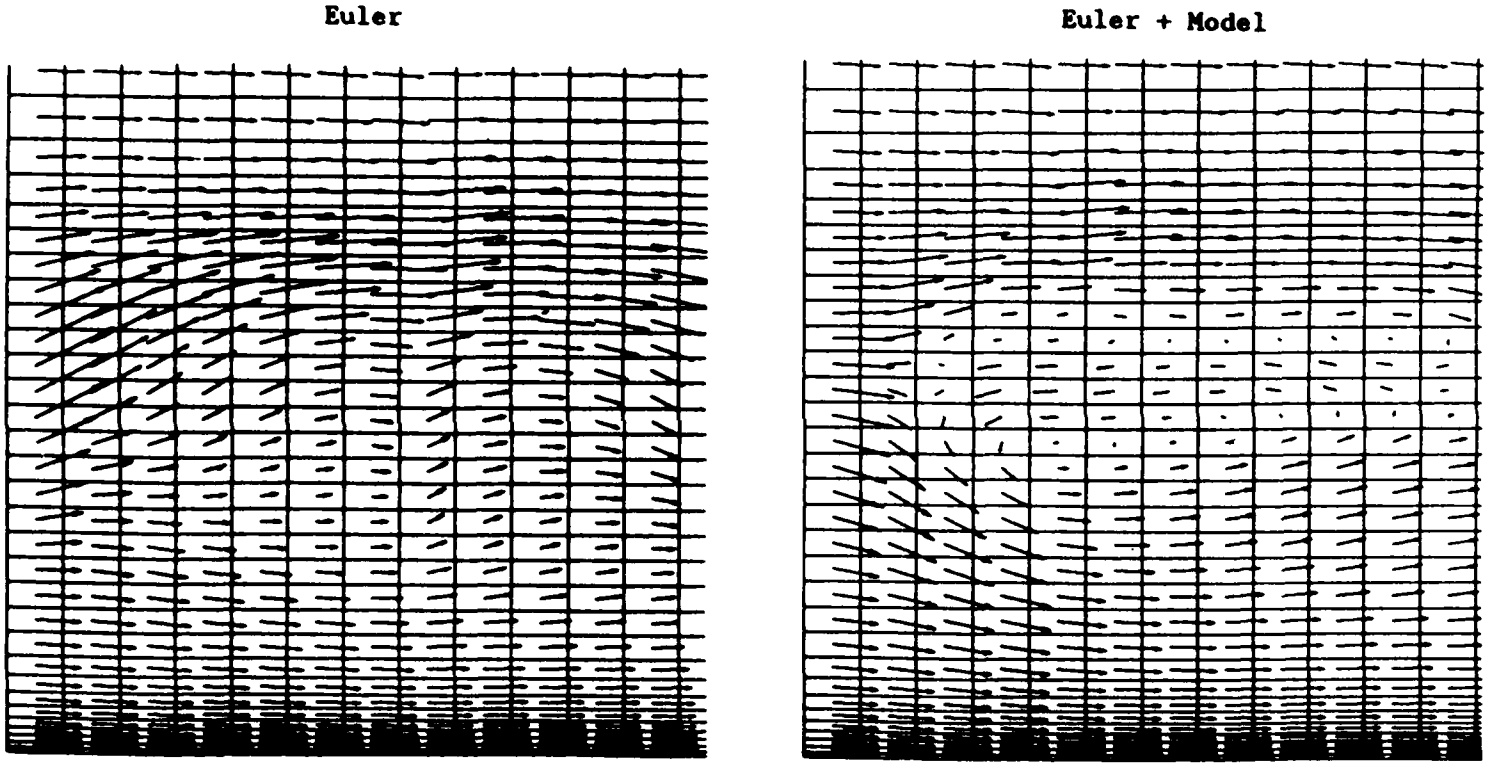

Figure 19. Side views of velocity vectors in the vertical plane containing the vortex axis for two flow solutions on Grid A. The solution on the left is from an Euler solver alone. That on the right is for an Euler solver plus vortex core model with a rapid growth of the model core specified.

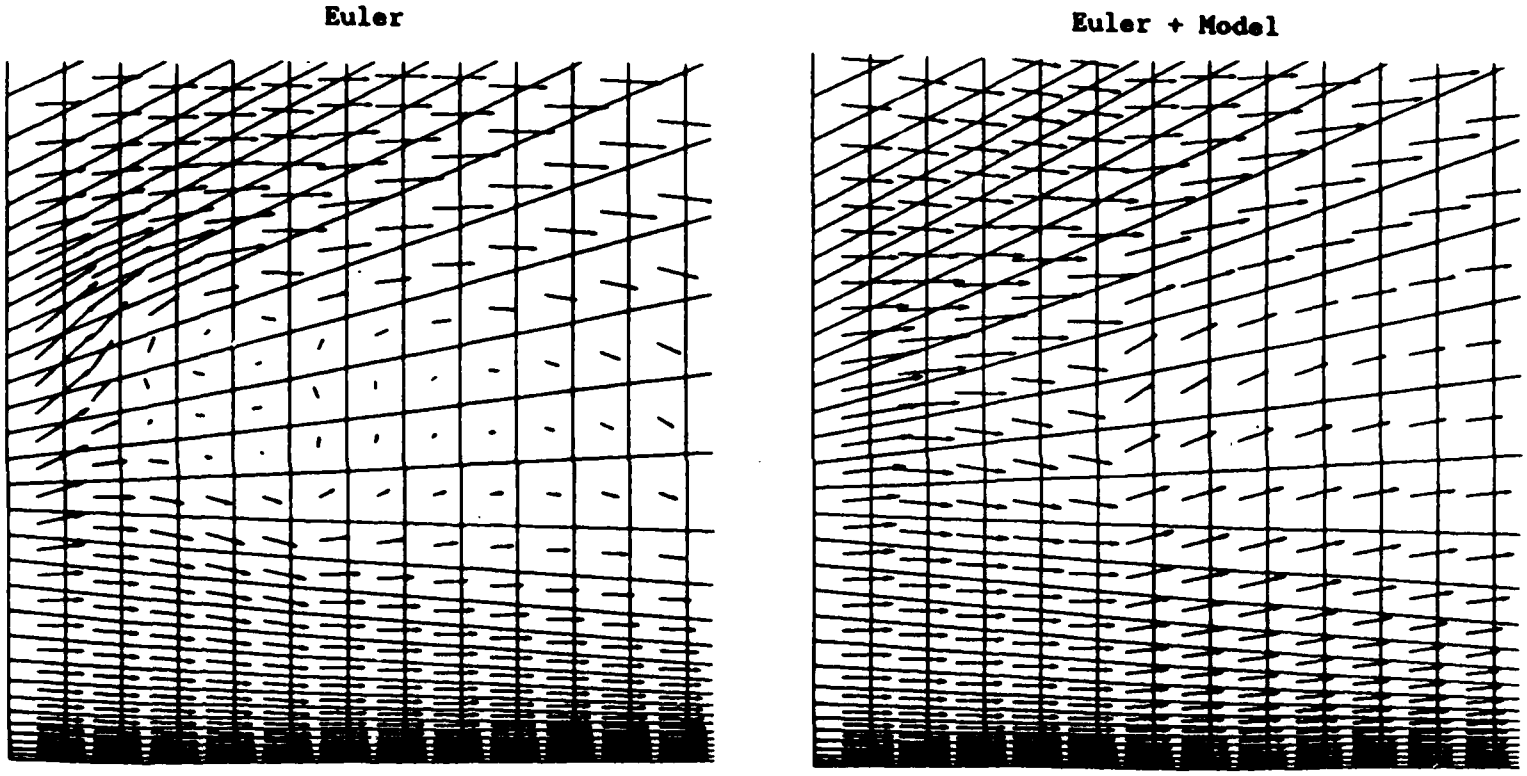

Figure 20. Side views of velocity vectors in the vertical plane containing the vortex axis for two flow solutions on Grid B. The solution on the left is from an Euler solver alone. That on the right is for an Euler solver plus vortex core model with constant model core size specified.

CHAPTER 5

RESULTS AND DISCUSSION

5.1 DELTA WING BURSTING STUDY

The vortex core model was tested to assess its ability to predict the onset of bursting on four different delta wings. Grids with H-O topology were used around flat plate delta wings with sweep angles varying from 55 to 76 degrees. All grids used were 57 x 21 x 33 with 25 x 33 points on the wing surface. Figure 21 shows planform views of the right half of each wing used for the test. Mach number for all these tests was 0.2.

The first wing tested was swept 65 degrees. Flow solutions were first obtained for this wing using the Euler solver alone. It was discovered that at angles of attack above 25 degrees, some bursting was present in the Euler solutions. This was not surprising, since cell sizes in the grid increased in the streamwise direction, forcing the vortex core in the Euler solution to grow. The locations of the bursting points did not, however agree with available wind tunnel data [4] for this wing. This suggests

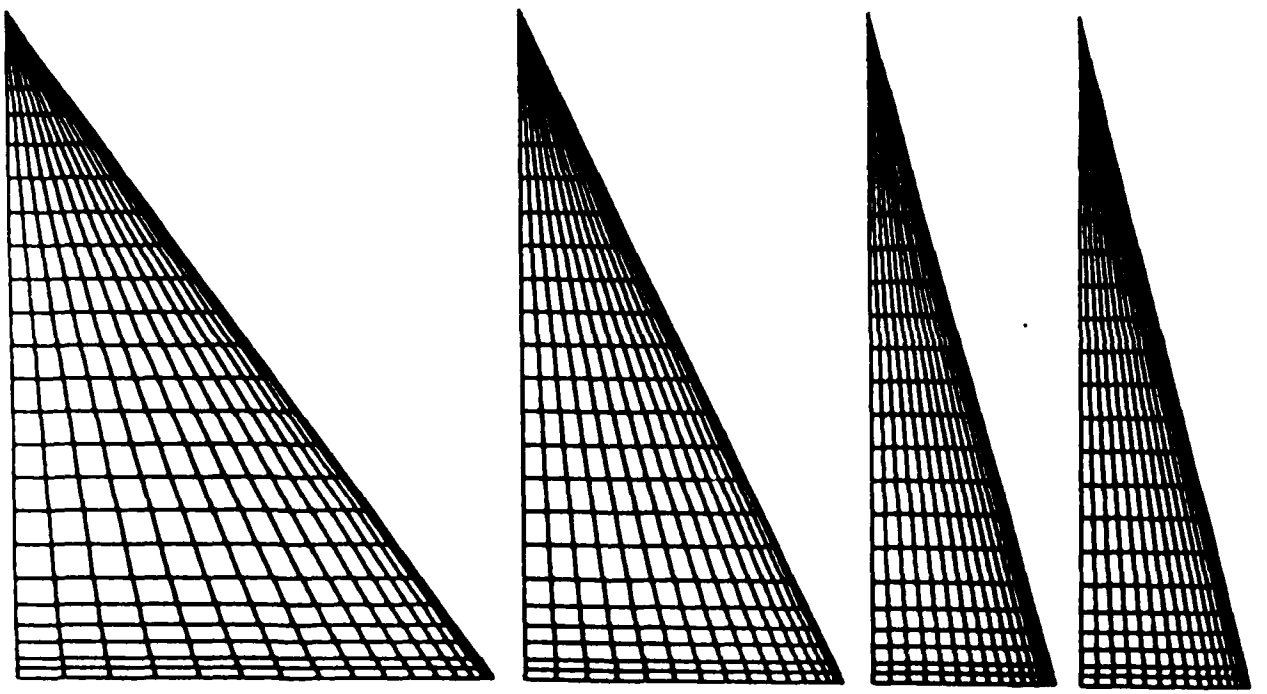

Figure 21. Planform views of the right halves of four delta wings used in the vortex bursting study.

that the rate of core growth induced by the grid was not the same as that of the physical vortex in the wind tunnel tests.

For the core model tests, a value for K_g was chosen which gave the same core area at the wing trailing edge as that in the Euler solution. For this situation, the difference between the Euler core and the model core was limited to differences in the core growth profile, but not in the final core size. Appropriate values of K_a and K_i were determined by trial and error. The values calculated for the Rankine vortex and Mager's profiles were used as initial guesses, but these proved to be too large. When these large values were used, the solution was destabilized and caused to diverge rapidly. As smaller values of K_a and K_i were tried, a range was found where they were not so small that they did not produce an effect, but not so large that they caused instability. Well within the bounds of this range, values were found which allowed the model to generate source terms which brought the bursting locations in the resulting solution into very close agreement with the wind tunnel data. Figure 22 shows a comparison between bursting locations for the Euler alone solutions and the results from the Euler code with core model. Wind tunnel data for the same wing are also plotted. As can be seen, the agreement between the wind tunnel data and the model results is very good over the entire range of angles of attack, except at the very highest angles. Here the Euler solver with model could never quite get bursting to progress all the way to the apex. This trend is visible in the Euler alone solution as well, and was common in all the other delta wing bursting tests made.

At the lower angles of attack, the method experienced some instability. This was overcome by increasing the number of iterations of the Euler solver between updates of the core model momentum source terms. The source terms were applied at each iteration, but their values were

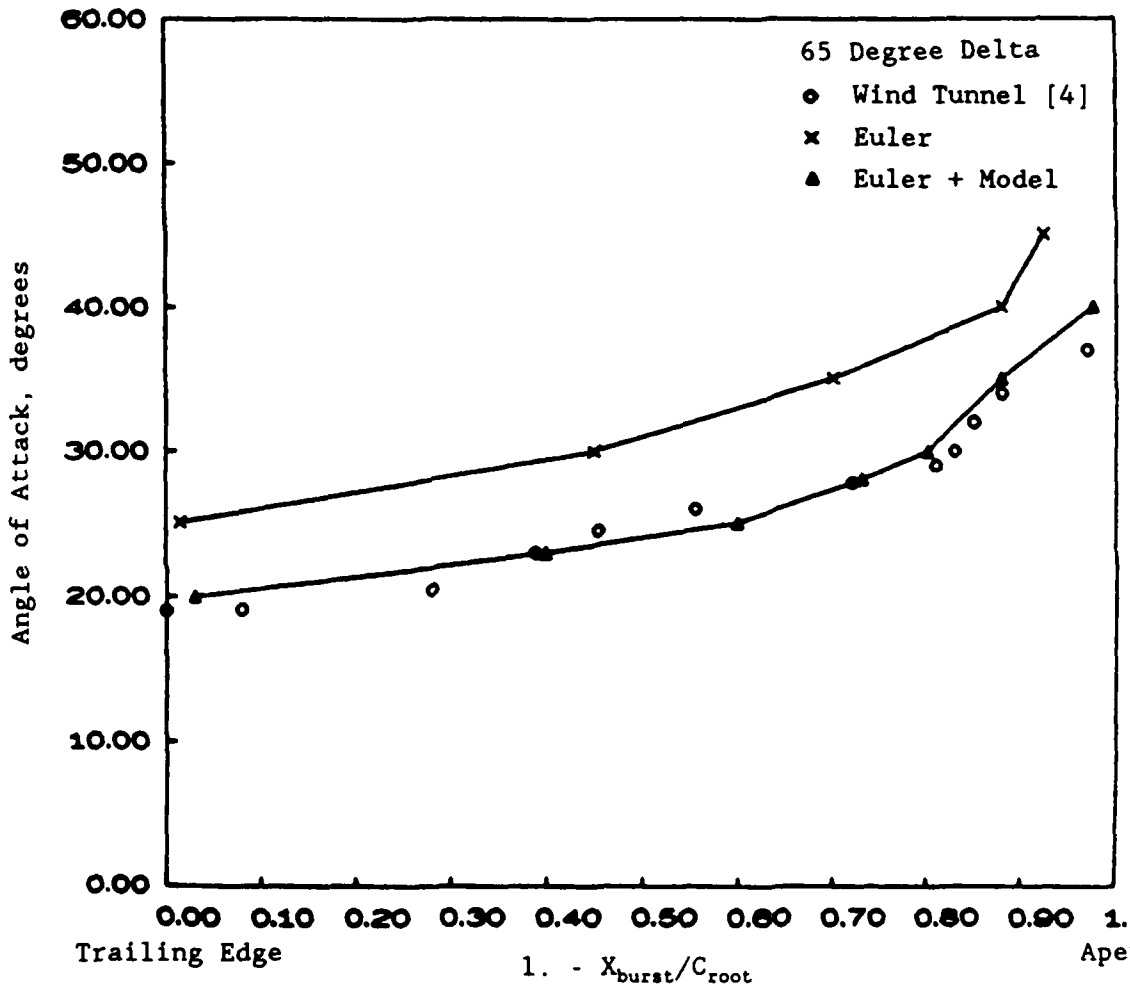

Figure 22. Variation of bursting location with angle of attack for 65 degree delta wing.

updated only periodically. For angles of attack above 25 degrees, source terms were updated every 50 iterations of the Euler solver. For 20 and 23 degrees angle of attack, updates were done only once every 150 iterations. In both cases, as the flow solutions progressed, the magnitude of the source terms decreased with each update. In the final converged solutions, the momentum sources were usually about 10% or less of their initial values.

The next test of the core model was to determine if the same values for K_g, K_a, and K_i would produce equally good results on delta wings with much different planforms. A 75 degree delta wing was first tested. Figure 23 shows bursting location curves for this wing for Euler, Euler with core model, and wind tunnel results. Agreement with the wind tunnel data of Wentz [4] is better than Euler alone results, but not as good as for the 65 degree delta wing. When the wind tunnel data of Payne and Nelson for this wing is plotted, however, the agreement is improved.

Tests were also made on a 55 degree delta. Figure 24 plots these results. Once again, the agreement between Euler with model results and wind tunnel data is better than for the Euler alone solutions, though not as good as for the 65 degree wing.

In order to compare results from the core model with a Navier-Stokes solution, a fourth delta wing was tested. This wing had an aspect ratio of 1 and a sweep angle of approximately 76 degrees. Figure 25 compares the resulting bursting location versus angle of attack curves with the single Navier-Stokes result [39]. Of significance in evaluating the usefulness of the present method is the fact that all of the Euler and Euler with model solutions obtained for this test required less total computation time than the single Navier-Stokes result.

Figure 26 shows spanwise surface pressure coefficient distributions at the midpoint of the root chord of the aspect ratio 1 delta wing at 20.5

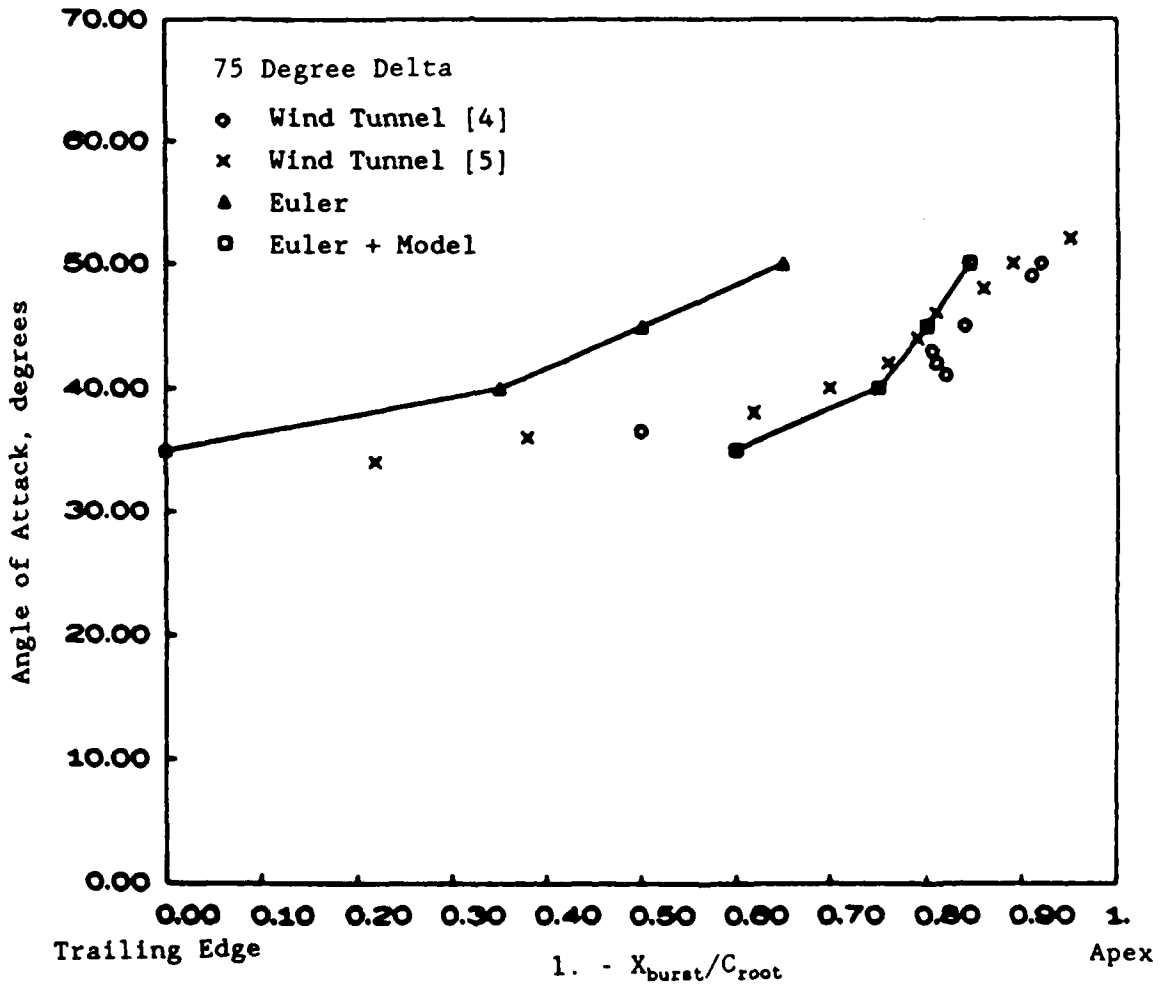

Figure 23. Variation of bursting location with angle of attack for 75 degree delta wing.

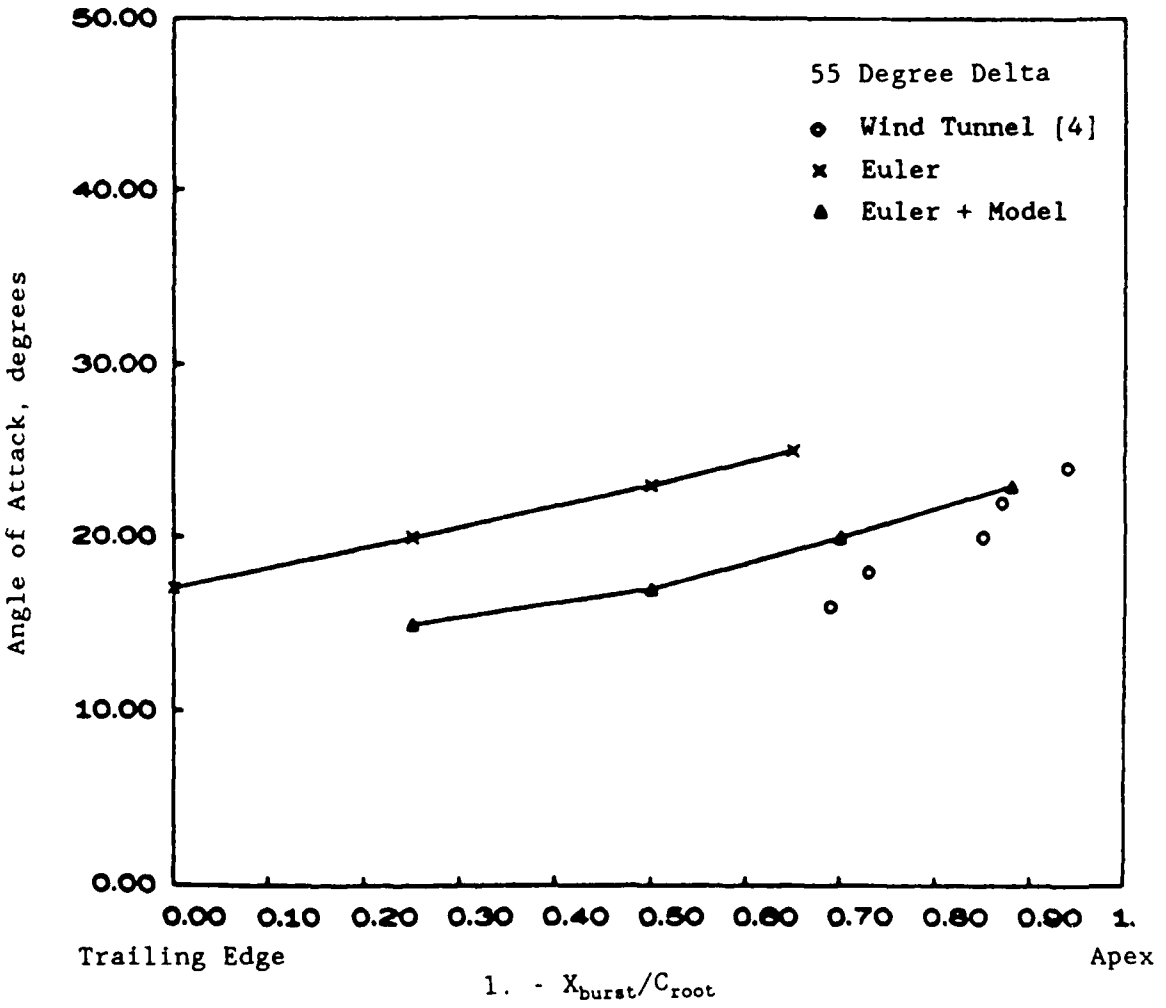

Figure 24. Variation of bursting location with angle of attack for 55 degree delta wing.

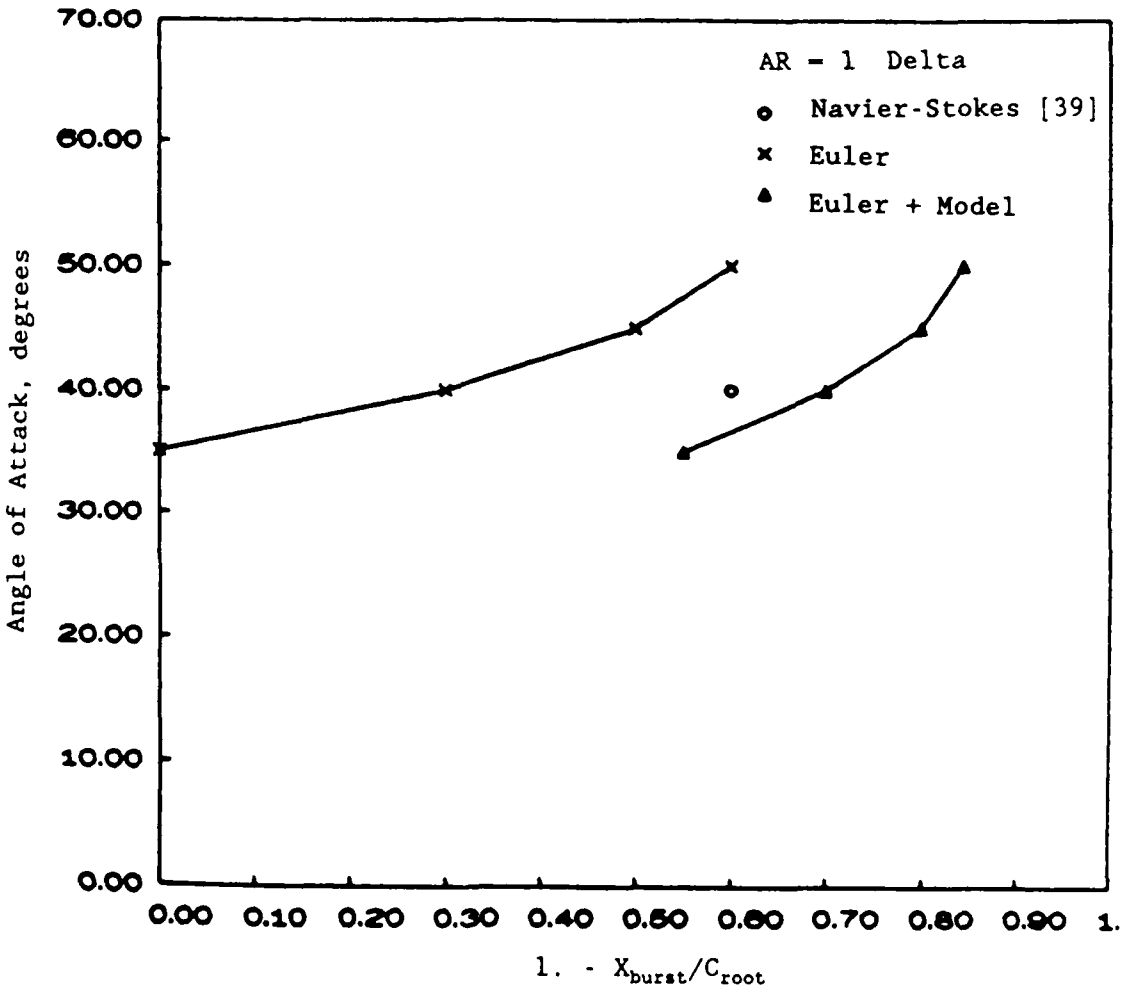

Figure 25. Variation of bursting location with angle of attack for a delta wing with an aspect ratio of one.

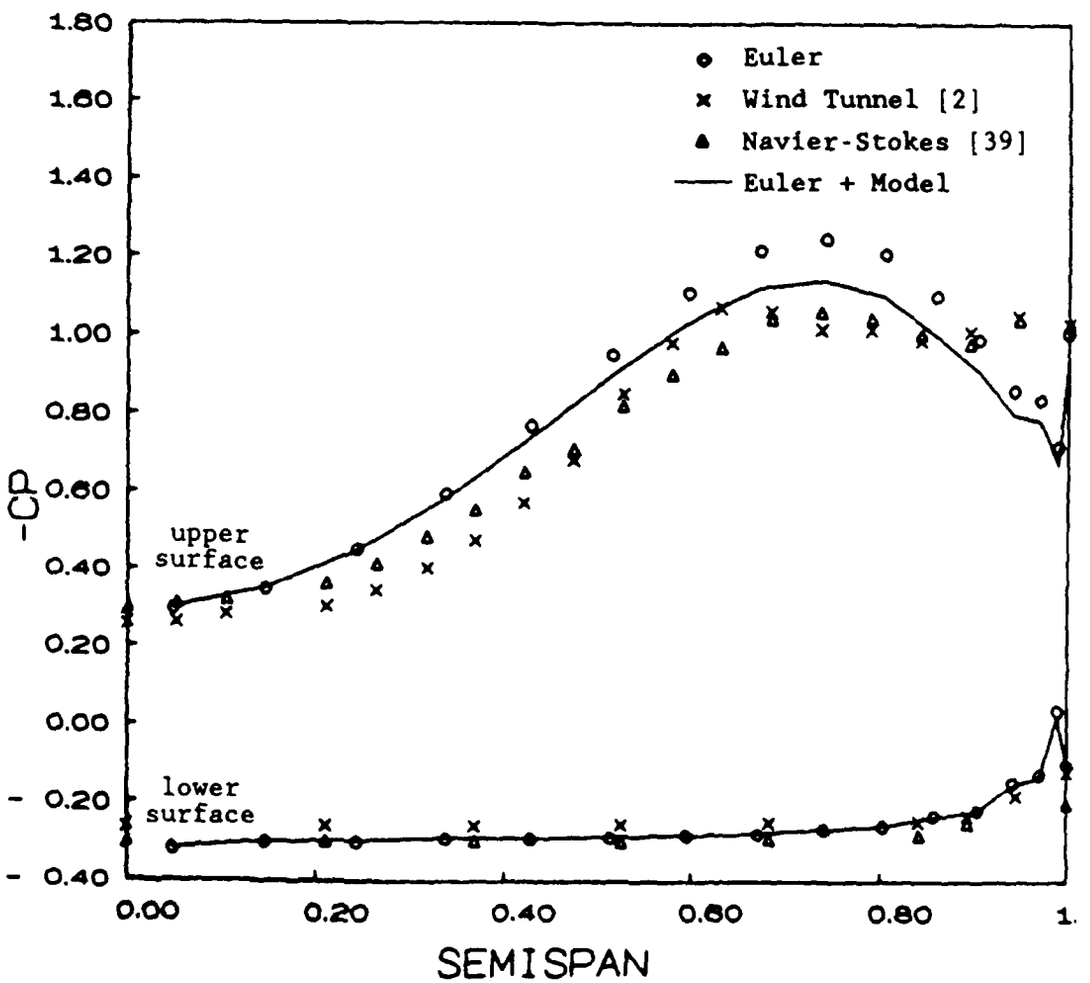

Figure 26. Spanwise pressure coefficient distributions at X/C = 0.5 for an AR = 1 delta wing at 20.5 degrees angle of attack.

degrees angle of attack. At this angle of attack, the vortex does not burst over any part of the wing. The C_p curve predicted by the Euler solver with the core model is compared with curves from the Euler solver alone and from Navier-Stokes simulations [39] and wind tunnel tests [2]. Note that neither of the Euler solvers captured the secondary vortex influence on the C_p curve which is evident in the wind tunnel data and Navier-Stokes solutions. However, the vortex core model does allow the modified Euler code to predict the peak of the C_p curve in closer agreement with experiment. Although bursting does not occur in this flow solution, the core model still has an effect on the axial velocities in the core. As axial velocities are decreased, the core expands slightly, reducing circumferential velocities and increasing core pressure. Figure 27 compares velocity vectors in a nearly horizontal plane which is parallel to the Z axis and contains the vortex axis for the same wing at 40 degrees angle of attack. The result from the Euler code alone shows the bursting point at an axial station about 70% of the root chord downstream of the wing apex. The Euler code with core model gives the bursting point at about 30% root chord, which does agree better with Navier-Stokes results [39]. Figure 28 compares the corresponding C_p curves for the two solutions at 50% root chord. The vortex at that station has burst in the Euler with model solution, but not in the Euler alone solution. Note the flattening of the C_p curve when bursting has occurred.

5.2 BOUNDARY CONDITION COMPARISONS

The shear layer model surface boundary condition was tested on the arrow wing shown in Figure 6. As a basis for comparison, test runs were first made using FLO57 with two choices of surface boundary conditions.

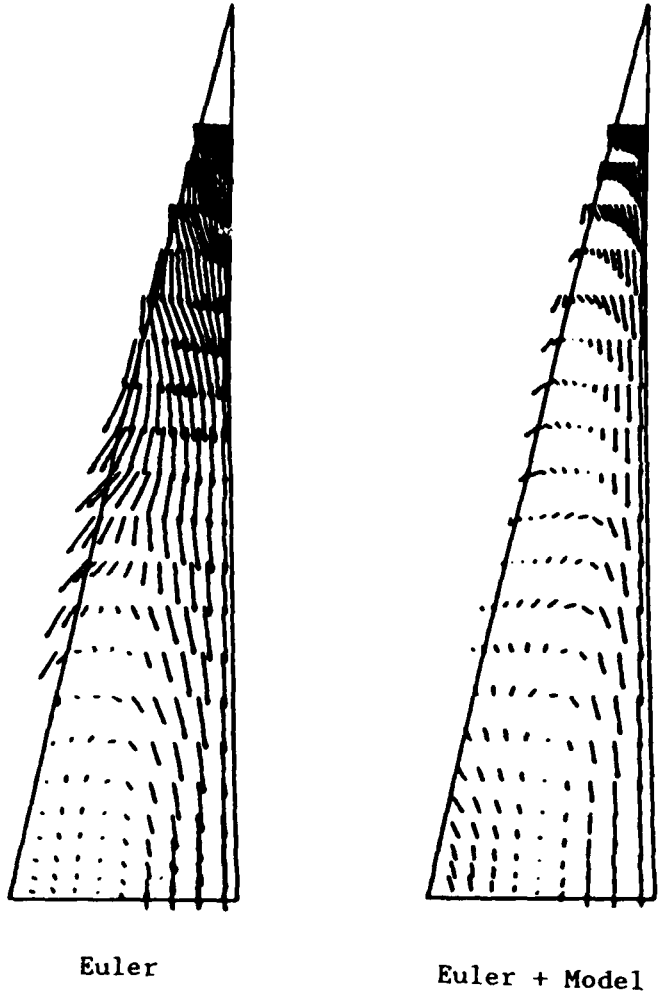

Figure 27. Planform views of velocity vectors in the horizontal plane of the leading edge vortex over an AR = 1 delta wing at 40 degrees angle of attack.

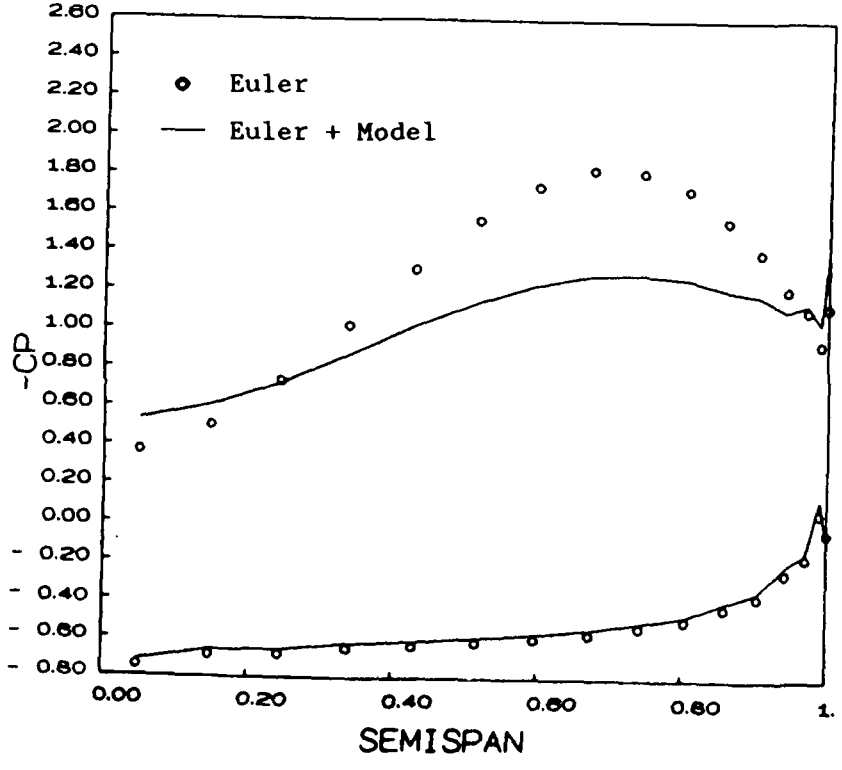

Figure 28. Spanwise pressure coefficient distributions at X/C = 0.5 for an AR = 1 delta wing at 40 degrees angle of attack.

The first of these extrapolates surface pressure from the boundary cell center using the momentum equation normal to the wing surface. The second simply equates pressure at the surface to pressure at the cell center. Surface pressure plots for a range of angles of attack for the two boundary conditions are compared with wind tunnel data [40] in Figure 29. The tendency for the momentum boundary condition to delay leading edge separation is apparent. Likewise, the vortex appears to develop too quickly when using the simple boundary condition which equates surface pressure to boundary cell pressure. Figure 30 shows results using the new boundary condition with the shear layer model at four degrees angle of attack for a range of values of the effective shear layer thickness parameter, K_t. Wind tunnel results are shown for comparison. Reynolds number is 6 million for both the computer model and the wind tunnel tests. A value of 2.1 for Kt appears to give the best results.

Figure 31 compares surface pressure plots from wind tunnel tests with those for the shear layer model surface boundary condition for a range of angles of attack. K_t was held constant at 2.1 for this simulation. Note that the new boundary condition results match the wind tunnel data better than results for either of the old boundary conditions, especially for angles of attack of eight degrees and less. At 10 degrees, a difference can be seen between the location of the Euler with model vortex and the wind tunnel vortex. This difference may be due to the crude approximation of the viscous effects in the shear layer used in developing the present model.

For the preceding tests, the shear stress parameter, K_s was left equal to zero. For another set of tests, K_s was set equal to 0.074 and used in the Euler solver with the shear layer model on two different cropped delta wings at relatively large angles of attack. Both wings had sweep angles of 65 degrees and taper ratios of 0.15. The first wing used a NACA 0012

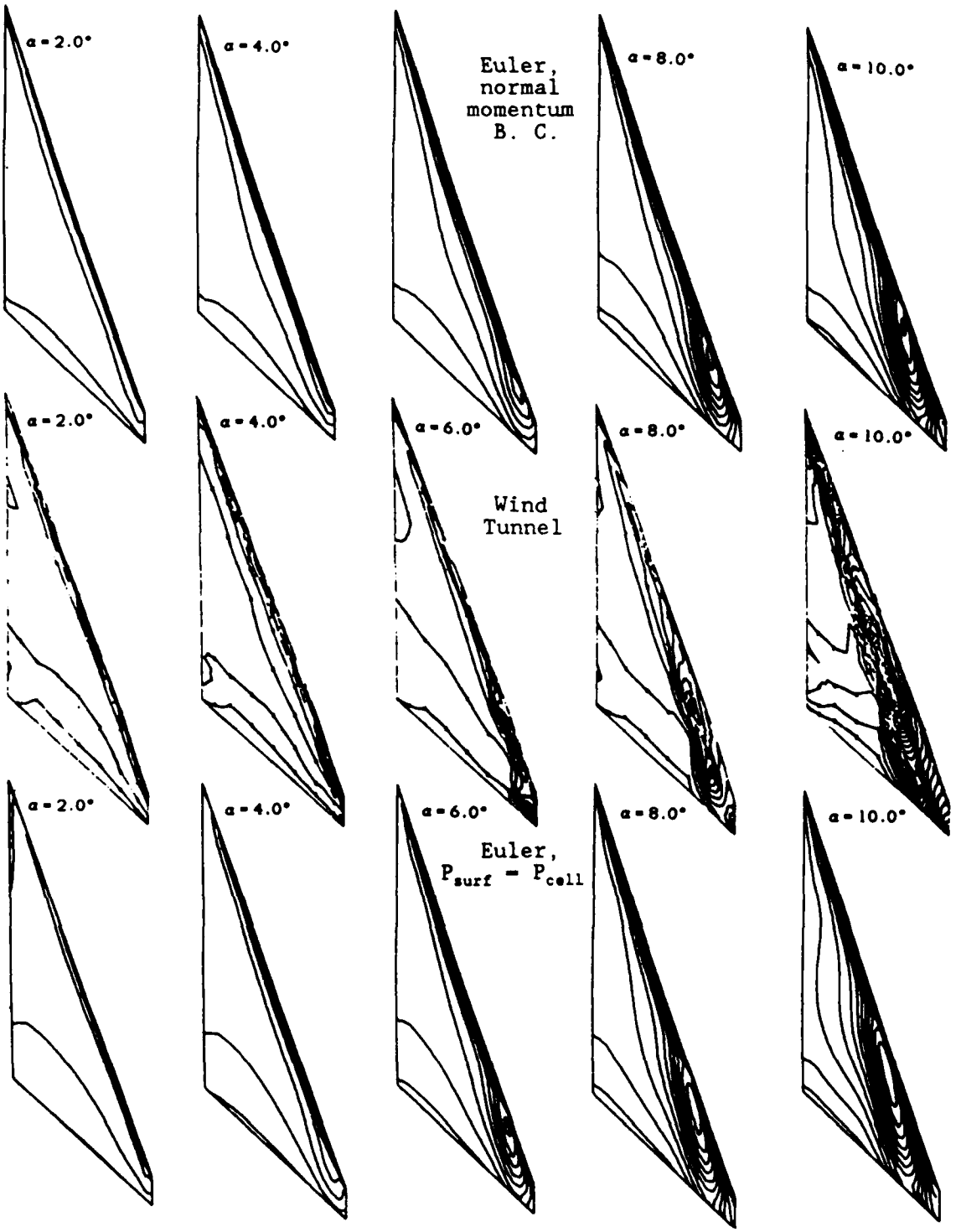

Figure 29. Comparison of surface pressure contours on an arrow wing for wind tunnel tests [40] and two Euler solutions with different surface boundary conditions.

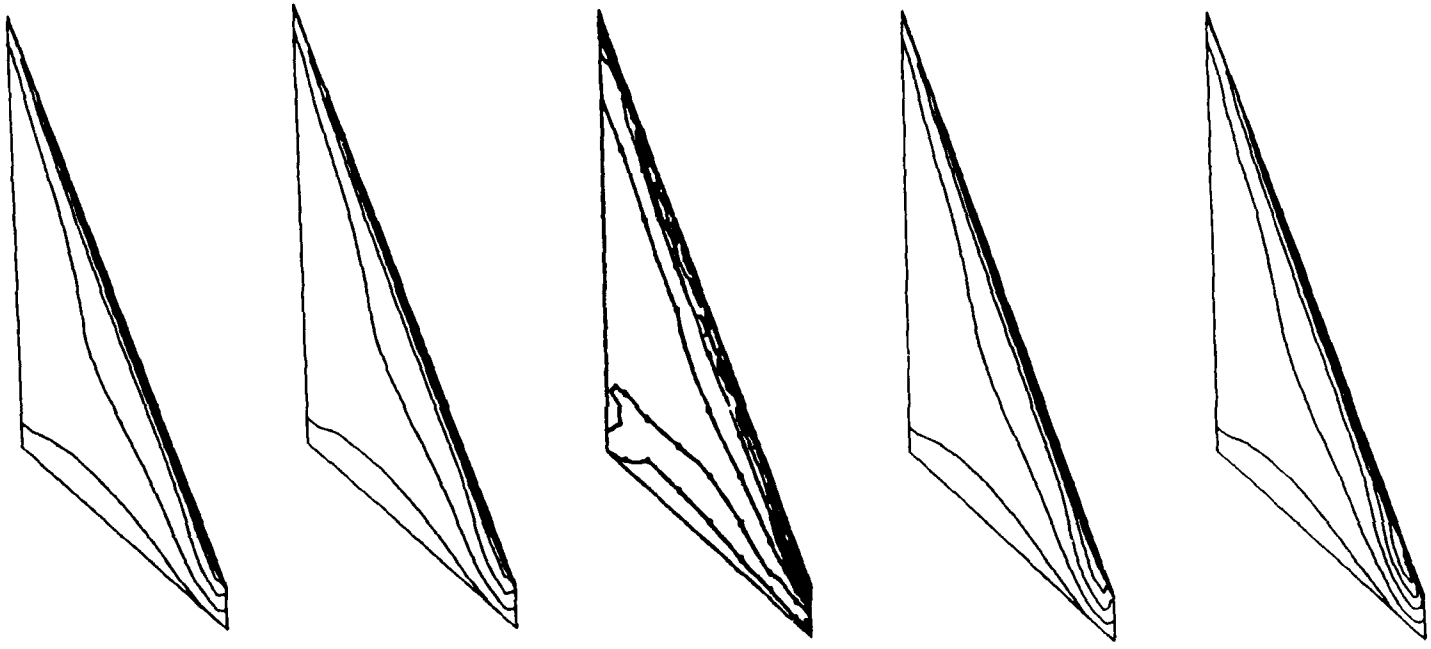

Figure 30. Wing surface pressure contours for a range of values of the shear layer effective thickness parameter compared with wind tunnel data. Angle of attack is ½ degrees.

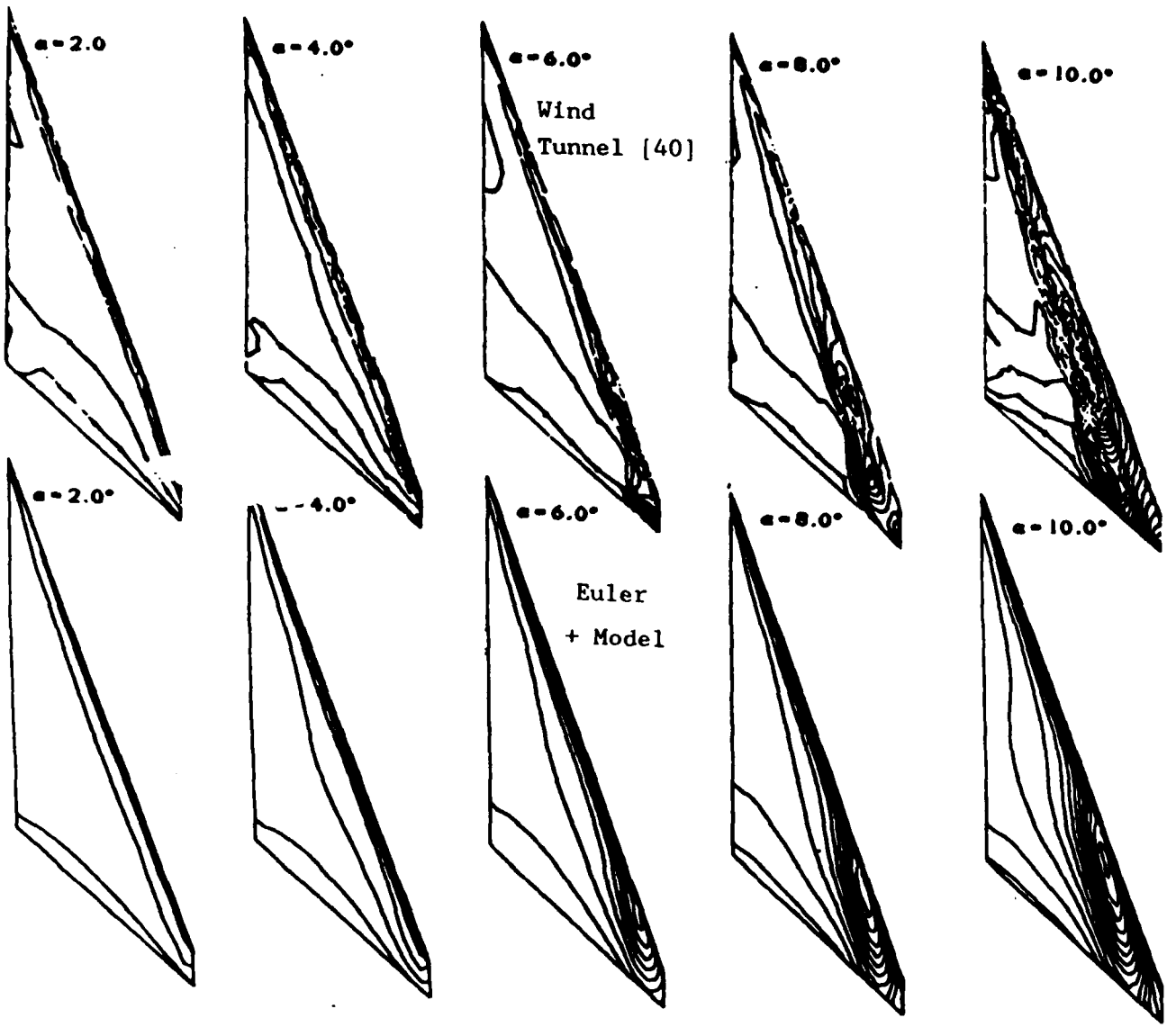

Figure 31. Arrow wing surface pressures for a range of angles of attack compared with wind tunnel data. [40] K_t is 2.1 and K_s is 0.

airfoil. When a flow solution was obtained for this wing at 30 degrees angle of attack, a secondary vortex was seen in the flowfield between the primary vortex and the leading edge. Figure 32 shows crossflow velocity vectors at X/C_{root} = 0.5 for this result compared with results from an Euler solver alone for the same wing and flow conditions. The secondary vortex is made especially visible by the contrast with the Euler alone solution.

In the second test, a delta wing with the same planform but a NACA 65A005 airfoil was tested at 20 degrees angle of attack. Ks was again set to 0.074. Figure 33 shows surface pressure contours for this result compared Euler alone results for the same wing and flow conditions. Note that the secondary vortex causes the primary vortex to move inboard and that a small local trough of pressure coefficient develops under the secondary vortex. Figure 34 shows crossflow velocity vectors for these conditions. The secondary vortex is just barely visible as only a single row of three arrows a little inboard of the leading edge. Figure 35 shows velocity vectors on the surface of the wing for the Euler alone solution and the Euler with model results. The secondary separation line is visible, as is the area of inboard flow under the secondary vortex.

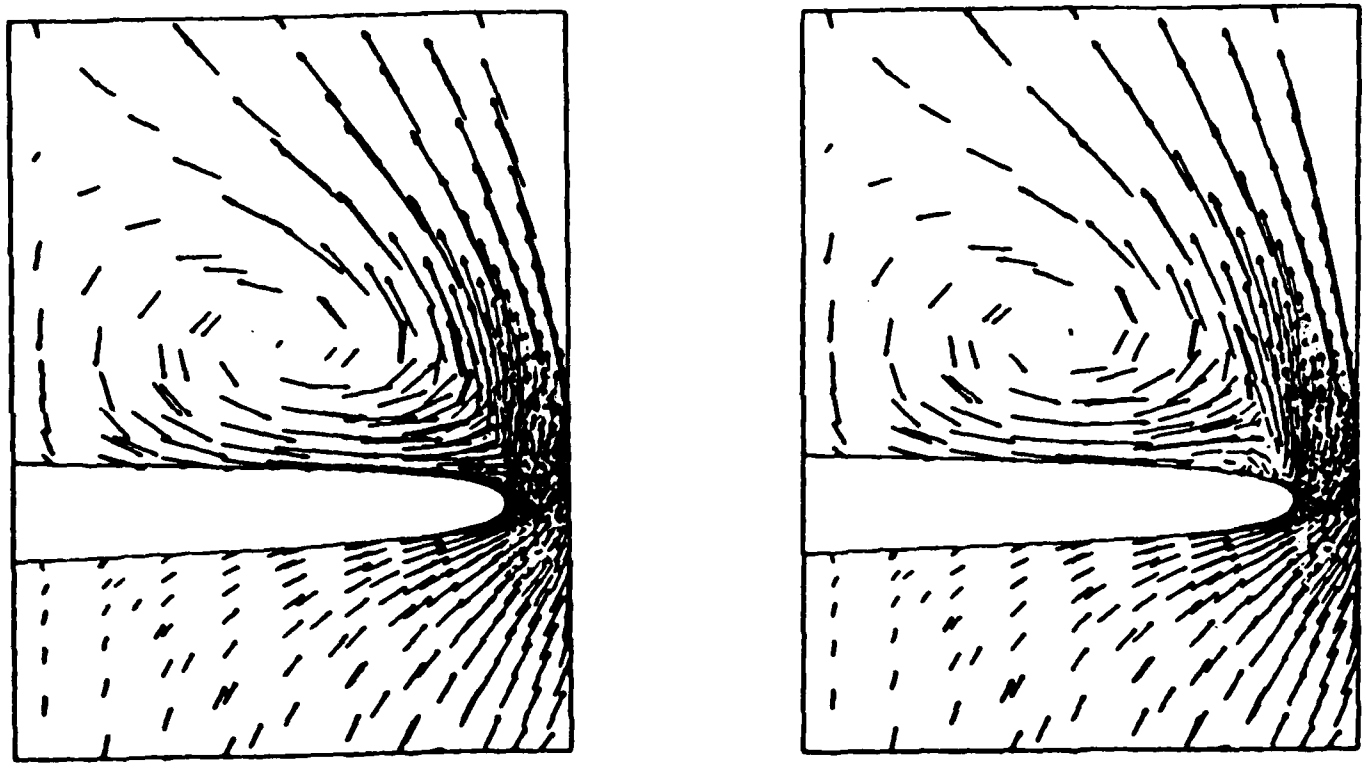

Euler

Euler + Model

Figure 32. Crossflow velocity vectors at X/C_{root} = 0.5 for a 65 degree delta wing with a NACA 0012 airfoil at 40 degrees angle of attack.

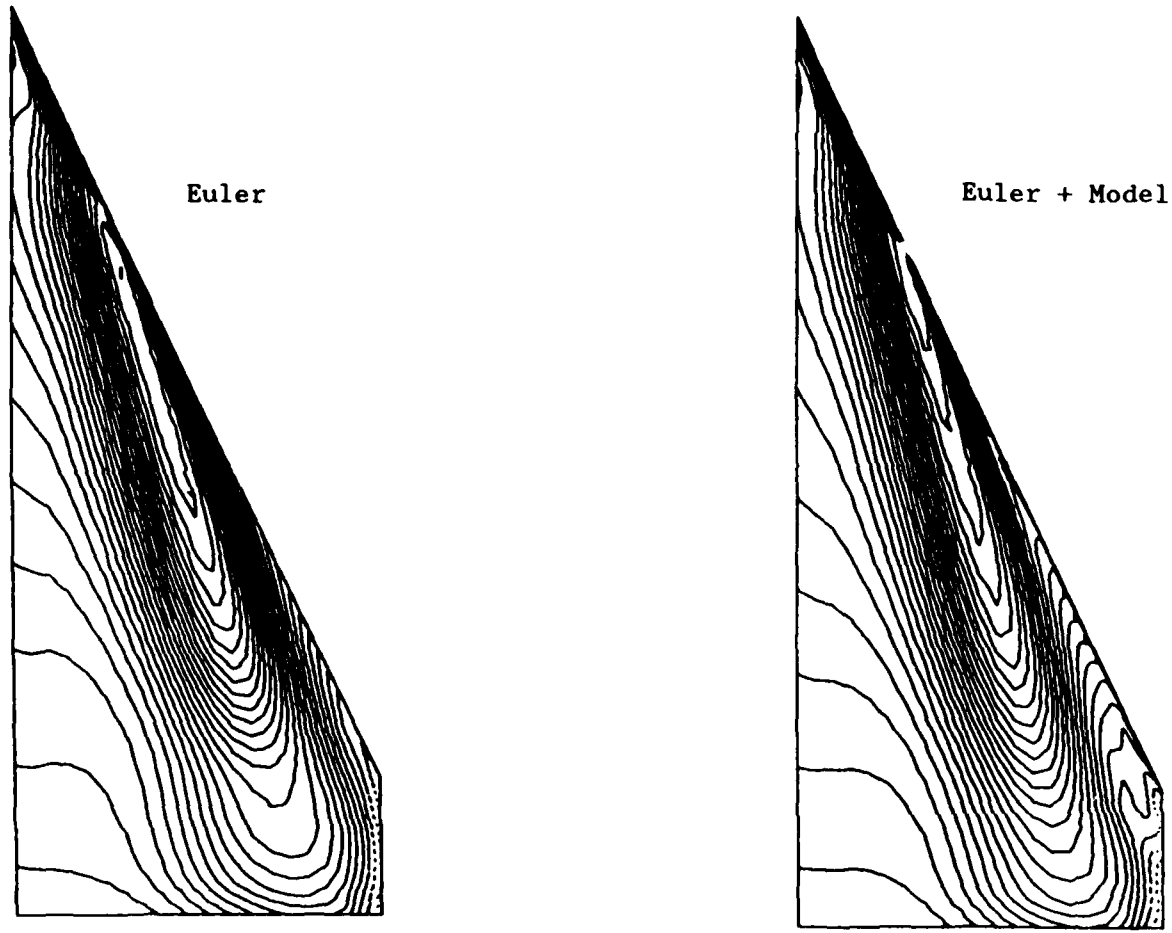

Figure 33. Surface pressure contours for a 65 degree delta wing with a NACA 65A005 airfoil at 20 degrees angle of attack.

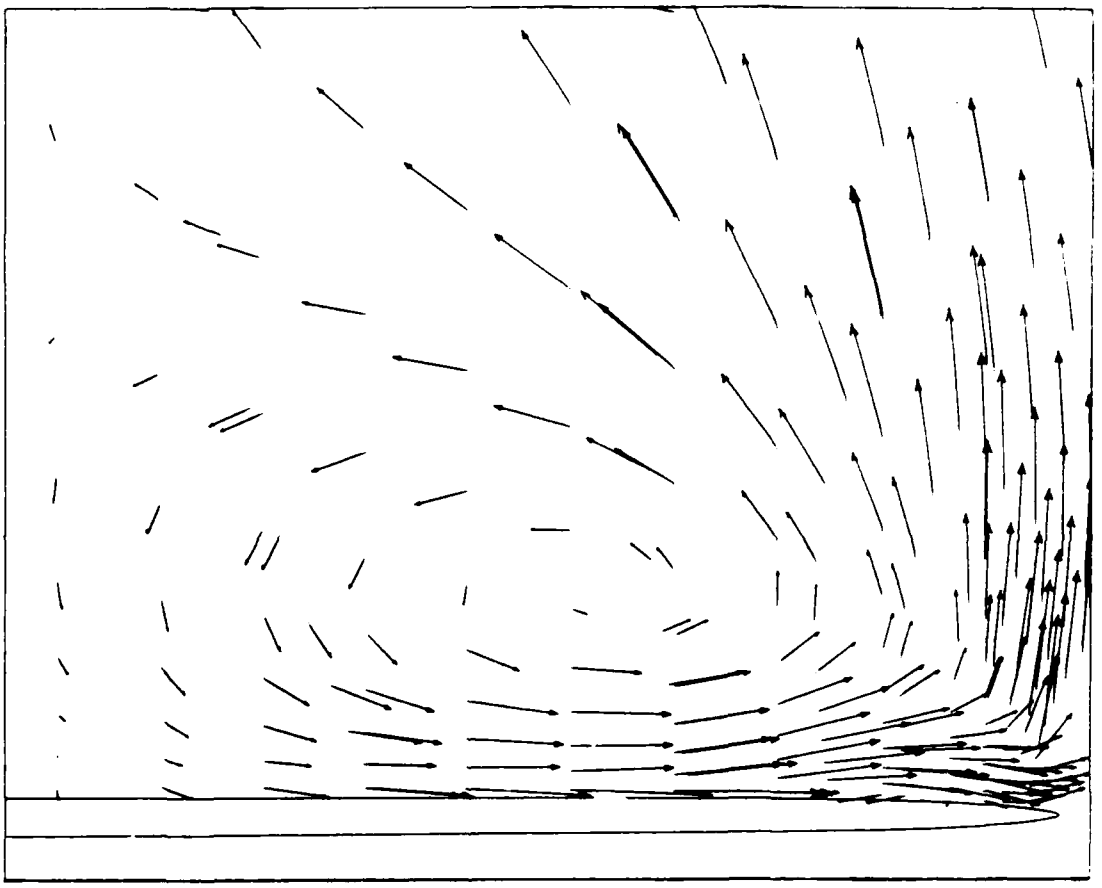

Figure 34. Crossflow velocity vectors at X/C_{root} = 0.87 for a 65 degree delta wing with a NACA 65A005 airfoil at 20 degrees angle of attack.

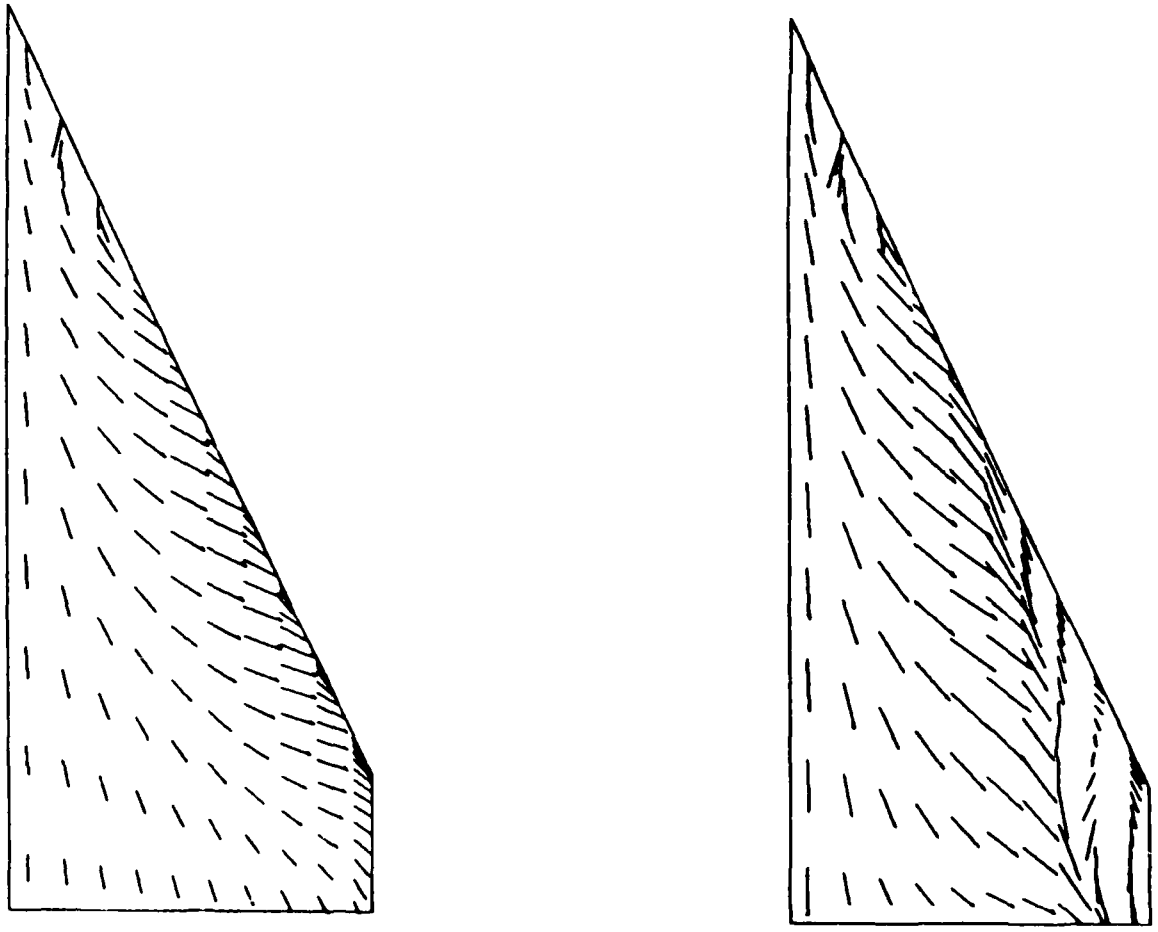

Figure 35. Planform view of surface velocity vectors on a 65 degree delta wing with a NACA 65A005 airfoil at 20 degrees angle of attack.

CHAPTER 6

CONCLUSIONS

A vortex core model has been derived which introduces the effects of physical viscosity for vortex cores into computer solutions of the 3-dimensional Euler equations. The formulation of this model allows it to replace the effects of numerical viscosity in the solution with those based on physical viscosity. The model has been used to predict the onset and location of vortex bursting on a variety of delta wings. In each case, the Euler code with the core model predicted bursting locations as a function of angle of attack which were in much better agreement with wind tunnel data and Navier-Stokes simulations than the results for an Euler code alone. The same values of the model control parameters produced reasonably good results for all the tests. Such good performance for a variety of wings and angles of attack without any adjustments of the model control parameters is a strong argument that the approximations made in deriving the model are acceptable, and that the model is useful. The core model also produced favorable effects on wing surface pressure distributions

which agree with wind tunnel results and Navier-Stokes simulations better than results from the Euler code alone. This improvement is seen whether or not bursting is present in the solution.

Another model which describes viscosity effects in the viscous shear layer near highly swept wings has also been derived. The model uses an analogy to the boundary layer on a flat plate to make a correction to the pressure on the wing surface. This pressure correction accounts for total pressure losses due to viscous dissipation in the shear layer, and contributes to the leading edge separation which rolls up into a leading edge vortex. The model also calculates momentum source terms for the grid cells next to the wing surface to account for the net momentum loss in these cells due to viscosity. The new boundary condition has been tested on several highly swept wings with rounded leading edges for a range of angles of attack. Surface pressure distributions for these tests were found to be in better agreement with wind tunnel tests of the same wing geometry than results for an Euler code with conventional boundary conditions. At higher angles of attack, a secondary separation and secondary vortex could be seen in the flow solution. This feature makes these flow solutions more similar to Navier-Stokes solutions and wind tunnel tests than any solutions from Euler solvers alone.

The two models for vortex-related viscosity effects which have been developed in the present work can be extended in many ways to improve their capabilities. The success of these models and the great need for the capability they can provide make such extensions very attractive.

The next logical step for the vortex core model is to extend it to include compressibility effects so the model could be used for higher Mach number problems. An extension of the model to include unsteady flow could also be done. This might have applications for time-accurate simulations of vortex bursting used to determine aircraft stability derivatives. Higher order approximations for the vortex core growth model could also be

developed. This could even be formulated as a differential equation which is integrated numerically whenever the model sources terms are updated.

The shear layer model could also be extended to include compressibility and unsteady effects. The first step, however, should be to use a model for the shear layer thickness and shear stress which accounts for geometry effects such as leading edge curvature and sweep angle and the presence of a flow reattachment line. This should permit the model to be used for a greater variety of wing shapes without changing the control parameters.

REFERENCES

1. Wilson, H. A. and Lovell, J. C., "Full-Scale Investigation of the Maximum Lift Flow Characteristics of an Airplane Having Approximately Triangular Planform," NACA RM L6K20, Nov. 1946.

2. Hummel, D., "On the Vortex Formation Over a Slender Delta Wing at Large Angles of Incidence," AGARD-CP-247, Paper No. 15, 1978.

3. Anders, K., "LDV Measurements of the Velocity Field of a Leading Edge Vortex over a Delta Wing Before and After Breakdown," Von Karman Institute for Fluid Dynamics TN 142, Mar. 1982.

4. Wentz, W. H. and Kohlman, D. L., "Vortex Breakdown on Slender Sharp-Edged Wings," Journal of Aircraft, Vol. 8, No. 3, March 1971, pp. 156-161.

5. Payne, F. M. and Nelson, R. C., "An Experimental Investigation of Vortex Breakdown on a Delta Wing," Vortex Flow Aerodynamics, NASA CP 2416, Vol. 1, Oct. 1985, pp. 135-161.

6. Hall, R. M., "Influence of Forebody Cross-Sectional Shape on Wing Vortex-Burst Location," Journal of Aircraft, Vol. 24, No. 9, Sep. 1987, pp. 645-652.

7. Lawford, J. A., and Beauchamp, A. R., "Low Speed Wind Tunnel Measurements on a Thin Sharp Edged Delta Wing with 70 Degree Leading Edge Sweep, with Particular Reference to the Position of Leading Edge Vortex Breakdown," RAE TN Aero 2797, 1961.

8. Skow, A. M., Titiraga Jr., A., and Moore, W. A., "Forebody/Wing Vortex Interactions and Their Influence on Departure and Spin Resistance," High Angle of Attack Aerodynamics, AGARD CP 247, Oct. 1978.

9. Polhamus,E. C., "A Concept of the Vortex Lift of Sharp-Edge Delta Wings Based on a Leading Edge Suction Analogy," NASA TN D-3767, Dec. 1966.

10. Johnson, F. T., Lu, P., Tinoco, E. N., and Epton, M. A., "An Improved Panel Method for the Solution of Three-Dimensional Leading-Edge Vortex Flows," NASA CR-3278, Jul. 1980.

11. Hoejmakers, H. W. M., and Rizzi, A., "Vortex-Fitted Potential Solution Compared with Vortex-Captured Euler Solution for Delta Wing with Leading-Edge Vortex-Separation," AIAA Paper 84-2144, Aug. 1984.

12. Murman, E. M. and Rizzi, A., "Applications of Euler Equations to Sharp Edge Delta Wings with Leading Edge Vortices," AGARD Symposium on Application of Computational Fluid Dynamics in Aeronautics, Aix-en-Provence, France, Apr. 1986.

13. Jameson, A., Schmidt, W., and Turkel, E., "Numerical Solutions of the Euler Equations by Finite Volume Methods Using Runge-Kutta Time-Stepping Schemes," AIAA Paper 81-1259, June 1981.

14. Raj, P. and Long, L. N., "An Euler Aerodynamic Method for Leading-Edge Vortex Flow Simulation," Vortex Flow Aerodynamics, NASA CP 2416, Vol. 1, Oct. 1985, pp. 263-281.

15. Pulliam, T. H., "Euler and Thin Layer Navier-Stokes Codes: ARC2D, ARC3D," Notes for Computational Fluid Dynamics User's Workshop, Tullahoma, Tennessee, March 1984.

16. Rizzetta, D. P. and Shang, J. S., "Numerical Simulation of Leading-Edge Vortex Flows," AIAA Journal, Vol. 24, No. 2, Feb. 1986, pp. 237-245.

17. Kandil, O. A., Chuang, A. H., and Shifflette, J. M., "Finite-Volume Euler and Navier-Stokes Solvers for Three-Dimensional and Conical Vortex Flows Over Delta Wings," AIAA Paper 87-0041, Jan. 1987.

18. Hsu, C. H. and Liu, C. H., "Navier-Stokes Computation of Flow Around a Round-Edged Double-Delta Wing," AIAA Paper 88-2560-CP, June 1988.

19. Rizzi, A., "Euler Solutions of Transonic Vortex Flow Around the Dillner Wing - Compared and Analyzed," AIAA Paper No. 84-2142, Aug. 1984.

20. Newsome, R.W. and Thomas, J. L., "Computation of Leading Edge Vortex Flows," Vortex Flow Aerodynamics, NASA CP 2416, Vol. 1, Oct. 1985, pp. 305-330.

21. Kreiss, H. O., "Initial Boundary Value Problems for Hyperbolic Systems", Comm. Pure Appl. Math., Vol. 23, 1970, pp. 277-298.

22. Beam, R. M. and Warming, R. F., "An Implicit Factored Scheme for the Compressible Navier-Stokes Equations," AIAA Journal, Vol. 16, Apr. 1978, pp. 393-402.

23. Lamb, H., Hydronamics, Dover, N.Y., 1945, pp. 591-592.

24. Iversen, J. D., "Correlation of Turbulent Trailing Vortex Decay Data," AIAA Paper

25. Hall, M. G. "A Theory for the Core of a Leading-Edge Vortex," Journal of Fluid Mechanics, Vol. 11, 1961, pp. 209-232.

26. Brown, S. N. "The Compressible Inviscid Leading-Edge Vortex," Journal of Fluid Mechanics, Vol. 22, Part 1, 1965, pp. 13-32.

27. Mager, A. "Dissipation and Breakdown of a Wingtip Vortex," Journal of Fluid Mechanics, Vol. 55, part 4, 1972, pp. 609-628.

28. Krause, E., "A Contribution to the Problem of Vortex Breakdown," Computers and Fluids, Vol. 13, No.3, pp. 375-381.

29. Powell, K. G., and Murman, E. M., "A Model for the Core of a Slender Viscous Vortex," AIAA Paper 88-0503, Jan. 1988

30. Krause, E., "Numerical Analysis of Vortex Breakdown" Von Karman Institute Lecture Series 1985-01, Jan. 1985.

31. Grabowski, W. J., and Berger, S. A., "Solutions of the Navier-Stokes Equations for Vortex Breakdown", Journal of Fluid Mechanics, Vol. 75, No. 11, 1979, pp. 2053-2064.

32. Sarpkaya, "Vortex Breakdown in Swirling Conical Flows," AIAA Journal, Vol. 9, No. 9, 1971, pp. 1792-1799.

33. Faler, J. H. and Leibovich, S., "Disrupted States of Vortex Flow and Vortex Breakdown", Physics of Fluids, Vol. 20, No. 9, Sep. 1977, pp. 1385-1400.

34. Jones, J. P., "The Breakdown of Vortices in Separated Flow," U.S.A.A., Report No. 140, University of Southampton, 1960.

35. Benjamin, T.B., "Theory of the Vortex Breakdown Phenomenon," Journal of Fluid Mechanics, Vol. 14, part 4, pp. 593-629.

36. Lessen, M., Singh, P. J., and Paillet, F., "The Stability of a Trailing Line Vortex. Part 2, Viscous Theory," Journal of Fluid Mechanics, Vol. 63, part 4, 1974, pp. 753-763.

37. Leibovich, S., "Vortex Stability and Breakdown: Survey and Extension'" AIAA Journal, Vol. 22, No. 9, 1983, pp. 1192-1206.

38. Schlichting, H., Boundary Layer Theory, McGraw-Hill, 1979

39. Hartwich, P.-M., Hsu, C. H., Luckring, J. M., and Liu, C. H., "Numerical Study of the Vortex Burst Phenomenon for Delta Wings," AIAA Paper 88-0505, Jan. 1988.

40. Manroe, M. E., Manning, K. J. R., Halstaff, T. H., and Rogers, J. T., "Transonic Pressure Measurements and Comparison of Theory to Experiment for an Arrow-wing Configuration," NASA CR 2610, August 1976.

41. Keller, J. J., Egli, W. and Exley, J., Force- and Loss-Free Transitions Between Vortex Flow States'" Vortex Dominated Flows, Springer-Verlag, 1986.

APPENDIX A

VORTEX VELOCITY PROFILES

A great number of vortex velocity profiles have been defined as solutions to simplified versions of the Navier-Stokes equations or as approximations to the velocity distributions measured in real vortices. The most important of these will be described in a generally chronological order.

The point vortex is a two-dimensional circulating flow which solves Laplace's equation. The line vortex is a three-dimensional extension of the point vortex. Both are sometimes referred to as potential vortices because their flowfields are irrotational everywhere but at their exact center. The line vortex velocity profile is given by

$$u = \text{constant}$$

$$v = 0$$

$$w = \frac{\Gamma}{2\pi r}$$

The Rankine vortex is obtained by replacing the central part of a potential vortex with a core which rotates as a solid body. Its velocity profiles are given by

$$u = \text{constant}$$

$$v = 0$$

$$w = \frac{\Gamma r}{2\pi\delta^2} \qquad r \leq \delta$$

$$w = \frac{\Gamma}{2\pi r} \qquad r \geq \delta$$

The Rankine vortex has been used by Jones [34] and Keller, Egli, and Exley [41], among others, for vortex stability analysis and bursting prediction.

Lamb's vortex was derived as a solution for the decay of what is initially an infinite line vortex. The time dependent velocity profiles are given by

$$u = \text{constant}$$

$$v = 0$$

$$w = \frac{\Gamma}{2\pi r}\left(1 - e^{-\frac{r^2}{4\nu t}}\right)$$

Hall's vortex was derived as a solution to the Euler equations for a slender conical vortex core. The velocity profiles are

$$u = C\left(K - \ln\frac{r}{\delta}\right)$$

$$v = -\frac{1}{2} C \frac{r}{\delta}$$

$$w = C\left(K + \frac{1}{2} - \ln \frac{r}{\delta}\right)^{\frac{1}{2}}$$

where K is a shape factor for the profile and C determines the magnitudes of the velocities. This model was used by Hall [25], Anders [3] and others for bursting studies. The singularity at the center must be avoided with a patched solution to a diffusive subcore.

Mager defined his velocity profiles as polynomials which matched values and slopes with a potential external flow at the core edge. Only the u and w profiles were defined. The profiles for $r < \delta$ are

$$u = u_\delta + (u_\delta - u_0)\left(\frac{r}{\delta}\right)^2\left(6 - 8\frac{r}{\delta} + 3\left(\frac{r}{\delta}\right)^2\right)$$

$$w = w_\delta \frac{r}{\delta}\left(2 - \left(\frac{r}{\delta}\right)^2\right)$$

For $r > \delta$, the Mager vortex velocities are the same as for a potential vortex.

Several modifications of the Burgers vortex have been used. The Q vortex, first proposed by Lessen [36], uses the Burgers vortex circumferential velocity profile but a non-uniform axial profile. These profiles are

$$u = u_0 \; e^{-\frac{r^2}{\delta^2}}$$

$$w = q \left| u_0 \right| \frac{\delta}{r} \left(1 - e^{-\frac{r^2}{\delta^2}} \right)$$

where

$$q = \frac{\Gamma}{2\pi\delta u_0}.$$

Several other investigators have used this vortex model. In addition, Powell and Murman [29] derived a conical analog to the Burgers vortex which is represented as a system of ordinary differential equations.

APPENDIX B

IMAGE VORTEX VELOCITY DERIVATION

Consider first the two-dimensional case. The primary vortex and three image vortices are assumed to be infinite and parallel. The coordinate systems and definitions used in Chapter 3 apply. The pertinant geometry for this case is shown in Figure 32. Note that for simplicity in defining angles, this figure views the crossflow plane from the upstream direction, while Figures 8,9,10 and 11, for instance, view the problem from downstream. For these assumptions, the stream function in the XYZ coordinate system due to the image vortices is given by

$$\Psi_i = \frac{\Gamma}{2\pi} \ln\left(\frac{r_4}{r_2 r_3}\right).$$

From the geometry of the problem, the following equalities hold:

$$\begin{aligned}
(r\sin\theta + 2l_Y)^2 &= (r_2\sin\theta_2)^2 \\
(r\cos\theta)^2 &= (r_2\cos\theta_2)^2 \\
(r\sin\theta)^2 &= (r_3\sin\theta_3)^2 \\
(r\cos\theta - 2l_Z)^2 &= (r_3\cos\theta_3)^2 \\
(r\sin\theta + 2l_Y)^2 &= (r_4\sin\theta_4)^2 \\
(r\cos\theta - 2l_Z)^2 &= (r_4\cos\theta_4)^2
\end{aligned}$$

These equations can be solved for r_2, r_3, and r_4 in terms of r to obtain

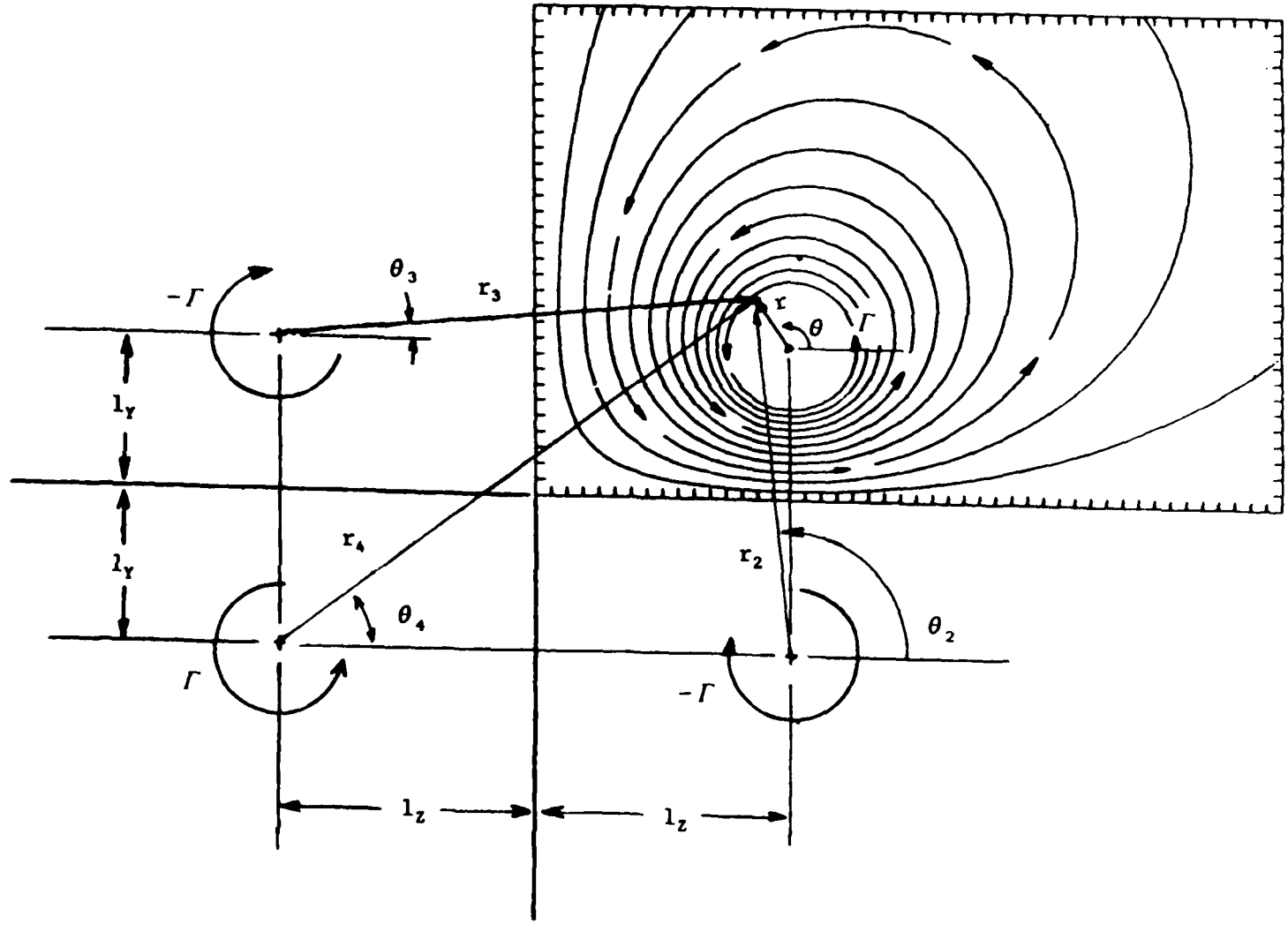

Figure 36. Image vortex geometry.

$$r_2 = \left(r^2 + 4l_Y r\sin\theta + 4l_Y^2\right)^{\frac{1}{2}}$$

$$r_3 = \left(r^2 - 4l_Z r\cos\theta + 4l_Z^2\right)^{\frac{1}{2}}$$

$$r_4 = \left(r^2 + 4l_Y r\sin\theta - 4l_Z\cos\theta + 4l_Y^2 + 4l_Z^2\right)^{\frac{1}{2}}$$

The stream function for the image vortices can therefore be written

$$\Psi_i = \frac{\Gamma}{2\pi}\left\{-\frac{1}{2}\ln\left(r^2 + 4l_Y r\sin\theta + 4l_Y^2\right) - \frac{1}{2}\ln\left(r^2 - 4l_Z r\cos\theta + 4l_Z^2\right)\right\}$$

$$+\frac{\Gamma}{4\pi}\ln\left(r^2 + 4l_Y r\sin\theta - 4l_Z r\cos\theta + 4l_Y^2 + 4l_Z^2\right)$$

Then the induced velocities in a cylindrical coordinate system fixed at the present location of the vortex center would be

$$v_i = \frac{1}{r}\frac{\partial\Psi_i}{\partial\theta} = -\frac{\Gamma}{2\pi}\left(\frac{2l_Y\cos\theta}{r^2 + 4l_Y r\sin\theta + 4l_Y^2} + \frac{2l_Z\sin\theta}{r^2 - 4l_Z r\cos\theta + 4l_Z^2}\right)$$

$$+\frac{\Gamma}{2\pi}\left(\frac{2l_Y\cos\theta + 2l_Z\sin\theta}{r^2 + 4l_Y r\sin\theta - 4l_Z r\cos\theta + 4l_Y^2 + 4l_Z^2}\right)$$

$$w_i = \frac{\partial\Psi_i}{\partial r} = -\frac{\Gamma}{2\pi}\left(\frac{r + 2l_Y\sin\theta}{r^2 + 4l_Y r\sin\theta + 4l_Y^2} + \frac{r - 2l_Z\cos\theta}{r^2 - 4l_Z r\cos\theta + 4l_Z^2}\right)$$

$$+\frac{\Gamma}{2\pi}\left(\frac{r + 2l_Y\sin\theta - 2l_Z\cos\theta}{r^2 + 4l_Y r\sin\theta - 4l_Z r\cos\theta + 4l_Y^2 + 4l_Z^2}\right)$$

But the xrθ coordinate system is moving with the vortex core, so the velocities induced at r = 0 must be subtracted off to yield the image vortex velocities in the moving coordinate system as

$$v_i = -\frac{\Gamma}{2\pi}\left\{\left(\frac{2l_Y\cos\theta}{r^2+4l_Yr\sin\theta+4l_Y^2}-\frac{\cos\theta}{2l_Y}\right)+\left(\frac{2l_Z\sin\theta}{r^2-4l_Zr\cos\theta+4l_Z^2}-\frac{\sin\theta}{2l_Z}\right)\right\}$$

$$+\frac{\Gamma}{2\pi}\left(\frac{2l_Y\cos\theta+2l_Z\sin\theta}{r^2+4l_Yr\sin\theta-4l_Zr\cos\theta+4l_Y^2+4l_Z^2}-\frac{l_Y\cos\theta+l_Z\sin\theta}{l_Y^2+l_Z^2}\right)$$

$$w_i = -\frac{\Gamma}{2\pi}\left\{\left(\frac{r+2l_Y\sin\theta}{r^2+4l_Yr\sin\theta+4l_Y^2}-\frac{\sin\theta}{2l_Y}\right)+\left(\frac{r-2l_Z\cos\theta}{r^2-4l_Zr\cos\theta+4l_Z^2}+\frac{\cos\theta}{2l_Z}\right)\right\}$$

$$+\frac{\Gamma}{2\pi}\left(\frac{r+2l_Y\sin\theta-2l_Z\cos\theta}{r^2+4l_Yr\sin\theta-4l_Zr\cos\theta+4l_Y^2+4l_Z^2}-\frac{l_Y\sin\theta-l_Z\cos\theta}{l_Y^2+l_Z^2}\right)$$

Now, in the three dimensional case, the image vortices are not, in general, parallel to the primary vortex, nor to each other. In this case, the induced velocities must be multiplied by the cosines of the angles between the primary vortex and the image vortices to get:

$$v_i = -\frac{\Gamma}{2\pi}\left\{\cos\phi_Y\left(\frac{2l_Y\cos\theta}{r^2+4l_Yr\sin\theta+4l_Y^2}-\frac{\cos\theta}{2l_Y}\right)+\cos\phi_Z\left(\frac{2l_Z\sin\theta}{r^2-4l_Zr\cos\theta+4l_Z^2}-\frac{\sin\theta}{2l_Z}\right)\right\}$$

$$+\frac{\Gamma}{2\pi}\cos\phi_Y\cos\phi_Z\left(\frac{2l_Y\cos\theta+2l_Z\sin\theta}{r^2+4l_Yr\sin\theta-4l_Zr\cos\theta+4l_Y^2+4l_Z^2}-\frac{l_Y\cos\theta+l_Z\sin\theta}{l_Y^2+l_Z^2}\right)$$

$$w_i = -\frac{\Gamma}{2\pi}\left\{\cos\phi_Y\left(\frac{r+2l_Y\sin\theta}{r^2+4l_Yr\sin\theta+4l_Y^2}-\frac{\sin\theta}{2l_Y}\right)+\cos\phi_Z\left(\frac{r-2l_Z\cos\theta}{r^2-4l_Zr\cos\theta+4l_Z^2}+\frac{\cos\theta}{2l_Z}\right)\right\}$$

$$+\frac{\Gamma}{2\pi}\cos\phi_Y\cos\phi_Z\left(\frac{r+2l_Y\sin\theta-2l_Z\cos\theta}{r^2+4l_Yr\sin\theta-4l_Zr\cos\theta+4l_Y^2+4l_Z^2}-\frac{l_Y\sin\theta-l_Z\cos\theta}{l_Y^2+l_Z^2}\right)$$

APPENDIX C

WING GEOMETRY DATA

Three different types of wings are used in the present work. The first group are delta wings with leading edge sweep angles ranging from 55 to 76 degrees. The second group of wings are highly swept and tapered. These wings are often referred to as arrow wings. The third group are two cropped delta wings with identical planforms but different airfoil sections.

Four different delta wings are used. All have very thin flat plate airfoils. Pertinate data for these wings are listed in Table 1.

	Sweep Angle	Aspect Ratio	Half Span/Root Chord
Wing 1	55	2.800	.7002
Wing 2	65	1.865	.4663
Wing 3	75	1.072	.2679
Wing 4	76	1.000	.2500

Table 1. Delta wing geometry data.

The arrow wings had leading edge sweep angles of 71.2 degrees and taper ratios of 0.10. Half span divided by root chord was 0.4545. The aspect ratio was 1.653. Arrow wing number 1 had an NACA 0012 airfoil. Coordinates for the airfoil section of the second arrow wing are listed in Table 2.

X	Y
0.0000	0.0000
0.1250	0.3359
0.2500	0.4506
0.5000	0.6064
0.7500	0.7247
1.0000	0.8182
1.5000	0.9520
2.5000	1.1191
5.0000	1.3448
8.5000	1.4809
10.0000	1.5195
12.5000	1.5444
15.0000	1.5630
17.5000	1.5720
20.0000	1.5813
30.0000	1.6214
40.0000	1.6398
45.0000	1.6282
50.0000	1.5901
60.0000	1.4344
65.0000	1.3121
70.0000	1.1627
72.5000	1.0792
75.0000	0.9921
77.5000	0.9006
80.0000	0.8069
85.0000	0.6132
90.0000	0.4156
95.0000	0.2153
100.0000	0.0113

Table 2. Arrow wing number 2 airfoil coordinates.

The cropped delta wings had 65 degree swept leading edges and taper ratios of 0.15. Half span divided by root chord was 0.3964 and aspect ratio was 1.379. One wing used a NACA 0012 airfoil. The other used a NACA 65A005.

APPENDIX D

EVALUATION OF MODEL CONSTANTS

Consider equation (9c). Three different w velocity profiles are chosen and used to integrate (9c) to obtain a relationship between pressure at the vortex center and pressure at the core edge. These profiles are the Rankine vortex, Mager's vortex, and the Rankine vortex with image vortex induced velocities added to it.

For the Rankine vortex, equation (9c) is integrated from the vortex center to the vortex edge to yield

$$\int_0^{\delta} \frac{\partial p}{\partial r} dr = \int_0^{\delta} \frac{w^2}{r} dr = \int_0^{\delta} \left(\frac{\Gamma r}{2\pi\delta^2} \right)^2 \frac{1}{r} dr = \frac{\Gamma^2}{4\pi^2\delta^4} \int_0^{\delta} r\, dr$$

or

$$p(x,\delta) - p(x,0) = \frac{\Gamma^2}{4\pi^2\delta^2}\left(\frac{1}{2}\right) = \frac{\Gamma^2}{8\pi}\left(\frac{1}{\pi\delta^2}\right) = \frac{\Gamma^2}{8\pi a}$$

$$p(x,0) = p(x,\delta) - \frac{\Gamma^2}{8\pi a}$$

so

$$K_a = \frac{1}{8\pi} \qquad \text{and} \qquad K_i = 0$$

Next, using the Mager w velocity profile,

$$\int_0^\delta \frac{w^2}{r}dr = \int_0^\delta \left\{\frac{\Gamma}{2\pi\delta}\left(\frac{r}{\delta}\right)\left(2-\frac{r^2}{\delta^2}\right)\right\}^2 \frac{1}{r}dr$$

$$= \frac{\Gamma^2}{4\pi^2\delta^2}\int_0^\delta \left(\frac{4r}{\delta^2}-\frac{4r^3}{\delta^4}+\frac{r^5}{\delta^6}\right)dr = \frac{7\Gamma^2}{24\pi a}$$

so

$$p(x,0) = p(x,\delta) - \frac{7\Gamma^2}{24\pi a} \qquad \text{and} \qquad K_a = \frac{7}{24\pi} \quad , \quad K_i = 0$$

Finally, for the Rankine vortex plus image vortex velocities, it is first assumed that within the vortex core, r is enough smaller than l_Y and l_Z that r^2 can be neglected compared with $4l_Y^2$ and $4l_Z^2$ in equation (10b). It is further assumed that flattening of portions of the vortex core which come close to a solid wall reduces the effect on core pressure of the velocities induced by the image vortex on the other side of that wall. This occurs because flattening of the core reduces the curvature and hence the radial pressure gradient of that portion of the core where image vortex velocities would otherwise increase the radial pressure gradient. As a result, sine and cosine terms in (10b) are also neglected, and the expression which is integrated is

$$\int_0^\delta \frac{w^2}{r}dr = \int_0^\delta \left\{\frac{\Gamma}{2\pi\delta}\left(\frac{r}{\delta}\right)\left(1-\delta^2 C_\phi\right)\right\}^2 \frac{1}{r}dr$$

where C_ϕ is given by equation (12). The integral can be written

$$\frac{\Gamma^2}{4\pi^2\delta^2}\left(1-\delta^2 C_\phi\right)^2 \int_0^\delta \frac{r}{\delta^2} dr \;=\; \frac{\Gamma^2}{4\pi^2\delta^2}\left(1-2\delta^2 C_\phi+\delta^4 C_\phi^2\right)\left(\frac{1}{2}\right)$$

For $\delta < l_Y$ and $\delta < l_Z$, the term $\delta^4 C_\phi^2$ is small compared with $\delta^2 C_\phi$, so the expression for pressure is approximated by

$$p(x,0) \;=\; p(x,\delta) \;-\; \frac{\Gamma^2}{8\pi a}+\frac{\Gamma^2}{4\pi a}\delta^2 C_\phi$$

$$p(x,0) \;=\; p(x,\delta) \;-\; \frac{\Gamma^2}{8\pi a}+\frac{\Gamma^2}{4\pi^2} C_\phi$$

$$K_a \;=\; \frac{1}{8\pi} \qquad \text{and} \qquad K_i \;=\; \frac{1}{4\pi^2}$$

Next, consider equation (9d). First, for a Rankine vortex, v = 0 and the radial variation of w is linear, so, if u is not zero, (9d) reduces to

$$\frac{\partial w}{\partial x} \;=\; 0$$

which, since

$$w \;=\; \frac{\Gamma r}{2\pi\delta^2} \;=\; \frac{\Gamma r}{a}$$

can only be satisfied for all r inside the core and all x if

$$\frac{\Gamma(x)}{a(x)} = \text{constant.}$$

However, equations (9a) and (9b) can only be satisfied for this case if vortex strength and core area are both constant for all x. A more useful vortex model can be obtained by using the Rankine vortex w profiles, but allowing v to be determined by integrating equation (9a) with respect to r. The u profile will still be modeled as uniform in the core but not necessarily equal to the axial velocity outside the core. Since this profile is axisymmetric, (9a) can be rewritten

$$\frac{\partial(ru)}{\partial x} + \frac{\partial(rv)}{\partial r} = 0$$

so

$$rv = -\int_0^r \frac{\partial(\eta u)}{\partial x} d\eta$$

where n is a dummy variable for r. Since $u = u_0$ everywhere in the core,

$$\frac{\partial(ru)}{\partial x} = r\frac{du_0}{dx}$$

$$rv = -\frac{du_0}{dx}\int_0^r \eta\, d\eta = -\frac{du_0}{dx}\left(\frac{r^2}{2}\right)$$

$$v = -\left(\frac{r}{2}\right)\frac{du_0}{dx}$$

Then, in equation (9d) the Rankine vortex w profile still causes the viscous term to vanish, and axisymmetry makes circumferential derivatives zero, but the other terms remain to give

$$u_0\frac{\partial w}{\partial x} - \left(\frac{r}{2}\right)\frac{du_0}{dx}\frac{\partial w}{\partial r} - \frac{1}{2}\frac{du_0}{dx}w = 0$$

or

$$u_0\left\{\frac{r}{2\pi\delta^2}\frac{\partial \Gamma}{\partial x} - \frac{\Gamma r}{\pi\delta^2}\left(\frac{1}{\delta}\right)\frac{\partial \delta}{\partial x}\right\} - \frac{\Gamma r}{2\pi\delta^2}\frac{du_0}{dx} = 0.$$

This expression is integrated over the area of the core to obtain

$$u_0\left(\frac{1}{2}\frac{d\Gamma}{dx} - \Gamma\frac{1}{\delta}\frac{d\delta}{dx}\right) - \frac{\Gamma}{2}\frac{du_0}{dx} = 0$$

$$\frac{1}{a}\frac{da}{dx} = \frac{1}{\Gamma}\frac{d\Gamma}{dx} - \frac{1}{u_0}\frac{du_0}{dx}$$

$$K_1 = 1 \quad , \quad K_2 = 1 \quad \text{and} \quad K_3 = 0$$

If the Mager profiles are used, the u distribution is a function of the

ratio of u at the vortex center to u at the core edge. If B is used to represent this ratio, which Mager calls the axial velocity form parameter, then u is given by

$$u = u_\delta\left\{B+(1-B)\left(\frac{r}{\delta}\right)^2\left(6-8\left(\frac{r}{\delta}\right)+3\left(\frac{r}{\delta}\right)^2\right)\right\}$$

and the v obtained by integrating (9a) is

$$\begin{aligned} v = & -\frac{du_\delta}{dx}\left\{\frac{rB}{2}+r(1-B)\left(\frac{3}{2}\left(\frac{r}{\delta}\right)^2-\frac{8}{5}\left(\frac{r}{\delta}\right)^3+\frac{1}{2}\left(\frac{r}{\delta}\right)^4\right)\right\} \\ & -ru_\delta\frac{dB}{dx}\left\{\frac{1}{2}-\frac{3}{2}\left(\frac{r}{\delta}\right)^2+\frac{8}{5}\left(\frac{r}{\delta}\right)^3-\frac{1}{2}\left(\frac{r}{\delta}\right)^4\right\} \\ & +ru_\delta(1-B)\frac{d\delta}{dx}\left\{3\left(\frac{r}{\delta}\right)^3-\frac{24}{5}\left(\frac{r}{\delta}\right)^4+2\left(\frac{r}{\delta}\right)^5\right\} \end{aligned}$$

When equation (9d) is integrated over the area of the core, the result is

$$\frac{1}{\Gamma}\frac{d\Gamma}{dx}\left(\frac{2}{5}+\frac{B}{15}\right)-\frac{1}{u_\delta}\frac{du_\delta}{dx}\left(\frac{121B-37}{630}\right)-\left(\frac{11}{70}\right)\frac{dB}{dx}-\frac{1}{2a}\frac{da}{dx}\left(\frac{1571B-227}{2520}\right) = -\frac{8\pi}{3Re\epsilon^2au_\delta}$$

which, for B=1 all along the vortex, reduces to

$$\frac{1}{a}\frac{da}{dx} = \frac{7}{4\Gamma}\frac{d\Gamma}{dx}-\frac{1}{u_0}\frac{du_0}{dx}+\frac{10\pi}{Re\epsilon^2au_0}.$$

$$K_1 = \frac{7}{4} \quad , \quad K_2 = 1 \quad \text{and} \quad K_3 = 10\pi$$

VITA

Steven Allan Brandt [redacted] He received Bachelors and Masters degrees in aerospace engineering from Iowa State University in 1975 and 1976 respectively. A technical paper based on his Masters thesis research and entitled "Merging of Aircraft Trailing Vortices" was published in the June, 1977 Journal of Aircraft.

He entered active duty in the United States Air Force in 1977 and after completing Undergraduate Pilot Training, served as an instructor pilot and flight evaluator in the T-37 and F-106 aircraft. He also served as an academic instructor in th Euro-NATO Joint Jet Pilot Training program at Sheppard Air Force Base, Texas, and wrote a textbook entitled Applied Aerodynamics. This text was published locally and used in training instructor pilots from all the NATO countries. He currently holds the rank of Major in the Air Force.

A technical paper based on his doctoral dissertation research and entitled "Modeling of Vortex Dominated Flows in the Euler Formulation" will be presented at the 16th international congress of the International Council of the Aeronautical Sciences in Jerusalem, Israel in September, 1988.